

Scanning probe microscopy investigation of complex-oxide heterostructures

by

Feng Bi

Bachelor of Science, Nanjing University, 2007

Master of Science, University of Pittsburgh, 2010

Submitted to the Graduate Faculty of
the Kenneth P. Dietrich School of Arts and Sciences in partial fulfillment
of the requirements for the degree of
Doctor of Philosophy

University of Pittsburgh

2015

UNIVERSITY OF PITTSBURGH
KENNETH P. DIETRICH SCHOOL OF ARTS AND SCIENCES

This thesis was presented

by

Feng Bi

It was defended on

Mar. 19, 2015

and approved by

Adam Keith Leibovich, Associate Professor, Department of Physics and Astronomy

Robert P. Devaty, Associate Professor, Department of Physics and Astronomy

Brian D'Urso, Assistant Professor, Department of Physics and Astronomy

Kenneth Jordan, Professor, Department of Chemistry

Thesis Director: Jeremy Levy, Professor, Department of Physics and Astronomy

Scanning probe microscopy investigation of complex-oxide heterostructures

Feng Bi, PhD

University of Pittsburgh, 2015

Copyright © by Feng Bi

2015

Scanning probe microscopy investigation of complex-oxide heterostructure

Feng Bi, PhD

University of Pittsburgh, 2015

Advances in the growth of precisely tailored complex-oxide heterostructures have led to new emergent behavior and associated discoveries. One of the most successful examples consists of an ultrathin layer of LaAlO_3 (LAO) deposited on TiO_2 -terminated SrTiO_3 (STO), where a high mobility quasi-two dimensional electron liquid (2DEL) is formed at the interface. Such 2DEL demonstrates a variety of novel properties, including field tunable metal-insulator transition, superconductivity, strong spin-orbit coupling, magnetic and ferroelectric like behavior. Particularly, for 3-unit-cell (3 u.c.) LAO/STO heterostructures, it was demonstrated that a conductive atomic force microscope (c-AFM) tip can be used to “write” or “erase” nanoscale conducting channels at the interface, making LAO/STO a highly flexible platform to fabricate novel nanoelectronics. This thesis is focused on scanning probe microscopy studies of LAO/STO properties. We investigate the mechanism of c-AFM lithography over 3 u.c. LAO/STO in controlled ambient conditions by using a vacuum AFM, and find that the water molecules dissociated on the LAO surface play a critical role during the c-AFM lithography process. We also perform electro-mechanical response measurements over top-gated LAO/STO devices. Simultaneous piezoresponse force microscopy (PFM) and capacitance measurements reveal a correlation between LAO lattice distortion and interfacial carrier density, which suggests that PFM could not only serve as a powerful tool to map the carrier density at the interface but also provide insight into previously reported frequency dependence of capacitance enhancement of top-gated LAO/STO structures. To study magnetism at the LAO/STO interface, magnetic force microscopy

(MFM) and magnetoelectric force microscopy (MeFM) are carried out to search for magnetic signatures that depend on the carrier density at the interface. Results demonstrate an electronically-controlled ferromagnetic phase on top-gated LAO/STO heterostructures at room temperature. A follow-up study shows that electronically-controlled magnetic signatures are observed only within a LAO thickness window from 8 u.c. to 30 u.c. We also have developed a cryogen-free low-temperature AFM based on a commercial vacuum AFM. The modified system operates under high vacuum (10^{-6} Torr) and the base temperature is ~ 10 K. This low temperature AFM will be used in future experiments.

TABLE OF CONTENTS

PREFACE	XV
1.0 INTRODUCTION	1
1.1 LaAlO₃/SrTiO₃ INTERFACE	2
1.2 MATERIAL GROWTH	2
1.3 POSSIBLE ORIGIN OF QUASI-2DEL	5
1.4 EMERGENT PROPERTIES OF LAO/STO HETEROSTRUCTURE	7
2.0 EXPERIMENTAL METHOD	12
2.1 DEVICE FABRICATION	12
2.2 ATOMIC FORCE MICROSCOPY (AFM)	15
2.2.1 AFM working principle	16
2.2.2 Contact mode	17
2.2.3 AC mode	19
2.2.4 Piezoresponse force microscopy (PFM)	20
2.2.5 Quantitative PFM analysis	22
2.2.6 Magnetic force microscopy (MFM)	24
2.2.7 Magneto-electric force microscopy (MeFM)	26
2.3 C-AFM LITHOGRAPHY ON LAO/STO	27
2.3.1 Introduction	27
2.3.2 c-AFM lithography in contact mode	28
2.3.3 Sketched high performance nanodevices	30
2.3.4 Possible mechanism	31

3.0	'WATER CYCLE' MECHANISM FOR WRITING AND ERASING NANOSTRUCTURES AT THE $\text{LaAlO}_3/\text{SrTiO}_3$ INTERFACE.....	33
3.1	INTRODUCTION	33
3.2	SAMPLE GOWTH.....	34
3.3	EXPERIMENT SET UP	35
3.4	WRITING AND ERASING UNDER CONTROLLED ENVIRONMENT .	37
3.5	NANO DEVICE SELF-ERASE STUDY IN CONTROLLED AMBIENT ..	41
3.6	CONCLUSION	42
4.0	ELECTRO-MECHANICAL RESPONSE OF TOP-GATED LAO/STO	43
4.1	INTRODUCTION	43
4.2	SAMPLE GROWTH.....	44
4.3	DEVICE GEOMETRY AND FABRICATION.....	44
4.4	EXPERIMENTS AND RESULTS.....	46
4.4.1	Top-gate tuned MIT at interface	46
4.4.2	Capacitance and piezoresponse measurements.....	47
4.4.3	Quantitative PFM analysis.....	51
4.4.4	Surface displacement calculation	53
4.4.5	Simultaneous capacitance and peizoresponse measurements.....	55
4.4.6	Time-resolved PFM measurements and frequency dependence of capacitance enhancement	56
4.4.7	Interfacial carrier density distribution mapping by spatially resolved PFM imaging	59

4.4.8	RMS and histogram analysis of bias dependent inhomogeneity at the interface.....	62
4.5	CONCLUSION AND DISCUSSION.....	63
5.0	ELECTRONICALLY CONTROLLED FERROMAGNETISM ON TOP-GATED LAO/STO AT ROOM TEMPERATURE	66
5.1	INTRODUCTION	66
5.2	SAMPLE GROWTH.....	68
5.3	DEVICE GEOMETRY AND FABRICATION.....	69
5.4	EXPERIMENT METHODS AND SETUP	72
5.5	MEASUREMENTS	74
5.5.1	MFM on top-gated LAO/STO with different tip magnetization configurations (out-of-plane and in-plane) and modulated interfacial carrier density	74
5.5.2	MFM on bare LAO close to top gate with modulated interfacial carrier density	77
5.5.3	Sample interfacial magnetization reorientation in successive scans	79
5.5.4	Dynamic magneto-electric force (MeFM) microscopy mapping.....	81
5.5.5	2D FFT analysis of MeFM images.....	83
5.5.6	Histogram analysis of MFM images.....	85
5.6	DISUCSSION AND PERSPECTIVE	86
6.0	LaAlO₃ THICKNESS WINDOW FOR ELECTRONICALLY CONTROLLED MAGNETISM IN LAO/STO HETEROSTRUCTURES.....	89
6.1	INTRODUCTION	89

6.2	SAMPLE GROWTH.....	90
6.3	DEVICE GEOMETRY AND EXPERIMENT METHOD	91
6.4	MEASUREMENTS	92
6.5	DISCUSSION AND CONCLUSION	95
7.0	SUMMARY AND OUTLOOK.....	97
	APPENDIX A	99
	APPENDIX B	110
	APPENDIX C	117
	APPENDIX D	128
	BIBLIOGRAPHY	130

LIST OF TABLES

Table 4-1 Device Parameters.....	46
Table 5-1 Sample information and device parameters.	71
Table 5-2 List of scanning locations and corresponding figures.	71
Table 6-1 Sample information.	91

LIST OF FIGURES

Fig. 1-1 PLD growth of LAO layers on STO substrate.	4
Fig. 1-2 Mechanism for interfacial conductivity in LAO/STO	6
Fig. 1-3 Emergent properties of LAO/STO interface.	10
Fig. 2-1 Illustration of typical device fabrication process.	14
Fig. 2-2 Fabricated devices on LAO/STO.	15
Fig. 2-3 Illustration of force-distance curve and corresponding AFM image modes.	18
Fig. 2-4 Schematic diagram of the essential components for contact mode AFM.	18
Fig. 2-5 Schematic diagram of the essential components for AC mode AFM.	19
Fig. 2-6 Piezoresponse force microscopy illustration.	21
Fig. 2-7 Magnetic force microscopy illustration.	25
Fig. 2-8 Magnetoelectric force microscopy illustration.	26
Fig. 2-9 Conductive AFM lithography	29
Fig. 2-10 Sketchable high performance nanoelectronics.	31
Fig. 2-11 "water cycle" mechanism	32
Fig. 3-1 Fabricated electrodes and writing canvas.	35
Fig. 3-2 Writing and erasing nanowires.	37
Fig. 3-3 Nanowire writing versus various atmospheric conditions.	38
Fig. 3-4 Nanowire writing versus different air pressure.	39
Fig. 3-5 Nanowire writing under different relative humidity.	40
Fig. 3-6 Experiment showing effect of atmosphere on nanostructure self-erasure.	42
Fig. 4-1 Photograph of capacitor devices	45

Fig. 4-2 Resistance measurements between two electrodes that contact the interface	47
Fig. 4-3 Simultaneous PFM and capacitance measurement	49
Fig. 4-4 Piezoresponse under electric field.	51
Fig. 4-5 Quantitative analysis of PFM spectra on device A.	52
Fig. 4-6 Surface displacement calculation.	54
Fig. 4-7 Simultaneous time-dependent PFM and capacitance measurements	55
Fig. 4-8 Capacitance enhancement and time resolved PFM analysis.	57
Fig. 4-9 Spatially-resolved dual frequency PFM images show inhomogeneity at the interface. .	61
Fig. 4-10 Spatially resolved dual frequency PFM images	62
Fig. 4-11 Normalized RMS analysis for PFM images acquired over different locations on Device A (a), B (b) and C (c), respectively. The normalized RMS value is associated with the inhomogeneity at the interface.	63
Fig. 5-1 Optical images of fabricated devices.	70
Fig. 5-2 Sketch of experimental setup and CV characterization.	73
Fig. 5-3 Leakage current between top electrode and interface. Measurements are performed for Devices A-C.	73
Fig. 5-4 MFM on top-gated LAO/STO.	75
Fig. 5-5 Control MFM experiments using non-magnetic tip	76
Fig. 5-6 MFM experiments performed over the exposed LAO region.	78
Fig. 5-7 MFM images acquired in succession.	80
Fig. 5-8 Magneto-electric force microscopy (MeFM) experiments	82
Fig. 5-9 2D Fourier analysis of MeFM results.	84
Fig. 5-10 Histogram analysis of MFM images on magnetic domain boundary.	85

Fig. 6-1 Schematic of experimental setup and devices.....	92
Fig. 6-2 MFM on LAO/STO with LAO thickness range from 4 u.c. to 40 u.c.	93
Fig. 6-3 Device capacitance with respect to the LAO thickness.	94
Fig. A1 Front panel of the AFM lithography program.	100
Fig. A2 Front panel of important tab pages	103
Fig. A3 Block diagram of the program.	104
Fig. A4 ‘initialize’ case of the state machine.....	104
Fig. A5 ‘Configure’ case of the state machine.	106
Fig. A6 ‘Run’ case of the state machine.	107
Fig. B1 3D design of the cooling system for the vacuum AFM.....	111
Fig. B2 Essential parts of designed system.....	112
Fig. B3 Picture of assembled low temperature AFM system.	113
Fig. B4 System pressure during pumping down.	114
Fig. B5 System cool down history.....	115
Fig. B6 AFM height image of a grating sample in ambient air at room temperature.....	116
Fig. C1 Thermal spectroscopy of the MFM cantilever.....	118
Fig. C2 Electromagnets system used to magnetize the AFM tip.....	119
Fig. C3 MFM images on reference sample.....	121
Fig. C4 Schematic showing the AFM scanning environment.	122
Fig. C5 MFM images (3 $\mu\text{m} \times 3 \mu\text{m}$) acquired for various relative angles between the tip magnetization and the sample orientation.....	123
Fig. C6 MFM image over the same area on the top electrode of Device A with tip magnetization reversed.	124

Fig. C7 MFM on exposed LAO surface close to the top electrode for Devices B and C..... 125

Fig. C8 MeFM scanning above top electrode on Device A..... 126

Fig. C9 MeFM scanning over another $1.2 \times 1.2 \mu\text{m}^2$ square on Device A..... 127

Fig. D1 2-axis in-plane magnetic field generator module for Cypher AFM. 129

PREFACE

This thesis is the summary of my over six years' physics Ph.D. life. I need to thank so many people who helped me to finally get to this point.

First and foremost, I would like to thank my advisor Jeremy Levy for his patient guidance, hand-by-hand help and over five years of support. His hard-working, deep knowledge and research passion inspire me in every aspect. He also provided so many great opportunities for me to attend academic workshops and conferences, which I really appreciate.

I would like to thank all my former and current labmates: Patrick Irvin, Cen Cheng, Guanglei Cheng, Daniela Bogorin, Giriraj Jnawali, Yanjun Ma, Dongyue Yang, Mengchen Huang and Shuo Li. They help me to learn lab skills, give me precious comments on my manuscripts and work with me on different projects. They help to form a nice lab environment and let me advance to my graduation.

The good samples are crucial for my research. Therefore, I want to thank our collaborators Prof. Chang-Beom Eom and his group members, especially Chung Wung Bark, Hyungwoo Lee and Sangwoo Ryu at University of Wisconsin for providing high quality samples to our lab.

I also want to express my gratitude to my Ph.D. committee members, Adam Keith Leibovich, Robert P. Devaty, Brian D'Urso and Kenneth Jordan. Their guidance and comments help me on the right path of Ph.D. study.

Finally, I owe special thanks to my wife, my son and my parents for their support and encouragement during my Ph.D. study.

1.0 INTRODUCTION

Semiconductors have been the keystone of the modern electronic industry for many decades. For conventional semiconductors, such as silicon, germanium or III-V compounds, their band structures can be manipulated by doping with impurities, and their conductivity can be controlled by gating with electric fields. The convenience of conductivity tuning over a large range makes semiconductors ideal for the fabrication of electronic devices. However, the feature size of current electronics (~14 nm) is approaching the end of Moore's Law. There is increasing demand for alternative material systems with the capability of larger integration density and increased functionality.

Complex oxides, which possess a great variety of emergent properties, are candidates for the next generation electronics platform. Compared with conventional semiconductors, transition-metal oxides exhibit extensive novel functionalities such as superconductivity, ferroelectricity, ferroelasticity, ferromagnetism, high dielectric constant, colossal magnetoresistance and tunable metal-insulator transition. These fascinating and exotic properties make the oxide electronics not only an exciting research frontier but also an attractive field for industrial applications.

Motivated by all these aspects, this thesis is mainly focused on one of the most actively studied complex-oxide heterostructures: $\text{LaAlO}_3/\text{SrTiO}_3$ (LAO/STO). Research about the method and mechanism to create nanoelectronics on the LAO/STO interface, electro-mechanical response and ferromagnetism in top-gated LAO/STO heterostructures will be presented in the following sections.

1.1 LaAlO₃/SrTiO₃ INTERFACE

The perovskite materials LaAlO₃ and SrTiO₃ are both wide indirect band gap insulators ($E_{gap}^{LAO} = 5.6$ eV, $E_{gap}^{STO} = 3.2$ eV) and their lattice constants reasonably match each other (LAO \approx 3.789 Å and STO \approx 3.905 Å). In 2004, Ohtomo *et al.*¹ first reported that a high-mobility two dimensional electron liquid (2DEL) emerges at the interface of a few layers of LAO grown on top of a TiO₂-terminated STO substrate. Such conducting interface shows a typical carrier density² of 10^{12} - 10^{13} cm⁻², higher than that found in III-V semiconductor heterostructures (10^{10} - 10^{12} cm⁻²). In addition, the electron mobility at the LAO/STO interface can be as high as 10,000 cm²/Vs at low temperature ($T = 4$ K)¹. Reducing the lateral dimensions of the conducting channel³ at the LAO/STO interface can enhance the low-temperature mobility to $\sim 20,000$ cm²/Vs.

In most studies, the crystalline LAO is grown over the (001) STO substrates, which are commercially available. Recently, researchers attempt to grow LAO on (111) and (110) surface of STO substrates, which also lead to a conducting interface.⁴

1.2 MATERIAL GROWTH

Advances in the new material growth techniques, such as pulsed laser deposition⁵ (PLD) and molecular beam epitaxy⁶, now make precisely tailored complex-oxide heterostructures possible. In 2004, Ohtomo *et al.*¹ first successfully synthesized a LAO/STO heterostructure in an

ultrahigh vacuum chamber by PLD¹, which is the primary method to grow LAO thin films on STO substrates. LAO/STO heterostructures have also been fabricated by other methods such as molecular beam epitaxy⁷, sputtering⁸ and atomic layer deposition⁹.

There are several important aspects to generate a conducting LAO/STO interface: (1) TiO₂-terminated STO substrate (n-type interface).¹ (2) the proper growth condition and thermal annealing.^{1,10,11} (3) LAO layers above the critical thickness ~ 3 u.c.¹². (4) LAO stoichiometry (Al-rich LAO layer helps to make a conducting interface, while La-rich LAO leads to an insulating interface)¹³.

In this thesis, all the LAO/STO samples are grown in the group of our collaborator Chang Beom Eom at the University of Wisconsin-Madison, using PLD. The detailed sample growth steps are described as follows.

Before deposition, the TiO₂-terminated STO substrates with low-miscut angle ($<0.1^\circ$) are prepared by etching the surface with buffered HF acid. The STO substrates with (1 0 0) surface are annealed at 1000 °C for several hours so that atomically flat surfaces are created. During the deposition, a high power KrF excimer laser ($\lambda=248$ nm) beam is focused on a stoichiometric LAO single crystal target with energy density 1.5 J/cm². The laser pulses ablate the LAO target and the plume of ejected material is deposited onto the STO substrates. Each LAO unit cell is deposited by 50 laser pulses. Two typical growth conditions are used: (1) the substrate growth temperature $T=550$ °C and chamber background partial oxygen pressure $P(\text{O}_2) = 10^{-3}$ mbar ; (2) $T=780$ °C and $P(\text{O}_2)=10^{-5}$ mbar. For samples grown in condition (2), after deposition they are annealed at 600 °C in $P(\text{O}_2)=300$ mbar for one hour to minimize oxygen vacancies. During the LAO growth, the high pressure reflection high-energy electron diffraction (RHEED) is used to monitor the *in-situ* LAO thickness, which enables the precise control of layer-by-layer LAO growth. [Fig. 1-1\(a\)](#) shows the

RHEED intensity plot during LAO/STO sample growth, where three oscillations in the curve indicate the LAO thickness is 3 unit cells. The AFM height image of the grown LAO/STO (Fig. 1-1(b)) sample exhibits an atomically flat surface, where the terraces are the single unit cell height steps. The surface height profile along the red line cut is plotted as Fig. 1-1(c), from which each step height can be estimated as $\sim 4 \text{ \AA}$.

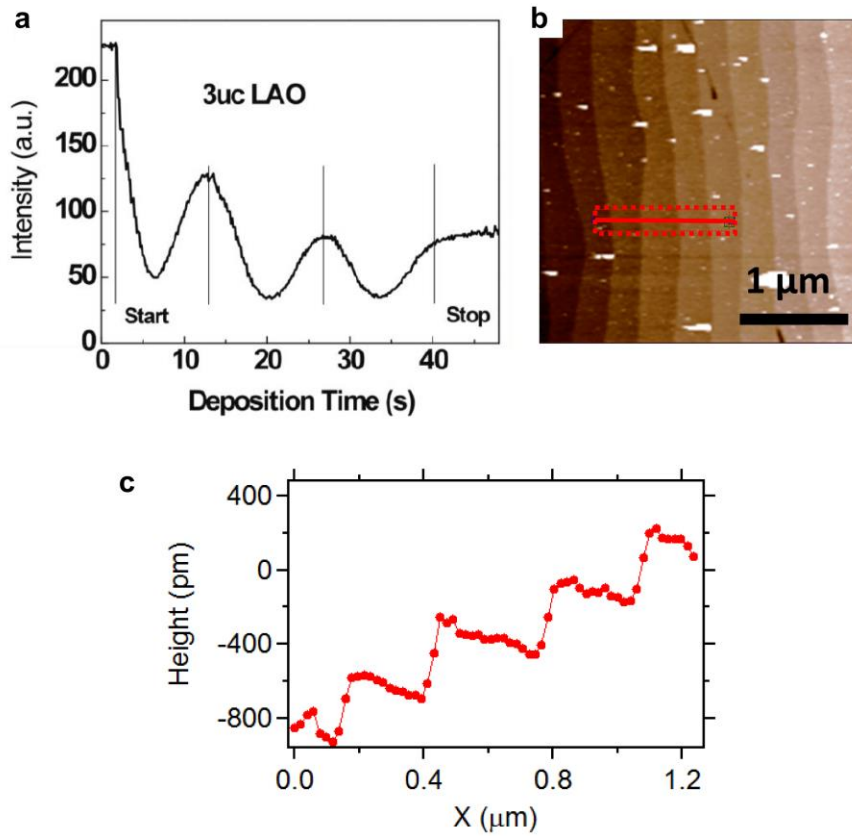


Fig. 1-1 PLD growth of LAO layers on STO substrate. (a), RHEED intensity oscillations during LAO film growth. The peaks marked by the vertical lines indicate each complete LAO unit cell is deposited. (Data is from our collaborator Prof. Chang-Beom Eom's group) (b), AFM height image of LAO surface, which shows the surface is atomically flat. (c), Height profile along the red line cut in (b).

1.3 POSSIBLE ORIGIN OF QUASI-2DEL

Although it is almost ten years since the LAO/STO conducting interface was first reported, the origin of the observed 2DEL is still under debate. Several mechanisms are proposed to explain the formation of the quasi-2DEL.

One explanation is about the oxygen vacancies embedded in LAO and STO (Fig. 1-2(a)). The intrinsic defects - oxygen vacancies could serve as donors, providing electrons to form the conducting interface.¹¹ Many experiments show that the interfacial conductivity is highly sensitive to the oxygen partial pressure during the growth and the post annealing process,^{1,10,11} which support the oxygen vacancies scenario. Another possible explanation is the cation intermixing across the interface (Fig. 1-2(b)). The exchange of La^{3+} and Sr^{2+} near the interface equivalently makes the STO locally doped and generates the 2DEL.¹⁴ Besides, the interfacial sharpness studies by TEM¹⁵ and XRD¹⁶ indicate such intermixing could play an important role in the 2DEL formation.

While both oxygen vacancies and cation intermixing point to the defects in LAO/STO, a popular mechanism called "polar catastrophe" describes an intrinsic electron reconstruction process within LAO/STO.¹⁵ As shown in Fig. 1-2(c), the STO substrate is a non-polar material with $\text{Ti}^{4+}\text{O}^{2-}_2$ and $\text{Sr}^{2+}\text{O}^{2-}$ planes charge neutral. However LAO is polar when it is epitaxially grown on STO. The $\text{La}^{3+}\text{O}^{2-}$ and $\text{Al}^{3+}\text{O}^{2-}_2$ planes have net charge $+e/-e$ respectively. When they alternatively stack together, the polar discontinuity at the interface will lead to a built-in electric potential which diverges with increasing LAO thickness. When the LAO thickness reaches a critical value, an electronic reconstruction is proposed to occur in which electrons transfer from the LAO surface to the interface, thus screening the built-in polarization. Fig. 1-2(c) also shows a schematic of the LAO/STO band diagram. The potential difference of the valance band across

LAO increases with LAO thickness. When a critical thickness is reached, the valance band is across the Fermi level and electrons transfer from the surface to the interface to form a 2DEL.

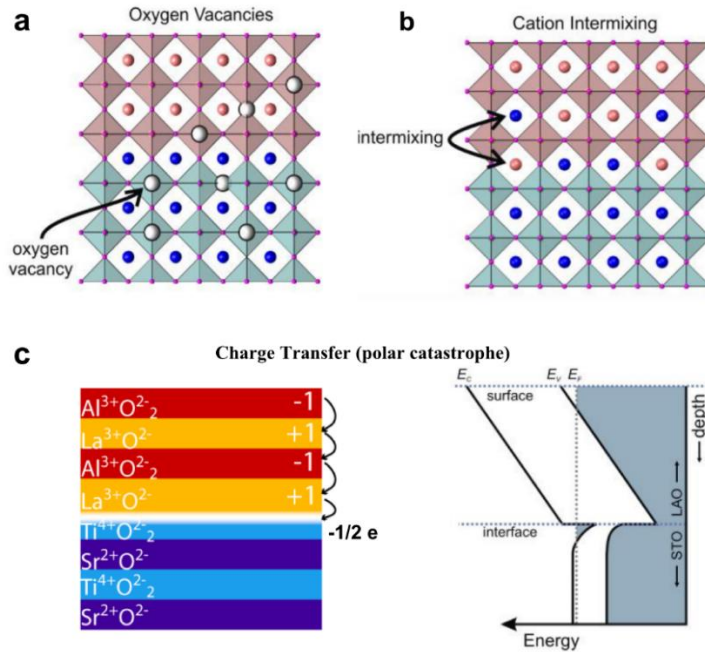


Fig. 1-2 Mechanism for interfacial conductivity in LAO/STO (Adapted from Ref. 17 and Ref. 15). (a), oxygen vacancies act as donors, providing charge to populate the conducting interface. (b), cation intermixing. The Sr atoms and La atoms near the interface could swap the positions, which dopes the interface. (c), polar catastrophe: for LAO grown on (100) TiO_2 -terminated STO substrate, each LaO^{+1} and AlO^{-1} layer has net charge ($+e$ and $-e$ respectively). Such a stack of the polar layers (LaO^{+1} and AlO^{-1}) results an increasing built-in potential as the LAO thickness increases. When LAO layer exceeds a critical thickness (3 u.c.), electron reconstruction happens under sufficiently large built-in potential, resulting in electrons transfer from surface to the interface. The left figure in (c) shows the charge transfer process, where a half electron per unit cell transfers to the interface. The right figure in (c) is the schematic of the energy bands, showing the 2DEL confined at the interface between LAO and STO.

1.4 EMERGENT PROPERTIES OF LAO/STO HETEROSTRUCTURE

The 2DEL at the LAO/STO interface has drawn widespread attention due to its possession of a remarkable variety of emergent behavior. These emergent properties include tunable metal-insulator transition,^{2,12} strong Rashba-like spin-orbit coupling,^{18,19} superconductivity^{20,21} and ferromagnetism, which cover almost all the fascinating and exotic functionalities in oxide semiconductors.

Tunable Metal-Insulator Transition

In 2006, Thiel *et al.*¹² discovered that the conductivity of the LAO/STO interface can be modulated by LAO thickness or external electric field. Fig. 1-3(a) shows the LAO thickness dependence of LAO/STO interfacial conductivity. The interface demonstrates a sharp insulator-metal transition when the LAO thickness crosses a critical value: $d_c = 3$ u.c. Below d_c , the interface is insulating, while above d_c , the interface becomes conducting. For 3 u.c. LAO/STO, the interface is originally insulating. However, applying a sufficiently large dc bias to the back of the STO substrate can effectively tune the interfacial metal-insulator transition (Fig. 1-3(b)). Such transition can persist even after the back gating is removed. That is to say, hysteretic behavior is observed in the gate tuned metal-insulator transition.

Interfacial Superconductivity

One important question concerns the ground state of the 2DEL system in LAO/STO heterostructures. At low temperature, do the electrons have a ferromagnetic ground state or condense into a superconducting state? In 2007, N. Reyren *et al.*²⁰ reported a superconducting phase in a LAO/STO heterostructure (Fig. 1-3(c)). The measured transition temperature $T_c \approx 200$ mK and the thickness of the superconducting layer is estimated to be ~ 10 nm. Further study

by Caviglia *et al.*²¹ shows an interfacial superconductor-insulator quantum phase transition, controlled by electric field.

Strong Rashba Spin-orbit Coupling

In two dimensional electron systems, inversion symmetry breaking generally occurs along the direction perpendicular to the two-dimensional plane. Such symmetry breaking can lead to a momentum-dependent spin splitting which is identical in form to the Rashba effect seen in many III-V compounds²².

In 2010, Caviglia *et al.*¹⁹ reported that the LAO/STO interface demonstrates large spin-orbit coupling, whose magnitude can be modulated by an external electric field (Fig. 1-3(d)). Their study also reveals a steep rise in Rashba interaction, where a quantum critical point separates the insulating and superconducting states of the system. Similar spin-orbit coupling tuning results are also demonstrated by Shalom *et al.*¹⁸ in magnetotransport measurements.

Interfacial Magnetism and Its Coexistence With Superconductivity

Although both LAO and STO are non-magnetic oxides, the LAO/STO interface shows magnetic signatures in many experiments. By performing magneto-transport measurements, Brinkman *et al.*²³ initiated the magnetism study of LAO/STO. Their measurements show a Kondo like temperature-dependence of the resistance (Fig. 1-3(e)), which indicates the presence of magnetic scattering at the interface. Experiments using DC scanning quantum interference device (SQUID) magnetometry^{24,25}, torque magnetometry²⁶ and X-ray circular dichroism measurements²⁷ suggest such magnetism is intrinsic and resides in-plane along the interface, persisting even up to room temperature.

More interestingly, in the LAO/STO system, studies show a coexistence of superconductivity and ferromagnetism (Fig. 1-3(f))^{24,26,28}. It is most likely that the system displays phase separation where magnetism and superconductivity coexist on the same sample but in different areas of the interface.

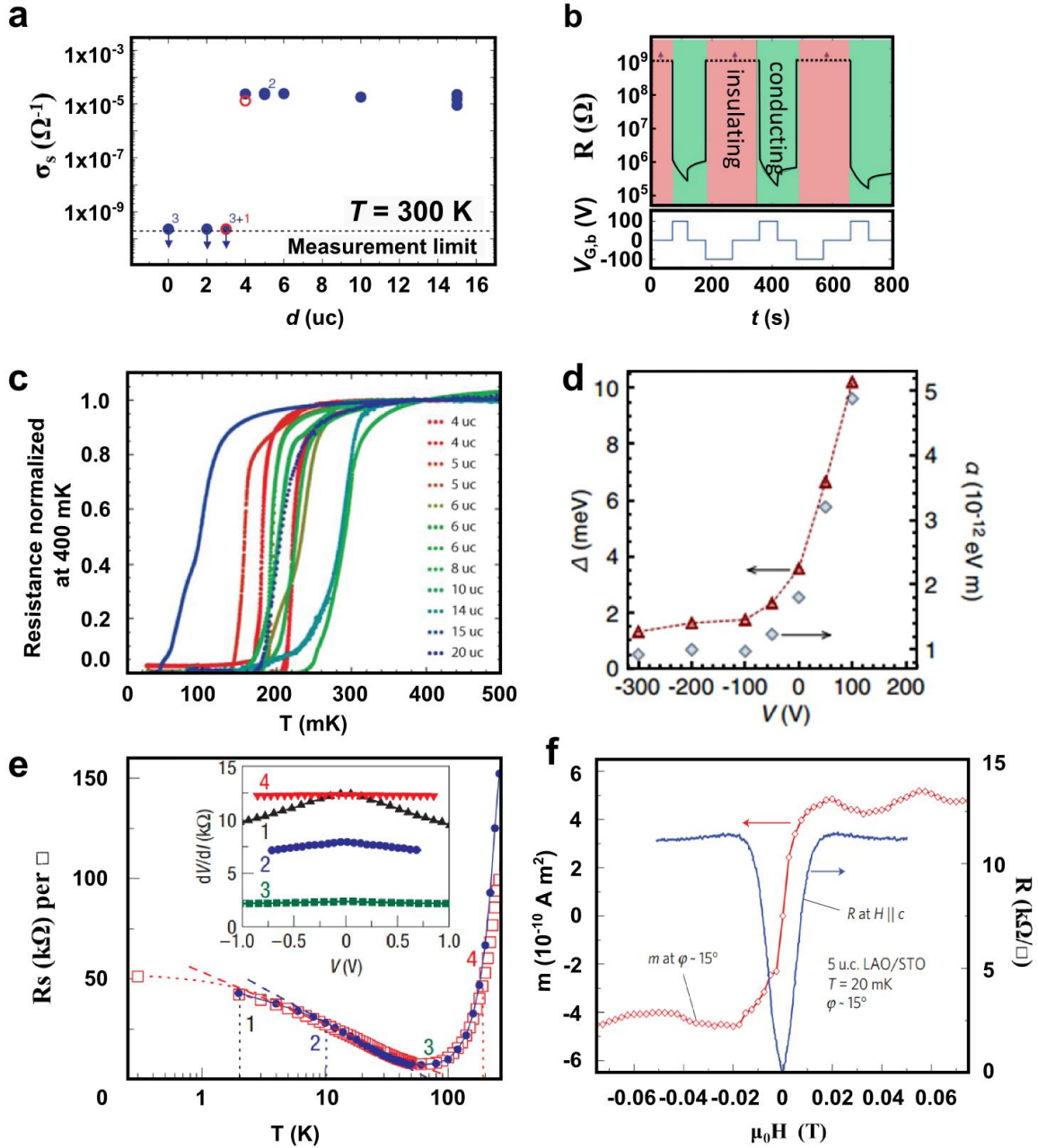


Fig. 1-3 Emergent properties of LAO/STO interface. (a), thickness dependence of interfacial conductivity. (Adapted from Ref. 12) (b), back gate tuning of LAO/STO interface through metal-insulator transition. The dash line in the figure is the measurements up limit. (Adapted from Ref. 12) (c), Superconductivity of LAO/STO interface at low temperature. Results show the transition temperature is around 200 mK. (Adapted from Ref. 20) (d), the red curve is the spin-orbit energy versus gate voltage, showing the size of spin-orbit splitting can be tuned by electric field. The

grey curve shows the field effect modulation of the Rashba coupling constant α . (Adapted from Ref. 19) (e), Temperature dependence of the LAO/STO sheet resistance. The observed logarithmic temperature dependence of the sheet resistance indicates the Kondo effect, suggesting the existence of local magnetic moments. (Adapted from Ref. 23) (f), Coexistence of superconductivity and magnetic ordering in 5 u.c. LAO/STO interface. Plot shows the magnetization m versus the magnetic field H at $T = 20$ mK and R - H curve. (Adapted from Ref. 26)

2.0 EXPERIMENTAL METHOD

This section primarily introduces the routinely used experiment methods during our study of LAO/STO interface structures.

2.1 DEVICE FABRICATION

Photolithography, ion etching and DC sputtering techniques are frequently used to pattern electrode contacts and permanent devices on LAO/STO samples.

Fig. 2-1 illustrates all steps associated with the fabrication of devices. The conventional photolithography method (Fig. 2-1(a-c)) is used to pattern the predesigned structures. During the process, the photoresist (AZ P4210) is first spin-coated uniformly ($\sim 2 \mu\text{m}$ thickness) on the LAO/STO surface (Fig. 2-1(a)) and soft baked at 90°C for 1 minute. Then the sample with photoresist is exposed in UV ($\lambda=365 \text{ nm}$) light with a photomask using a mask alignment system (Fig. 2-1(b)). The photomask can selectively let through the UV light, therefore transferring the predefined pattern onto the resist layer. After UV exposure, the sample is soaked in developer (AZ 400k) and the exposed area will dissolve (Fig. 2-1(c)).

Two types of electrodes are routinely made: (1) electrodes contacting the LAO/STO interface, (2) electrodes deposited directly on the LAO surface.

Fig. 2-1(d-f) depicts steps to fabricate the electrodes to the interface. The sample with patterned photoresist is put in a vacuum chamber and a high energy (2 keV) Ar-ion beam is used to etch trenches deep into the STO (Fig. 2-1(d)). Areas with photoresist covering are protected

from ion beam, while patterned areas with exposed LAO are etched away. After ion milling, metal deposition is performed using the DC sputtering deposition method, where high energy ions bombard the metal target, eject metal atoms and deposit them on the sample surface (Fig. 2-1(e)). The metal is carefully selected for deposition. First, a thin Ti layer (5 nm) is deposited on sample surface, which serves as an adhesive layer. Then a thicker Au layer (25 nm) is added above Ti layer, making an Ohmic contact to the LAO/STO interface. The final step is the photoresist lift-off process. The sample after sputtering deposition is immersed in acetone and experiences ultrasonic cleaning for minutes. The photoresist will dissolve in acetone and the metal rests on photoresist will be washed away, leaving only the patterned electrodes (Fig. 2-1(f)). In some case, there could be photoresist residues on the sample surface. To remove the photoresist residues, samples are cleaned by oxygen plasma cleaner under 100 W for 1 minute.

Fig. 2-1(g-h) illustrates the steps for making top electrodes on the LAO/STO surface. After the photolithography steps (Fig. 2-1(a-c)), the sample is put into vacuum chamber for metal deposition using the DC sputtering deposition method (Fig. 2-1(g)), which is similar to the process in Fig. 2-1(e). The final photoresist lift-off process (Fig. 2-1(h)) is the same as that is described in Fig. 2-1(f). After the photoresist is removed by acetone, the top electrodes are patterned on LAO/STO.

Fig. 2-2 show a picture of a typical processed sample. The sample size is typically 5 mm by 5 mm. The electrodes on the sample surface contact the LAO/STO interface and define the $30\ \mu\text{m} \times 30\ \mu\text{m}$ canvas for conductive AFM lithography experiments. To obtain electrical access to the sample, the LAO/STO sample is glued to a ceramic chip carrier and gold wires are used to make connections by a wire bonding machine. (Fig. 2-2(b))

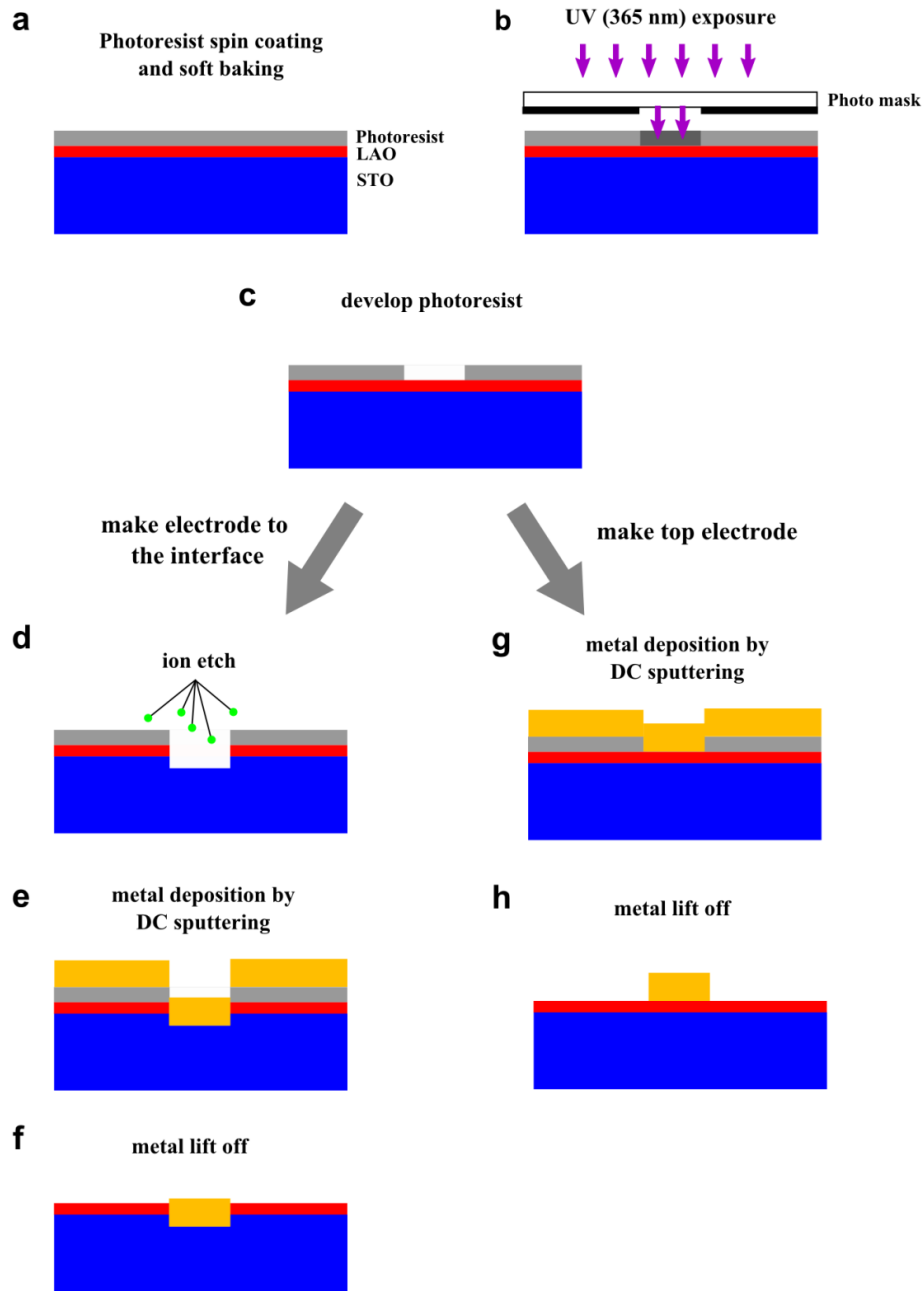


Fig. 2-1 Illustration of typical device fabrication process. (a), photoresist spin coat and soft bake. (b), UV exposure using Hg lamp I-line (365 nm). (c), photoresist development step. For positive photoresist, the exposed areas will be dissolved in developer. (d), ion milling step. High energy Ar^+ will etch away the material. (e), (g), metal deposition using DC sputtering deposition method. (f), (h), photoresist lift off step, which strips off the photoresist and the metal

on it. (a-f), detailed steps to make electrodes that contact to the LAO/STO interface. (a-c, g-h), detailed steps to fabricate the top electrodes on LAO.

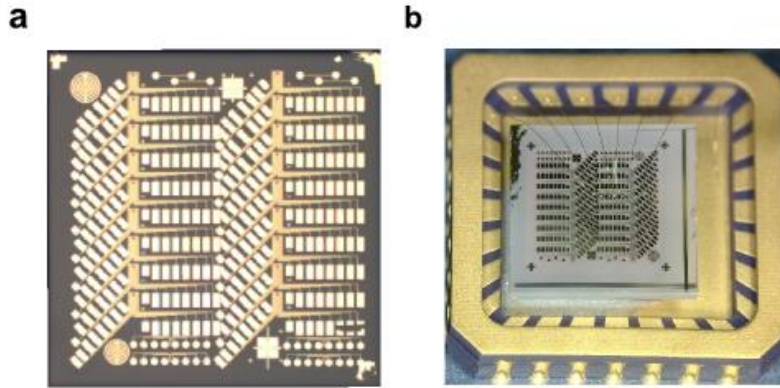


Fig. 2-2 Fabricated devices on LAO/STO. (a), Fabricated electrodes on 3 u.c. LAO/STO. The LAO/STO size is 5 mm by 5 mm. (b), sample with devices is glued on the chip carrier using silver epoxy and the electrical connections to the fabricated patterns are made by gold wires a using wire bonding machine.

2.2 ATOMIC FORCE MICROSCOPY (AFM)

The atomic force microscopy (AFM) is a very high-resolution type of scanning probe microscopy. It can resolve molecules²⁹ on a sample surface and even achieve atomic resolution³⁰. The AFM was first invented by Binnig, Quate and Gerber in 1986³¹. Since then, many variations were developed based on AFM, which include a variety of force sensing (electric force, magnetic force, Casimir forces, etc.), lithography (local oxidation lithography, dip pen lithography, etc.), nanomanipulation and nanoindentation. In addition, ultra-fast scanning (>100 Hz/line³²) and multi-probe technique (>10 million tips³³) are also developed to increase the throughput of AFM, giving it wider applications in industry. To sum up, nowadays, AFM is a mature technique that is widely

used in surface imaging, material properties characterization and matter manipulating at the nanoscale.

Compared with other microscopy techniques, AFM possesses many unique advantages. For example, while scanning tunneling microscopy (STM) requires the sample to be conductive or receive special treatment, such as metal-coating, AFM can work well on most types of samples, regardless of their conductivity. While electron microscopies, such as scanning electron microscopy (SEM) or transmission electron microscopy (TEM), generally needs to operate in vacuum environment, AFM can work in much more flexible environments, including liquids. As for the imaging quality, AFM demonstrates higher resolution than SEM and comparable resolution with TEM and STM. In fact, true atomic resolution can be achieved using AFM in both ultra-high vacuum (UHV) environment and liquid environment.³⁰

There are also limitations of AFM: AFM cannot scan as fast as SEM. The AFM scanning speed is limited by the scanner, AFM probe and also the electronic systems. Other limitations of AFM are the scan size and scan depth. A typical commercial AFM usually can handle a maximum scan size up to hundreds of microns and maximum surface height up to tens of microns. However, SEM can easily get the image area on the order of square millimeters with the depth of field also on the order of millimeters. One possible way to increase the AFM scan size is to use parallel probes to do simultaneous scanning.

2.2.1 AFM working principle

The AFM is a high resolution microscopy that uses a cantilever with a sharp tip (the radius of curvature $\rho \sim \text{nm}$) at its end to scan the specimen surface. When the tip is brought to the proximity of the sample surface, forces between the tip and the sample will cause the cantilever to

deflect. To measure the cantilever deflection, the most popular way is using the optic level system, where a laser beam incident on the top surface of the cantilever is deflected to a quad-segmented photodiode. The analog output of the photodiodes is called deflection, which is related to the force between the tip and the sample surface. Depending on the tip-sample interaction, AFM measured forces include mechanical contact force, van der Waals forces, capillary forces, chemical bonding, electrostatic forces, magnetic forces, Casimir forces, and solvation forces. Information such as surface topography, electric potential, magnetic moment, and chemical bonding energy can also be retrieved from AFM measurements.

2.2.2 Contact mode

One of the AFM basic functions is to measure the topography of a sample. Contact-mode AFM was the first mode developed for this purpose. In contact mode, the tip is brought into direct contact with the sample surface. The overall force between tip and sample is repulsive, which is indicated as the red region in the force-distance curve (Fig. 2-3).

A schematic diagram of contact-mode AFM operation is shown in Fig. 2-4. When the tip engages on a sample surface, the tip exerts a force to the sample. Given by Hooke's law, the force

$$F = -k \cdot D \quad (2-1)$$

where k is the cantilever's spring constant and D is the deflection distance. During the scanning, the tip-sample interaction force F is kept constant using a feedback circuit via height adjustment. The deflection signal D from the photodiodes serves as the error signal in the feedback loop and the feedback output control the piezo movements in the Z direction. The surface topography is obtained by spatially mapping out the Z piezo height change during the scanning.

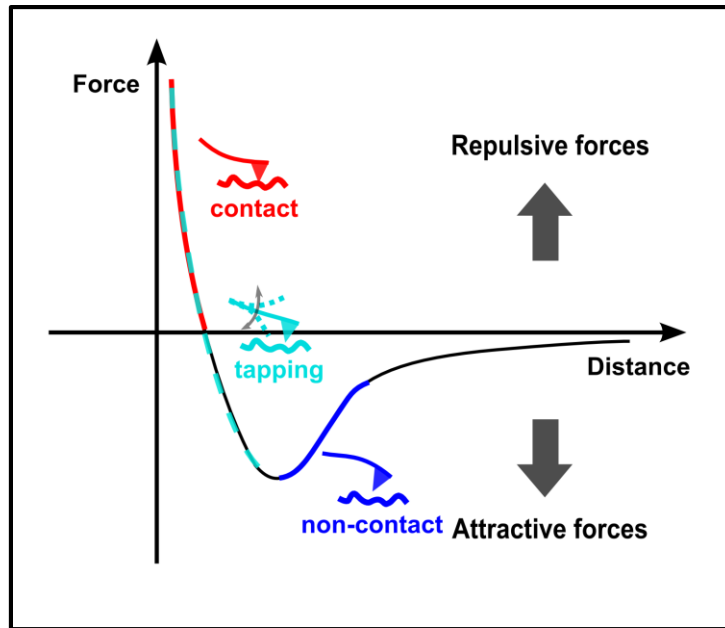


Fig. 2-3 Illustration of force-distance curve and corresponding AFM image modes.

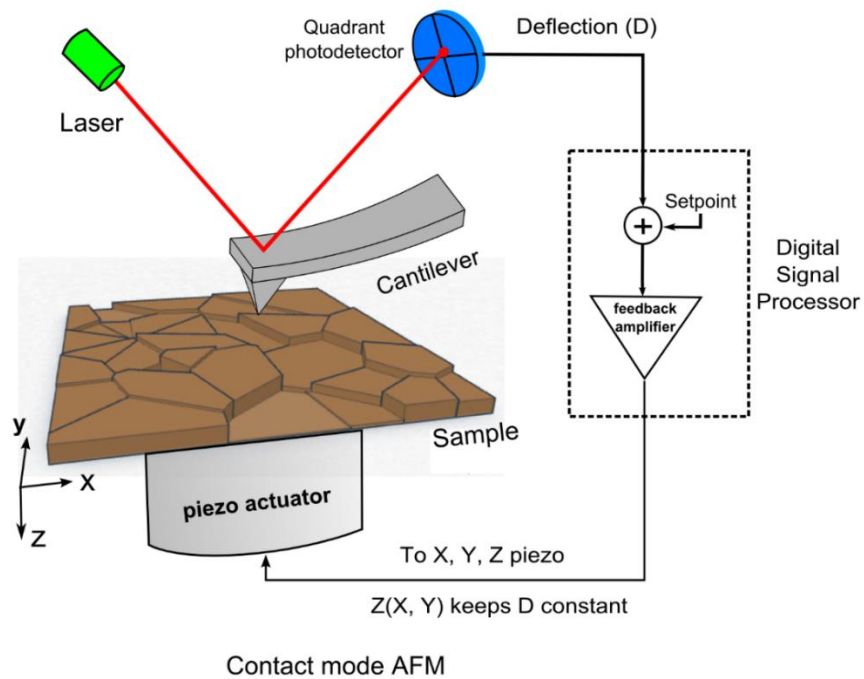


Fig. 2-4 Schematic diagram of the essential components for contact mode AFM.

2.2.3 AC mode

Another most commonly used AFM scanning mode is called AC mode. In contact mode, the AFM cantilever is static. However, in AC mode, the cantilever is dynamic. As it is shown in Fig. 2-5, a shake piezo is used to mechanically drive the cantilever to oscillate at its resonant frequency ω . Depending on the tip-sample distance, the interaction between the tip and sample surface could be repulsive (cyan dash line in Fig. 2-4) or attractive (blue line in Fig. 2-4), corresponding to tapping AC mode or non-contact AC mode separately. During the scan, the cantilever's oscillation amplitude (A) and phase (θ) are measured by the lock-in amplifier. To obtain the surface topography, the feedback circuit is used to maintain the tip-sample interaction to be constant via the height adjustment. The amplitude signal A serves as the error signal in the feedback loop and the Z piezo movements, which are controlled by feedback output, map out the sample surface profile.

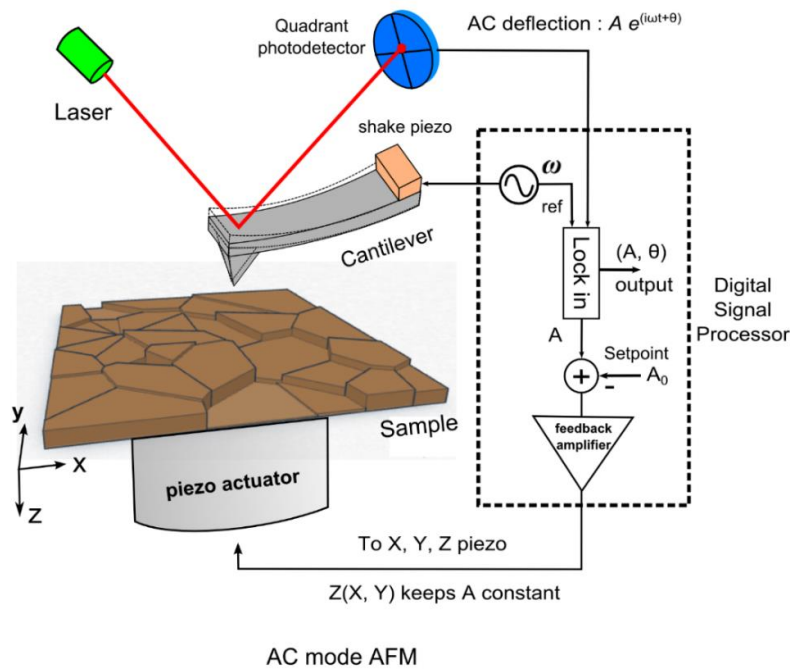


Fig. 2-5 Schematic diagram of the essential components for AC mode AFM.

2.2.4 Piezoresponse force microscopy (PFM)

One important application of AFM is piezoresponse force microscopy (PFM), which is used to characterize the electromechanical response of piezoelectric materials. Piezoelectric materials possess interesting properties: when an external stress is applied to the material, an internal electric potential is generated due to the induced dipole moments, giving rise to a macroscopic electric voltage across the material. The reverse effect is also observed in piezoelectric material. When an external electric field is applied, the piezoelectric material shows mechanical deformations, either expansion or contraction. Within the piezoelectric material, some crystals show spontaneous non-zero net polarization even without mechanical stress and they are called ferroelectric. The PFM technique is commonly used to characterize the ferroelectricity in ferroelectric material.

Fig. 2-6 illustrates the PFM working principles. In PFM mode, a conductive cantilever (heavily doped silicon tip or metal coated tip) scans over the sample surface in contact mode (Fig. 2-6(a)). Meanwhile, an AC excitation at frequency ω is applied to the tip and the sample is back grounded. Such AC modulated electric field runs across the ferroelectric material and causes a structure distortion which in turn leads to a periodic deflection (AC deflection) of the cantilever. By using a lock-in amplifier, the amplitude and phase of the AC deflection at frequency ω can be measured, which contain the information of sample spontaneous polarization direction and material piezoelectric strain constant.

The typical piezoresponse under external field is illustrated in Fig. 2-6(b). When the external electric field is parallel to the sample polarization direction, the material expands. When the external electric field is anti-parallel with the sample polarization direction, the material

contracts. Depending on the sample's initial polarization direction, the material surface deformation could oscillates in-phase or 180 degrees out-of-phase with the applied AC excitation.

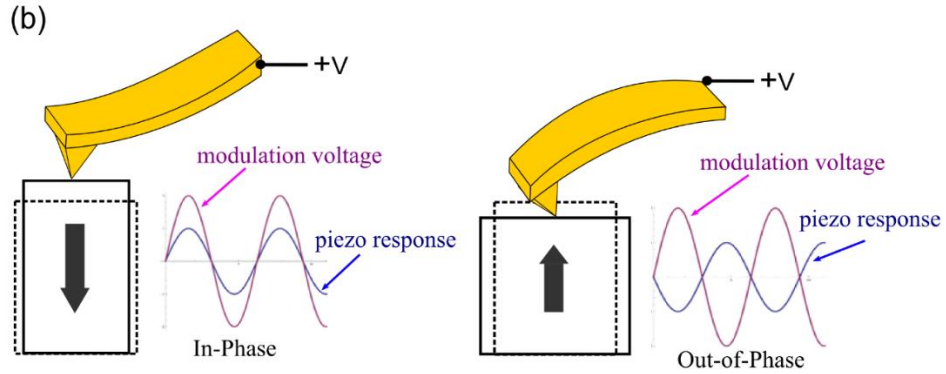
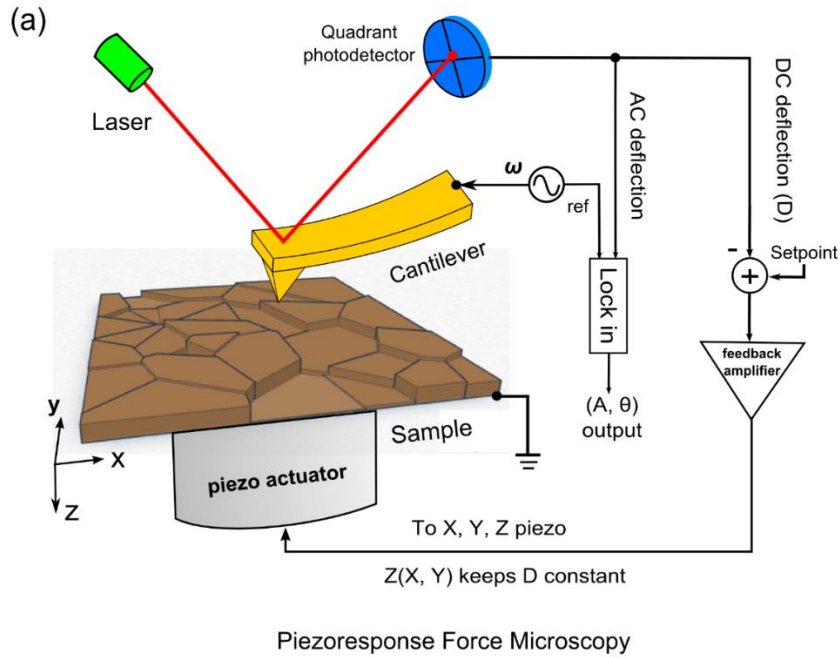


Fig. 2-6 Piezoresponse force microscopy illustration.(a), Schematic diagram of the essential components for piezoresponse force microscopy. (b), Illustration of in-phase and 180 degrees out-of-phase piezoresponse.

2.2.5 Quantitative PFM analysis

The PFM can be used to quantitatively measure the electrical field induced surface deformation. This section will discuss the details about PFM data analysis.

In the PFM set up, the dc+ac excitation voltage can be applied across the piezoelectric material.

$$V(t) = V_{dc} + V_{ac} = V_{dc} + V_{PFM} \cos(2\pi f_{PFM} t) \quad (2-2)$$

Here the V_{PFM} and f_{PFM} are the amplitude and frequency of ac modulation. The sample's surface deformation comes from the piezoelectric effect under both the dc and ac field. It can be expressed as

$$z = z_{dc} + z_{ac} \quad (2-3)$$

In Eq. (2-3), z_{dc} is the structure distortion due to the applied dc field

$$z_{dc} = \int_0^{V_{dc}} d_{33}^{eff}(V_{dc}) \cdot dV \quad (2-4)$$

where d_{33}^{eff} stands for the effective strain tensor component that directly couples into the vertical motion of the cantilever. z_{ac} represents the structure distortion due to the modulated ac field, which can be written as:

$$\begin{aligned} z_{ac} &= A_z(f_{PFM}, V_{PFM}, V_{dc}) \cdot \cos(2\pi f_{PFM} t + \varphi_0) \\ &= d_{33}^{eff}(V_{dc}) \cdot V_{PFM} \cdot \cos(2\pi f_{PFM} t + \varphi_0) \end{aligned} \quad (2-5)$$

Here $A_z(f_{PFM}, V_{PFM}, V_{dc})$ is the surface deformation amplitude under ac field modulation and the phase $\varphi_0 = 0$ or π , depending on the sample's polarization direction (Fig. 2-6(b)).

With the AFM tip contacting to the sample surface, the modulated surface deformation (z_{ac}) drives the cantilever to oscillate, the amplitude of which is measured by a lock-in amplifier

via the ac deflection signal. Considering that the piezoresponse is either in-phase or 180 degree out-of-phase with the excitation (Fig. 2-6(b)), only the X-output of the lock-in amplifier serves as the PFM signal. Here we denote the lock-in X-output as $X(f_{PFM}, V_{PFM}, V_{dc})$ and the sensitivity of AFM as α . Then the amplitude of AFM tip oscillation $A_{tip}(f_{PFM}, V_{PFM}, V_{dc})$ will be:

$$A_{tip}(f_{PFM}, V_{PFM}, V_{dc}) = X(f_{PFM}, V_{PFM}, V_{dc}) \cdot \alpha \quad (2-6)$$

(For our Cypher AFM, the sensitivity $\alpha = 67.75 \text{ nm/V}$, which is obtained from the AFM force-distance curve.)

The coupling between modulated surface deformation and tip displacement depends on the excitation frequency f_{PFM} . In conventional PFM, f_{PFM} is far below the AFM tip's contact resonant frequency f_0 , therefore

$$A_z(f_{PFM}, V_{PFM}, V_{dc}) = A_{tip}(f_{PFM}, V_{PFM}, V_{dc}) \quad (2-7)$$

In conventional PFM, the piezoresponse signal is usually very small and for some material the signal could be too small to be detected. A modern method is called contact resonance PFM, in which the excitation frequency f_{PFM} is chosen close to the AFM tip's contact resonant frequency f_0 . Due to the contact resonant enhancement, the tip's oscillate amplitude will be amplified:

$$A_z(f_{PFM}, V_{PFM}, V_{dc}) \cdot Q = A_{tip}(f_{PFM}, V_{PFM}, V_{dc}) \quad (2-8)$$

Here Q is the quality factor of the tip-surface contact resonance system. Based on Eq. (2-5), (2-6) and (2-8), the sample's tensor component $d_{33}^{eff}(V_{dc})$ can be calculated as:

$$d_{33}^{eff}(V_{dc}) = \frac{X(f_{PFM}, V_{PFM}, V_{dc}) \cdot \alpha}{Q \cdot V_{PFM}} \quad (2-9)$$

From Eq. (2-4) and Eq.(2-9), the AFM tip probed surface displacement due to external dc field can be obtained as follows:

$$z_{dc}(V_{dc}) = \int_0^{V_{dc}} \frac{X(f_{PFM}, V_{PFM}, V_{dc}) \cdot \alpha}{Q \cdot V_{PFM}} dV \quad (2-10)$$

The quality factor Q can be obtained by fitting the contact resonance curve using a simple harmonic oscillator (SHO) model:

$$A(f) = \frac{A^{max} f_0^2}{\sqrt{(f^2 - f_0^2)^2 + (f \times f_0 / Q)^2}} \quad (2-11)$$

2.2.6 Magnetic force microscopy (MFM)

When the AFM tip is coated with magnetic materials, such as CoCr, it can be used to detect the magnetic properties of the sample. Such technique is called magnetic force microscopy (MFM).

In MFM mode ([Fig. 2-7\(a\)](#)), the cantilever is mechanically driven by a piezoelectric transducer near its resonant frequency and kept a constant height Δh above the surface. When the tip is placed in proximity to a sample, the cantilever's resonant motion is altered in ways that can be traced directly to the force gradient $\partial F_z / \partial z$, which in turn produces changes in the amplitude ΔA , phase $\Delta \varphi$ and frequency Δf of the cantilever resonance:

$$\Delta A \approx \frac{2A_0Q}{3\sqrt{3}k} \cdot \frac{\partial F_z}{\partial z} \quad (2-12)$$

$$\Delta\phi \approx \frac{Q}{k} \cdot \frac{\partial F_z}{\partial z} \quad (2-13)$$

$$\Delta f_0 \approx -\frac{1}{2k} \cdot \frac{\partial F_z}{\partial z} \cdot f_0 \quad (2-14)$$

The MFM can be performed using either the frequency modulation method or slope detection method. For the frequency modulation method, a 90° phase shift between the cantilever drive and response is maintained using a feedback loop. The frequency shift $\Delta f = f' - f$ (Fig. 2-7(b)) is detected as the MFM signal. For the slope detection method, the cantilever oscillates at a fixed frequency f_0 near resonance (Fig. 2-7(b)). The changes in amplitude ΔA and phase $\Delta\phi$ are recorded as MFM signals.

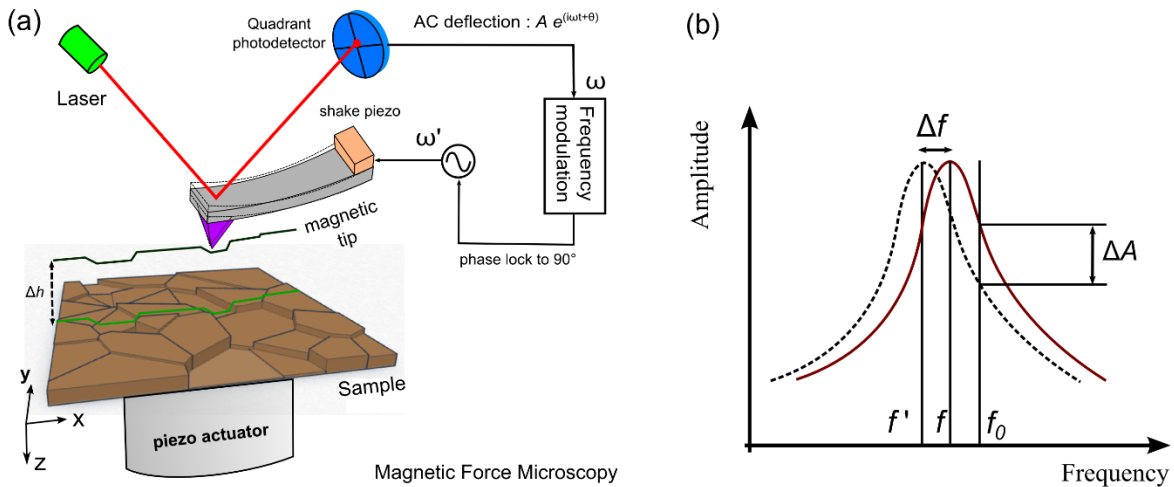


Fig. 2-7 Magnetic force microscopy illustration. (a), Schematic diagram of important components for MFM using frequency modulation. (b), Illustration of tip resonant curve shift due to magnetic interaction. For the frequency modulation method, the excitation frequency is modulated by feedback loop and the frequency shift $\Delta f = f' - f$ serves as the MFM signal. For the slope detection method, the excitation frequency is fixed and the amplitude, phase signal change serves as the MFM signal.

2.2.7 Magneto-electric force microscopy (MeFM)

The magnetoelectric effect, observed in certain single phase and composite materials such as Cr_2O_3 , is the phenomenon of inducing magnetization (\mathbf{M}) by applying an external electric field (\mathbf{E}) or that of an electric polarization (\mathbf{P}) by applying a magnetic field (\mathbf{B}). Based on the MFM with *in-situ* modulated \mathbf{E} field, the MeFM technique was first used to locally detect the \mathbf{E} -induced magnetic signal and spatially image the coupling between the magnetic and electric dipoles in magnetoelectric materials³⁴.

In our study, the MeFM method is employed to explore the connection between ferromagnetism and electric field tuned carrier density. Fig. 2-8 shows the MeFM setup. Rather than driving the tip mechanically, the sample is driven with a static and sinusoidally modulated voltage. The modulated sample magnetization periodically changes the magnetic force, driving the tip resonantly and producing a cantilever oscillation that is detected with a lock-in amplifier.

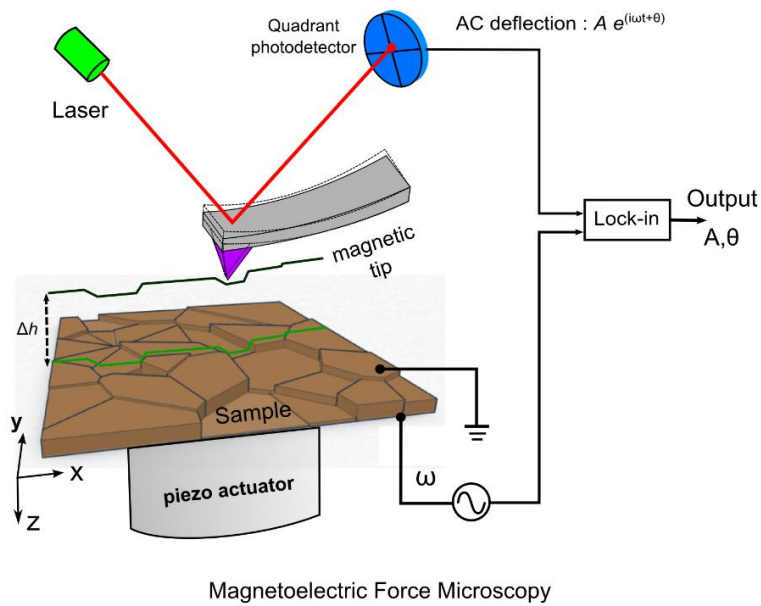


Fig. 2-8 Magneto-electric force microscopy illustration.

2.3 C-AFM LITHOGRAPHY ON LAO/STO

2.3.1 Introduction

As discussed in Section 1.4, for LAO with a critical thickness (3 u.c.) on STO, the interfacial conductivity can be macroscopically modulated through the metal to insulator transition by back gating. Our group first demonstrated that such kind of interfacial metal-insulator transition can also be locally controlled using a biased AFM tip³⁵. The conductive AFM probe on LAO surface serves as a nanoscale top gate (tens of nm size). Applying a dc bias to the conductive AFM probe will generate a strongly localized electric field across LAO/STO and do charge doping on the LAO surface. For 3 u.c. LAO/STO, the polar catastrophe model (Section 1.3) suggests that the built-in potential is not big enough to induce the electronic reconstruction at the interface and thus the interface is originally insulating. However, a positively biased (5~10 V) AFM tip can write positive charges on the LAO surface³⁶, making the potential large enough to induce polar catastrophe and consequently switch the insulating interface to be conducting. On another hand, the negatively biased AFM tip can remove the doped positive surface charges, making the interface restore to the insulating state. Such conductive AFM (c-AFM) lithography technique provides a robust way to sketch conducting nanostructures on the LAO/STO interface. The flexibility and convenience of such c-AFM method make it a powerful tool to fabricate nano-circuits and study the low dimensional (1D) physics in the oxide system.

2.3.2 c-AFM lithography in contact mode

Fig. 2-9 shows the c-AFM lithography in 3 u.c. LAO/STO heterostructures. For the writing process (Fig. 2-9(a)), the AFM tip is biased with +3 V and scans from one electrode to another in contact mode. As soon as the tip reaches the second electrode, the conductance between two electrodes shows an abrupt jump. Considering that both electrodes contact to the interface and the LAO surface is always insulating during the writing, such conducting channel (green line in Fig. 2-9(a)) must form at the LAO/STO interface. Such created conducting nanowire can also be erased (Fig. 2-9(b)). As the AFM tip cuts across a written nanowire with a negative voltage, e.g. -3 V, the conductance between two electrodes drops to the insulating value and a gap forms at the middle of the nanowire. By fitting the drop of conductance curve, the nanowire width is determined to be as small as 2 nm.

The c-AFM method created nanostructures at the LAO/STO interface can also be directly imaged using piezoresponse microscopy.³⁷ Fig. 2-9(c) shows the lithography between two Au electrodes. A nanowire (green line) is written by AFM tip with +8 V at the speed of 600 nm/s and then cut with -10 V at the speed of 10 nm/s. A 500 nm × 500 nm PFM image is taken over the written area (Fig. 2-9(d)). The nanowire as well as the junction is clearly visualized in PFM image. The imaged wire resolution is limited by tip sharpness.

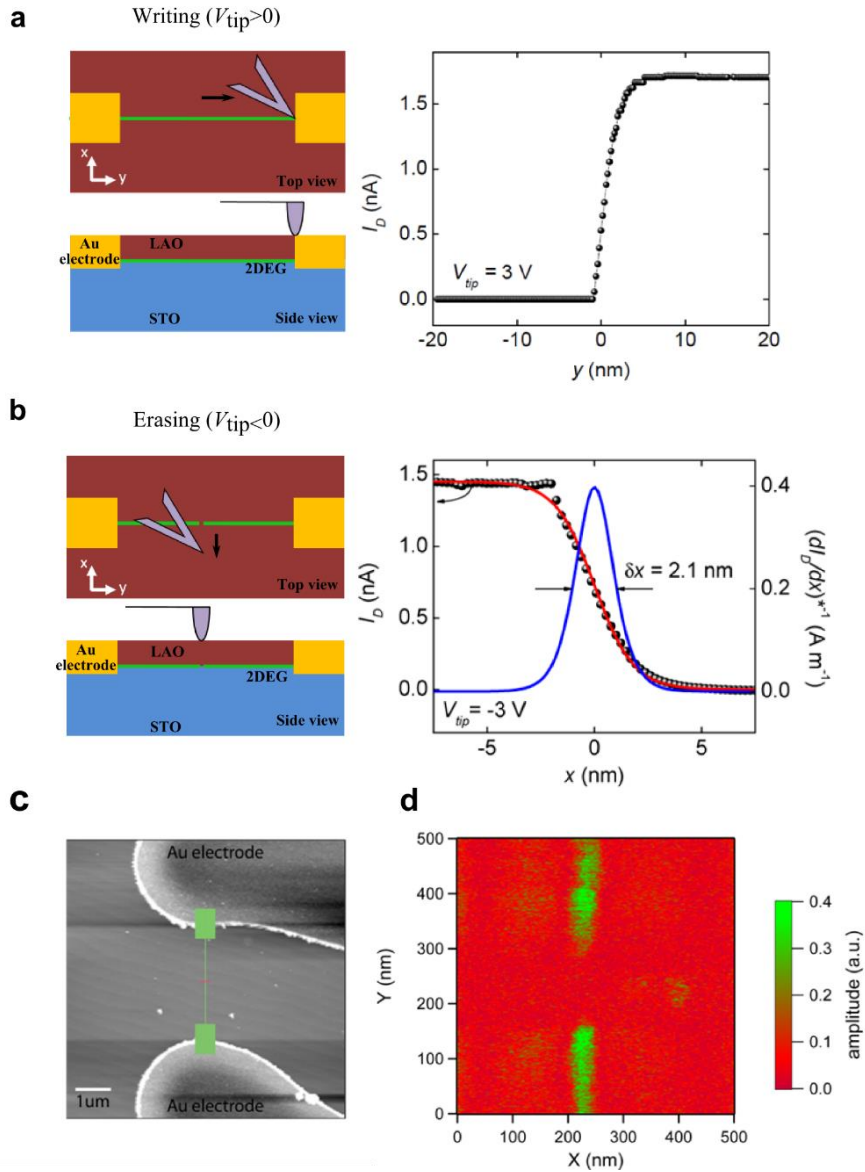


Fig. 2-9 Conductive AFM lithography in 3 unit cell LAO/STO heterostructures. (a), c-AFM writing process with positive biased AFM probe. (b), c-AFM erasing process with negative biased AFM probe. (c), AFM image of LAO/STO surface with fabricated Au electrodes contacting to the interface. The writing pattern (illustrated as the green region) consists of two square virtual electrodes and a nanowire. The cutting pattern is a short path (indicated as the red wire) right across the written nanowire. (d), PFM image of the c-AFM lithography pattern in (c), which directly visualizes the conducting channels at LAO/STO interface. (Data in (a-b) is adapted from Ref. 35. (c-d) is adapted from Ref. 37.)

2.3.3 Sketched high performance nanodevices

The c-AFM lithography method makes LAO/STO an open platform for high performance nanoelectronics fabrication. Fig. 2-10(a) demonstrates the field effect transistor, where source, drain and gate leads are written by a biased AFM tip. Such sketched transistor shows extremely high on-off current ratio (Fig. 2-10(b)), making it a great component for logic elements.³⁸ Fig. 2-10(c) shows that the written nano junction can serve as a sensitive photodiode.³⁹ With a laser illumination, a highly localized photo-current can be detected on the junction (Fig. 2-10(d)). The electric rectifier (Fig. 2-10(e)) can also be written with an AFM tip using an asymmetric voltage (e.g. triangular wave from -10 V to 10 V). The *I-V* characterization (Fig. 2-10(f)) demonstrates such device can be used to do electric rectification.⁴⁰ In addition, our group successfully made the first sketch single electron transistor in LAO/STO using the c-AFM method. The conducting island is as small as several nanometers. By using the side gate, a single electron can be precisely controlled to tunnel in or out of the center island. Such device shows great potential of application in quantum computation.⁴¹

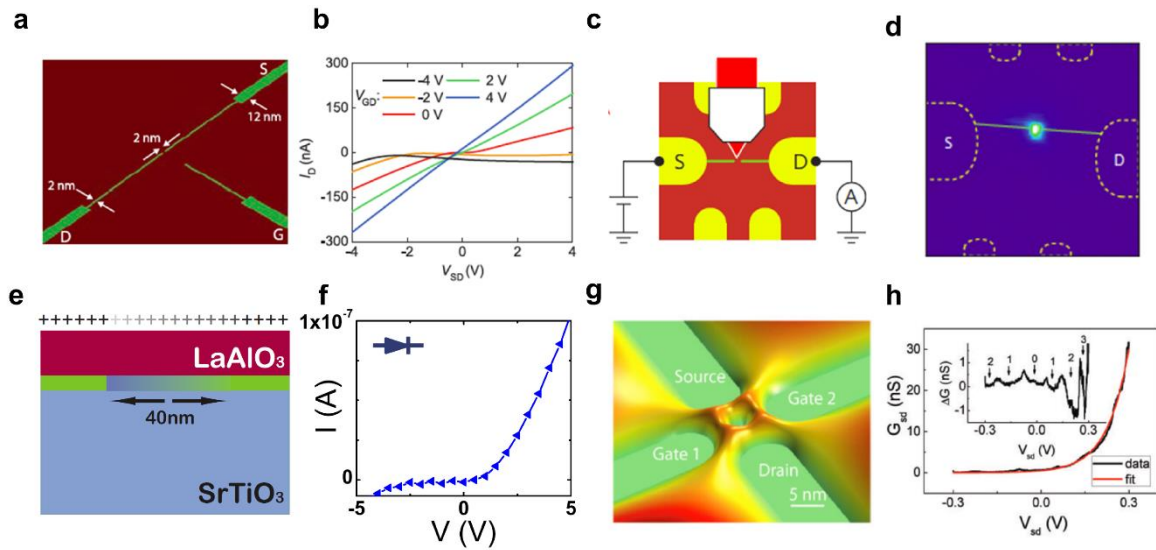


Fig. 2-10 Sketchable high performance nanoelectronics. (a-b), nanoscale field effect transistor and the gate tuning of IV curve. (Adapted from Ref. 38) (b-c), highly sensitive photodetector and the photocurrent image. (Adapted from Ref. 39) (e-f), nano diode and the IV performance. (Adapted from Ref. 40) (g- h), sketch single electron transistor with the Colum peaks resolved in the electric transport measurements. (Adapted from Ref. 41)

2.3.4 Possible mechanism

One possible mechanism for the writing process involves the adsorbed H_2O , which dissociates into OH^- and H^+ on the LAO surface. First principles calculations⁴² show H_2O binds strongly to the AlO_2 outer surface and dissociates into OH^- and H^+ adsorbates. (Fig. 2-11(a)) During the writing process, the positively biased AFM probe removes some of the OH^- adsorbates, thus locally charging the top surface with an excessive H^+ ions (Fig. 2-11(b)). This charge writing, which has also been observed for bulk LaAlO_3 crystals⁴³, acts to dope the LAO/STO interface and consequently switch the interface from insulating to conducting. During the erasing process, the negatively biased AFM probe removes H^+ adsorbates, restoring the OH^- - H^+ balance, and the

interface reverts back to an insulating state (Fig. 2-11(c)). We refer to this process as a "water cycle" because it permits multiple writing and erasing without physical modification of the oxide heterostructures.

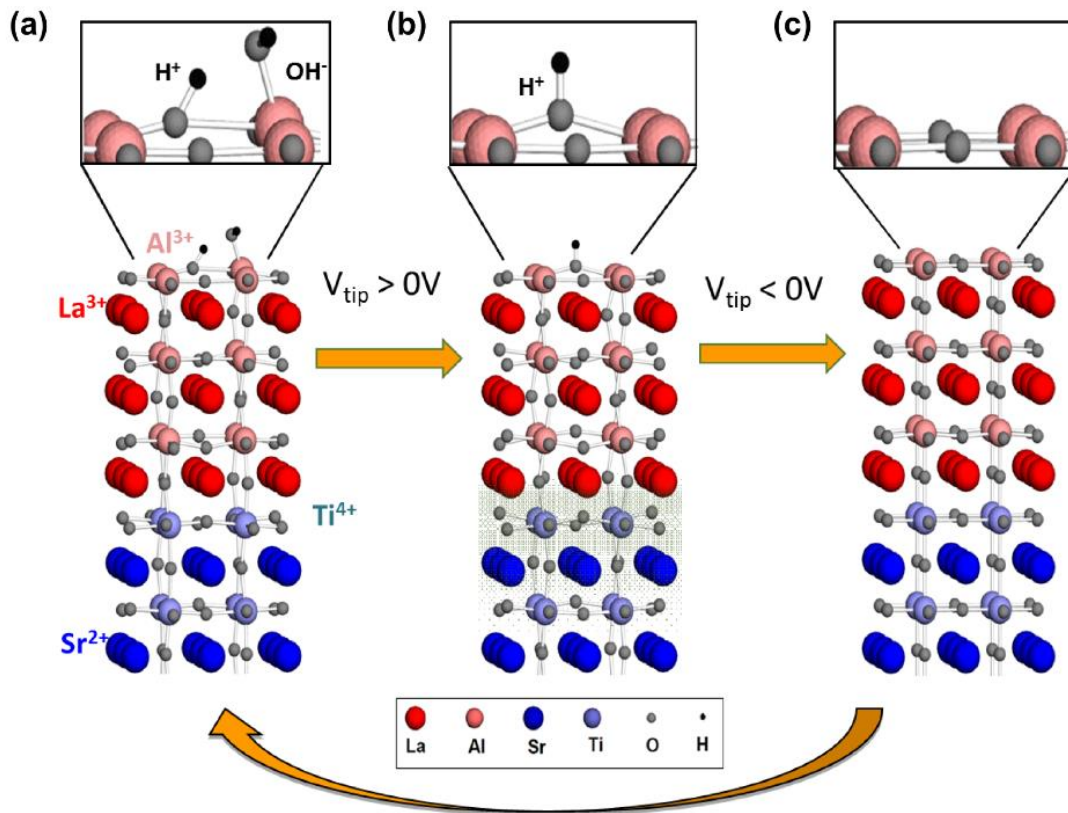


Fig. 2-11 "water cycle" mechanism for c-AFM lithography on LAO/STO. (a), Layer of water spontaneously adsorbed at the LaAlO₃ top surface. (b), Positive tip bias removes OH⁻, leaving H⁺ adsorbate and producing a metallic interface. (c), Negative tip bias removes residual H⁺ and restores the initial insulating state. (Adapted from C. S. Hellberg, APS talk)

3.0 'WATER CYCLE' MECHANISM FOR WRITING AND ERASING NANOSTRUCTURES AT THE $\text{LaAlO}_3/\text{SrTiO}_3$ INTERFACE

Nanoscale control of the metal-insulator transition in $\text{LaAlO}_3/\text{SrTiO}_3$ heterostructures can be achieved using local voltages applied by a conductive atomic-force microscope probe. One proposed mechanism for the writing and erasing process involves an adsorbed H_2O layer at the top LaAlO_3 surface. Under the scenario, water molecules dissociates into OH^- and H^+ which are then selectively removed by a biased AFM probe. To verify such proposed mechanism, writing and erasing experiments are performed in a vacuum AFM using various gas mixtures. Writing ability is suppressed in those environments where H_2O is not present. The stability of written nanostructures is found to be strongly associated with the ambient environment. The self-erasure process in air can be strongly suppressed by creating a modest vacuum or replacing the humid air with dry inert gas. These experiments provide strong constraints for theories of both the writing process as well as the origin of interfacial conductance.

3.1 INTRODUCTION

The discovery of a high mobility quasi-two-dimensional electron gas (q-2DEG) at the $\text{LaAlO}_3/\text{SrTiO}_3$ (LAO/STO) heterointerface¹ has drawn great interest towards its transport property^{1,12,20,35}, potential devices application^{35,38-40} and its physical mechanism^{10,15,44-47}. One defining characteristic of this family of heterostructures is the abrupt transition from an insulating to conducting interface for $n \geq 4$ unit cells¹². (We define n u.c.-LAO/STO to refer to n unit cells

of LaAlO₃ grown on TiO₂-terminated SrTiO₃.) To explain this transition, a number of mechanisms have been offered including electronic reconstruction (sometimes referred to as “polar catastrophe”)¹⁵, structural deformations⁴⁷, unintentional or intrinsic dopants¹⁰, interfacial intermixing⁴⁵ and oxygen vacancies⁴⁴. Theoretical investigations have predicted a critical thickness ranging from $n=3-4$ u.c.⁴⁸. For 3 u.c.-LAO/STO structures, reversible nanoscale control of the metal-insulator transition was reported³⁵. Positive voltages applied to a conductive atomic force microscope (c-AFM) probe in contact with the top LAO surface produce local conducting regions at the LAO/STO interface; negative voltages restore the interface to its initial insulating state. The process was found to be repeatable over hundreds of cycles³⁸, effectively ruling out an early theory involving the formation of oxygen vacancies at the top LAO surface³⁵. Conducting regions were found to be stable under atmospheric conditions for ~ 1 day, and indefinitely under vacuum conditions³⁸.

A physical understanding of the writing and erasing mechanism is important for fundamental reasons and also for the development of future technologies that are based on the stability of these nanostructures. Conducting islands with densities >150 TB/in² have been demonstrated³⁵, and transistors with channel lengths of 2 nm have been reported³⁸. Such an understanding can help in the development of conditions that can stabilize these structures over time scales that are relevant for information storage and processing applications (i.e., ~10 years).

3.2 SAMPLE GOWTH

Details about sample growth are discussed in Section 1.2. Thin films (3 u.c.) of LaAlO₃ were deposited on a TiO₂-terminated (001) SrTiO₃ substrates by our collaborators using pulsed

laser deposition with *in situ* high pressure reflection high energy electron diffraction (RHEED)⁴⁹. Growth was at a temperature of 550°C and O₂ pressure of 1×10⁻³ Torr. After growth, electrical contacts to the interface were prepared by milling 25nm deep trenches via an Ar-ion mill and filling them with Au/Ti bilayer (2 nm adhesion Ti layer and 23 nm Au layer). Fig. 3-1(a) shows an example of the fabricated electrodes on a 3 u.c. LAO/STO heterostructure. The electrical contacts confine a 30 μm × 30 μm canvas for AFM writing experiments, as illustrated in Fig. 3-1(b).

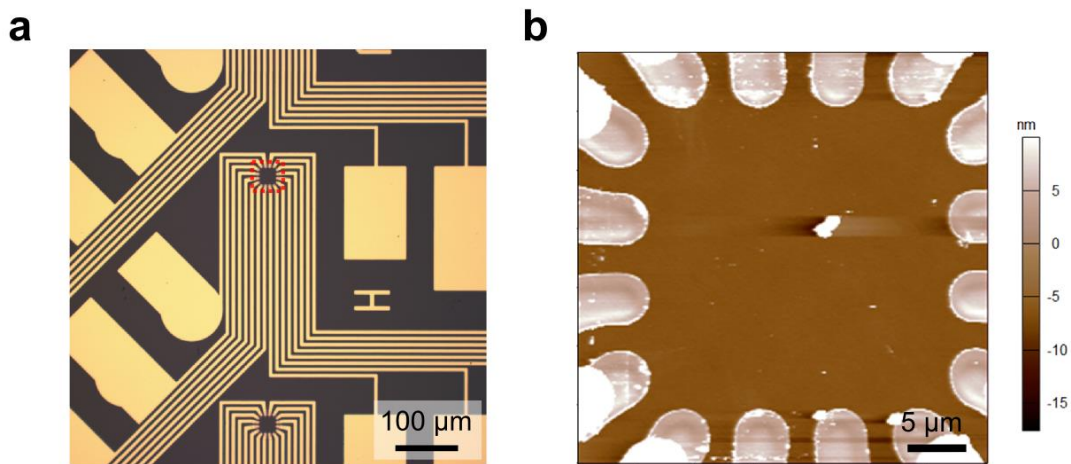


Fig. 3-1 Fabricated electrodes and writing canvas. (a), Fabricated Au electrodes that contact to the LAO/STO interface. The red dash line enclosed region serves as the AFM writing canvas. (b), AFM height image of the writing canvas with multiple electrodes contacting the interface.

3.3 EXPERIMENT SET UP

During the 2009 APS march meeting, Dr. C. S. Hellberg first proposed the "water cycle" mechanism (Discussed in Section 2.3.4). His DFT calculations show that the surface ions play an important role in LAO/STO interfacial conductivity. Here we investigate the writing and erasing

process on 3 u.c.-LAO/STO heterostructures under a variety of atmospheric conditions, in order to constrain physical models of the writing and erasing procedure and the origin of the interfacial electron gas.

To perform c-AFM experiments, a vacuum AFM (Fig. 3-2(a)) is employed that is capable of operation down to 10^{-5} Torr and allows controlled introduction of various gases. Writing and erasing experiments (Fig. 3-2(b-c)) are performed under a variety of conditions. We use the parameter $V_{\text{tip}}=10$ V, litho speed $v = 500$ nm/s for writing and $V_{\text{tip}}=-10$ V, litho speed $v = 10$ nm/s for erasing (the cutting speed is set to be slow in order to obtain a better spatial resolution of cutting, from which we can extract the nanowire width). The conductance of nanostructures is monitored in real time by a lock-in amplifier as the ambient gaseous environment is modified in a controlled fashion. Here conductance is defined as $G=I_{RMS}/V_{RMS}$. A sinusoidal voltage (amplitude 0.4 V_{RMS} , frequency 23 Hz) is applied to one electrode, and the resulting current I_{RMS} from the second electrode is measured by the lock-in amplifier. The pressure in the experiment is monitored using an ion gauge, which operates over a range Atmosphere - 10^{-9} Torr, with an accuracy $\pm 15\%$ < 100 mbar and $\pm 30\%$ below 10^{-3} mbar. Prior to the writing the LAO surface is raster-scanned twice with $V_{\text{tip}} = -10$ V and $V_{\text{tip}} = +10$ V alternatively, to remove any adsorbates on the LAO surface.

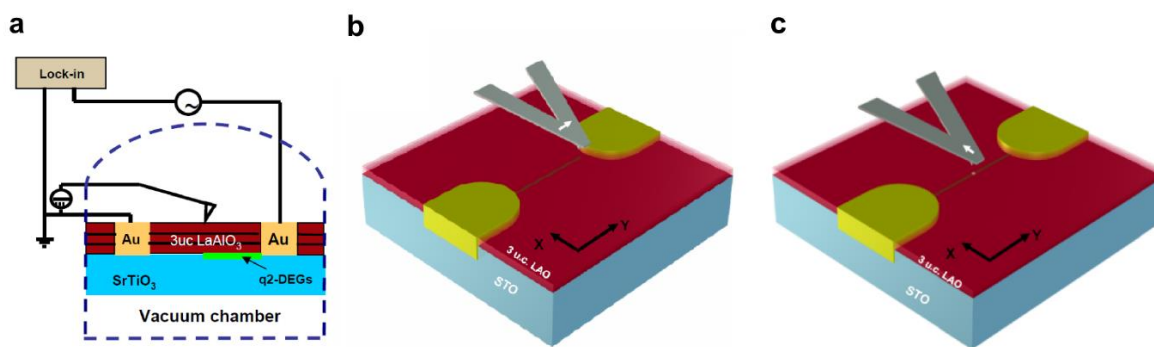


Fig. 3-2 Writing and erasing nanowires at the 3u.c. LaAlO₃/SrTiO₃ interface. (a) Side view schematic illustration about how a conducting AFM probe writes a nanowire. (b) Top view schematic of a writing experiment in which a nanowire is created with a positive biased tip. (c) Top view schematic of a cutting experiment in which a nanowire is locally erased with a negatively biased tip.

3.4 WRITING AND ERASING UNDER CONTROLLED ENVIRONMENT

A straightforward test of the water cycle mechanism outlined above replaces atmospheric conditions with gas environments that lack H₂O. Fig. 3-3 shows the results of a number of writing experiments performed using dry air (Fig. 3-3(a)), helium gas (Fig. 3-3(b)), and dry nitrogen (Fig. 3-3(c)) under pressures ranging from 10⁻²-10² Torr. Nanowires were not formed under any of these conditions. To verify that the sample was not adversely affected during these experiments, the sample was subsequently exposed to air (28% relative humidity (RH)) and a nanowire was written with ~120 nS conductance (Fig. 3-3(d)). The nanowire was then erased and the AFM was evacuated to base pressure (1.8×10⁻⁵ Torr). Under vacuum conditions, it was again not possible to create conducting nanostructures.

The ability to erase nanostructures under vacuum conditions is also examined. A nanostructure is created under atmospheric conditions, and the AFM is evacuated to base pressure. After that, the conductance of such nanostructure is stabilized around 20 nS. Fig. 3-3(d) inset illustrates that erasure is still achievable under vacuum conditions.

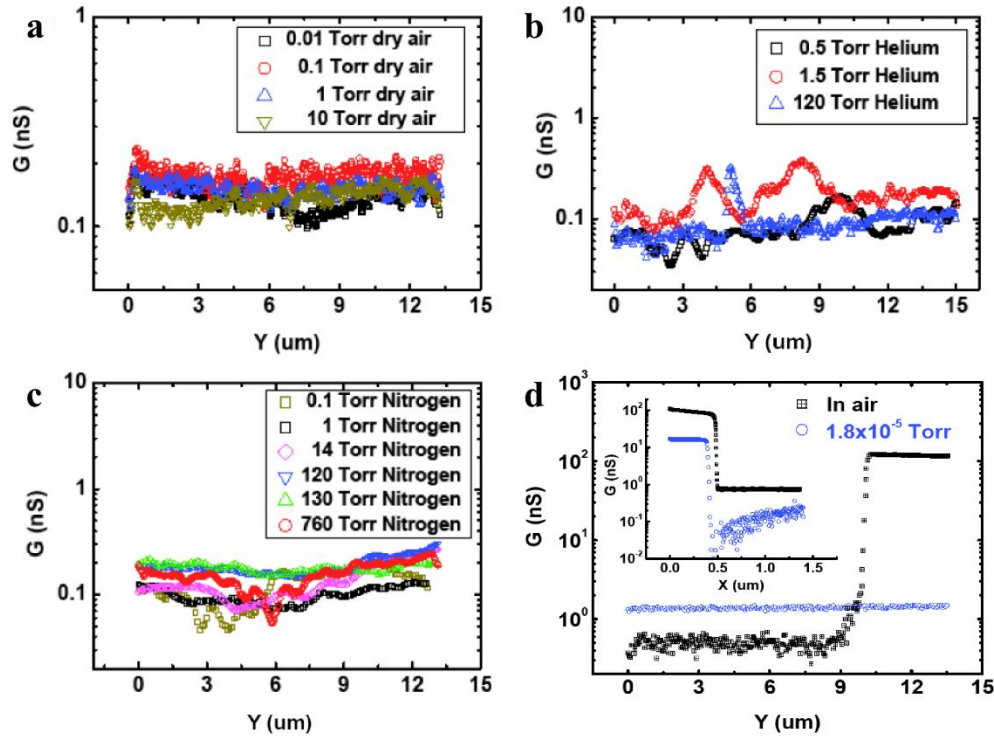


Fig. 3-3 Nanowire writing versus various atmospheric conditions. Writing a nanowire in (a) air, (b) helium, and (c) nitrogen environments. (d) Subsequent writing of nanowires under vacuum and atmospheric conditions confirms that no irreversible changes have occurred to the sample. Inset shows erasing under vacuum conditions, illustrating that the erasure process is insensitive to atmospheric conditions. In the vacuum, both the backgrounds after writing and cutting show slight increase, which is associated with the sample surface charges produced by the vacuum ion gauge.

The above experiments demonstrate that H_2O in the environment is crucial for AFM writing. To investigate how the H_2O amount affects the writing, nanostructures are created under varied pressure of air (Fig. 3-4). As the air pressure decreases, the H_2O amount in the environment

drops accordingly, making the nanowires harder to form. As shown in Fig. 3-4, the conductance of the created nanowires is suppressed tremendously when the environment pressure declines. Under 5.5×10^{-5} Torr, no conducting nanostructure can be formed.

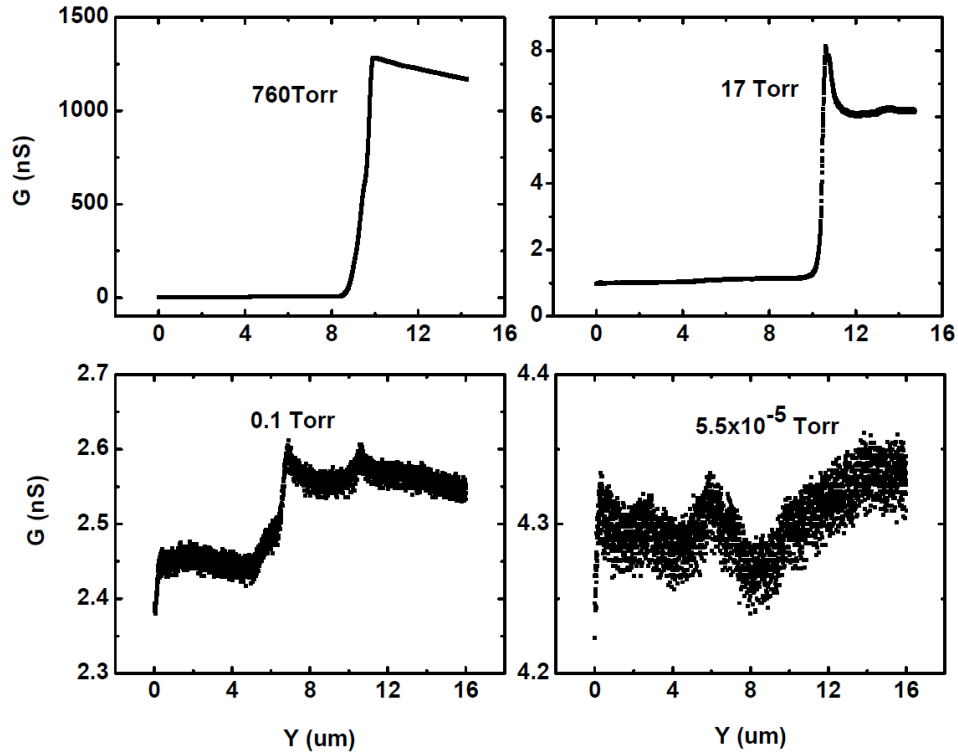


Fig. 3-4 Nanowire writing versus different air pressure.

The writing experiments are also performed under varied relative humidity (RH) environment. The sealed AFM chamber is initially filled with dry air ($P = 1$ atm, $T = 300$ K). Then water vapor is introduced to the gas chamber to increase the RH level. Under each fixed RH level, the writing experiments are performed multiple times ($n = 8$). The averaged conductance change before and after the nanowire creation is used to quantify the AFM writability:

$$\overline{\Delta G} = \frac{\sum_{i=1}^n (G_{wire} - G_{bg})}{n} \quad (3-1)$$

Here G_{wire} is the conductance after nanowire writing and G_{bg} is the background conductance before the nanowire writing.

Fig. 3-5(a) reveals the correlation between AFM writability and environment RH. As the RH value increases, the AFM created nanowires get more conducting. The results are consistent with the "water cycle" mechanism. When the RH value increases, the water meniscus is easier to form between the AFM tip and sample surface, making the AFM charge writing more effective. The surface potential on the AFM writing path can also be measured by Kelvin probe force microscopy (Fig. 3-5(b)). Higher surface potential on the writing path indicates that more H^+ adsorbates have formed by AFM writing, which explains the correlation between RH value and the writability.

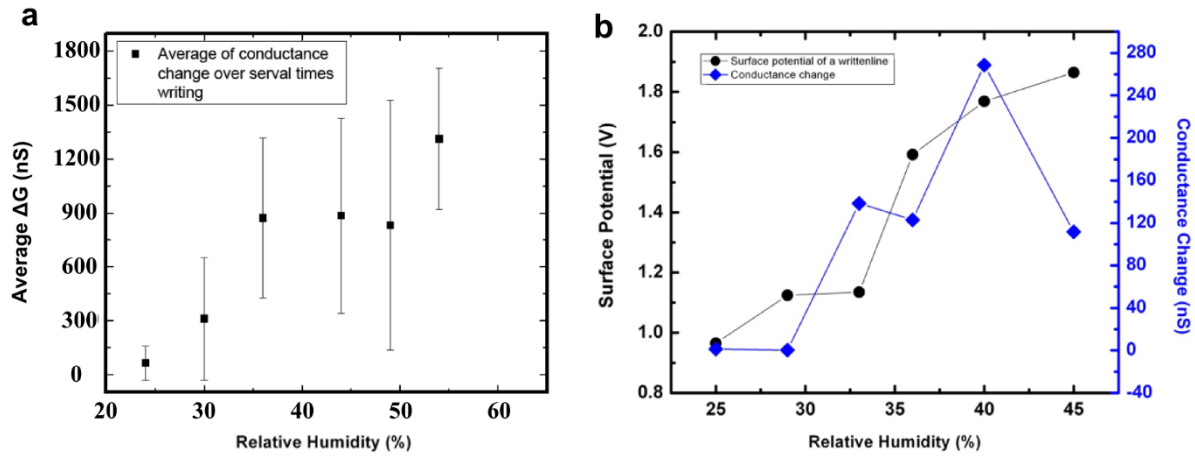


Fig. 3-5 Nanowire writing under different relative humidity. (a), nanowire writing ability under varied relative humidity level. (b), surface potential of nanowire writing with respect to the relative humidity. Notice the writing experiments in (a) and (b) are performed on two different canvases, so the conductance change scales differently.

3.5 NANO DEVICE SELF-ERASE STUDY IN CONTROLLED AMBIENT

Finally, we illustrate how the process of self-erasure depends on atmospheric conditions (Fig. 3-6). Self-erasure process of a single nanowire is observed in air and vacuum subsequently (Fig. 3-6(a)). A nanowire written at atmospheric pressure (RH=28%) exhibits a rapid initial decay. At $t=300$ s after writing the nanowire, the system is evacuated, and then reaches a pressure of 1.7×10^{-4} Torr. During this time, the nanowire conductance quickly stabilizes and reaches a constant value. At $t=1670$ s the system is vented, and the nanowire conductance resumes its decay. This experiment demonstrates that self-erasure is directly associated with atmospheric conditions, and that it can be slowed significantly or halted under modest vacuum conditions $\sim 10^{-3}$ Torr. These results are consistent with previous observations³⁸. Fig. 3-6(b) compares the self-erasure processes of a nanowire kept in air with a nanowire kept in 1 atm dry nitrogen gas. The red curve in Fig. 3-6(b) shows that a nanowire is written in air and then decays quickly in such environment (31% relative humidity air). It takes only about 2.2 hours for this nanowire to decay close to the background. For the blue curve, the nanowire is first formed in air and then the system is evacuated to 1.4×10^{-4} Torr. At $t=1900$ s, 1 atm dry nitrogen gas is introduced to the system. Compared with humid air, the self-erasure process in 1 atm dry nitrogen gas is strongly suppressed. The nanowire conductance decays by a factor of 50 or so over a 72 hour period, but remains a nanowire as evidenced by the subsequent erasure. This behavior is comparable to what was reported for vacuum conditions in Ref. 38. Therefore, these results illustrate that vacuum conditions are not required for long-term retention of nanoscale structures, although some self-erasure is evident.

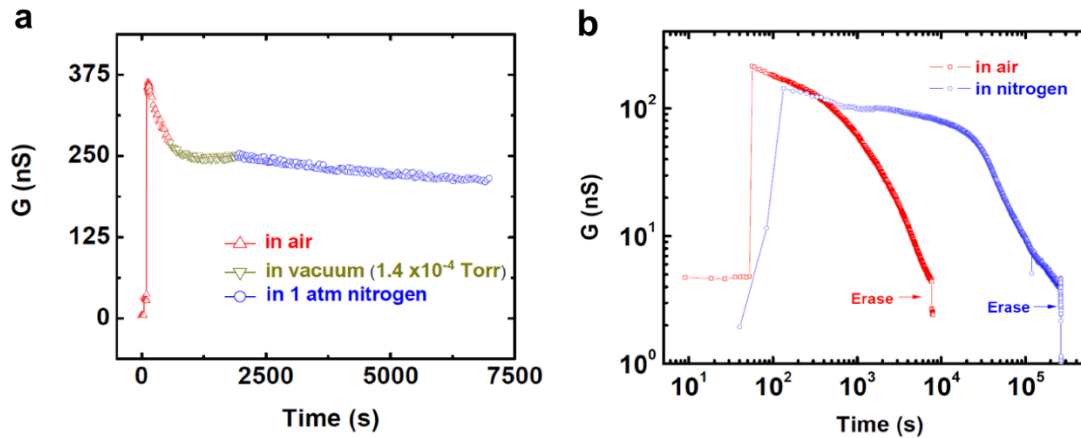


Fig. 3-6 Experiment showing effect of atmosphere on nanostructure self-erasure. (a) The self-erasure process of a single nanowire in air, vacuum and then put in 1 atm dry nitrogen environment. (b) Compare the self-erasure processes of one nanowire in air (RH=31%) and another nanowire in 1 atm dry nitrogen gas.

3.6 CONCLUSION

In conclusion, the AFM writing and erasing experiments in controlled environments provide experimental evidence for the "water cycle" mechanism. Results show that surface adsorbates play an important role in the tip induced metal-insulator transition at the LAO/STO interface. Besides, the experiments described above constrain not only models for the writing and erasing of nanostructures at $\text{LaAlO}_3/\text{SrTiO}_3$ interfaces, but also models of the interfacial conductivity itself. It is difficult to formulate a physical model that invokes only intermixing or oxygen diffusion—either at the top LaAlO_3 surface or at the interface itself—to explain the interfacial conduction. Rather, the interfacial conductance results directly from modulation doping of an otherwise insulating interface, which is stabilized by the screening of the polar discontinuity between LaAlO_3 and SrTiO_3 .

4.0 ELECTRO-MECHANICAL RESPONSE OF TOP-GATED LAO/STO

LaAlO₃/SrTiO₃ heterostructures are known to exhibit a sharp, hysteretic metal-insulator transition (MIT) with large enhanced capacitance near depletion. To understand the physical origin of this behavior, the electromechanical response of top-gated LaAlO₃/SrTiO₃ heterostructures is probed using two simultaneous measurement techniques: piezoforce microscopy (PFM) and capacitance spectroscopy. PFM measurements reveal local variations in the hysteretic response, which is directly correlated with capacitance measurements. The enhanced capacitance at the MIT is linked to charging/discharging dynamics of nanoscale conducting islands, which are revealed through PFM imaging and time-resolved capacitance and piezoresponse measurements.

4.1 INTRODUCTION

Oxide heterostructures have received increased attention due to the variety of exhibited behavior^{1,2,12,20,23,24,50} (insulating, metallic, ferroelectric, ferromagnetic and superconducting) as well as their potential for nanoelectronic device applications^{35,38-41,51}. The interface between LaAlO₃ (LAO) and TiO₂-terminated SrTiO₃ (STO) is *n*-type conducting¹ beyond a critical LAO thickness of 3 unit cells¹² and can be tuned through the metal-insulator transition (MIT) using a metallic top gate^{2,52-54}, back gate¹² or electrolyte gate¹¹. Li *et al.*⁵¹ found that near the MIT, the capacitance of gated LAO/STO heterostructures is enhanced significantly (over 40%) beyond the geometric value:

$$C_{geom} = \frac{\epsilon_{LAO} \cdot A}{d} \quad (4-1)$$

where ϵ_{LAO} is the dielectric permittivity of LAO, and A and d are the cross section and the spacing of the capacitor, respectively. Bark *et al.* have characterized gated $\text{LaAlO}_3/\text{SrTiO}_3/(\text{LaAlO}_3)_{0.3}(\text{Sr}_2\text{TaAlO}_6)_{0.7}$ structures using piezoelectric force microscopy (PFM) and observed hysteretic behavior near the MIT⁵⁵. However, the intrinsic origin of the top-gate-tuned MIT and the mechanism for capacitance enhancement as well as PFM hysteresis are still not well understood.

4.2 SAMPLE GROWTH

5 u.c. LAO/STO and 12 u.c. LAO/STO samples are grown using the PLD method by our collaborator Prof. Chang-Beom Eom's group. Details about sample growth are discussed in Section 1.2. Samples are annealed at 600 °C in 300 mbar oxygen pressure environment for several hours to reduce oxygen vacancies.

4.3 DEVICE GEOMETRY AND FABRICATION

The capacitor devices (Fig. 4-1(a)) are designed to have a geometry similar to that reported in Ref. 51. The top-gate electrodes are circular in shape, with a diameter ranging between 100 μm and 600 μm . The electrodes connecting the interface are arch-shaped with a width 20 μm and fixed

separation of 50 μm to the edge of the circular top gates. These arch-shaped electrodes surrounding the top gate are intended to provide a more isotropic electric field under applied bias.

The capacitor electrodes are deposited on the LAO/STO samples via DC-sputtering. As shown in Fig. 4-1(a), the arch-shaped electrodes are prepared by first creating 25-nm trenches via Ar-ion milling, followed by deposition of 4 nm Ti and 30 nm Au. Then a series of metallic circular top gates (4 nm Ti and 40 nm Au) are deposited on the LAO surface. The whole sample is affixed to a ceramic chip carrier using silver paint. Electrical contacts to the device are made with an ultrasonic wire bonder, using gold wires. Current-voltage (I - V) measurements are performed between arch shaped electrodes on all devices; measurements indicate (e.g., Fig. 4-1(b)) that the contacts have no Schottky barriers, similar to other reports^{11,12,20,52}.

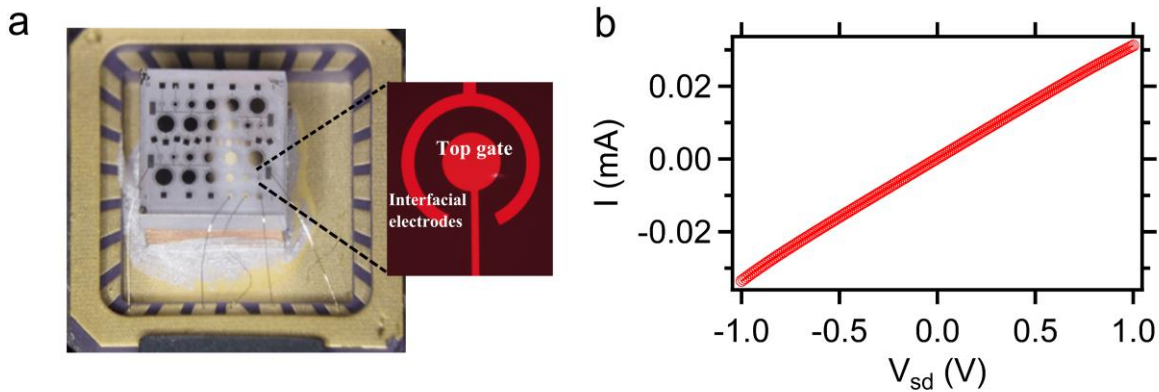


Fig. 4-1 Photograph of capacitor devices fabricated on a LAO/STO sample with leads attached. The STO substrate is square with a size 5 mm \times 5 mm. The sample is mounted on a ceramic chip carrier. (b) I - V measurement between two separated electrodes that directly contact to the interface. The linear I - V behavior shows that the electrode-interface contact is Ohmic. The conductance of the interface between these two electrodes is 3.2×10^{-5} S based on the linear fit to the IV curve, proving the interface is in the conducting phase. Results are shown for Device A.

Experimental measurements are performed on three devices, whose parameters are summarized in Table 4-1. For comparison between measurements and with results from the published literature, most of the results shown are from Device A. Similar results have been obtained for each of the three devices investigated.

	Top-gate diameter	LAO thickness	Growth condition
Device A	100 μm	12 u.c.	Grow at 780°C, partial oxygen pressure $P=10^{-5}$ mbar, annealed at 600 °C in $P(\text{O}_2)=300$ mbar for one hour
Device B	500 μm	5 u.c.	Grow at 550°C, partial oxygen pressure $P=10^{-3}$ mbar
Device C	600 μm	5 u.c.	Grow at 780°C, partial oxygen pressure $P=10^{-5}$ mbar, annealed at 600 °C in $P(\text{O}_2)=300$ mbar for one hour

Table 4-1 Device Parameters.

4.4 EXPERIMENTS AND RESULTS

4.4.1 Top-gate tuned MIT at interface

To check whether the top gate can effectively tune the carriers at the interface, a simple transport measurement of the interface is performed between two electrodes etched to the interface. The experiment setup is illustrated in Fig. 4-2(a). An ac source voltage with amplitude $V_{ac}=0.1$ V and frequency $f = 37.3$ Hz is applied to one arch-shaped electrode. The ac drain current I is measured by a lock-in amplifier through the second arch shaped electrode. The circular top gate is

connected with a dc bias V_g to tune the MIT at the interface. To avoid large current, a series resistance $R_r = 115 \text{ Mohm}$ is used in the circuit. Therefore the resistance of the interface under V_g can be obtained from $R = V_{ac} / I - R_r$, which is plotted in Fig. 4-2(b). The sharp hysteretic change in resistance of nearly two orders of magnitude coincides with the sharp changes in capacitance and indicates a MIT near $V_g=0$. Note that the resistance does not become immeasurably large in the insulating phase because the gate does not extend to the gap region between the two arch electrodes.

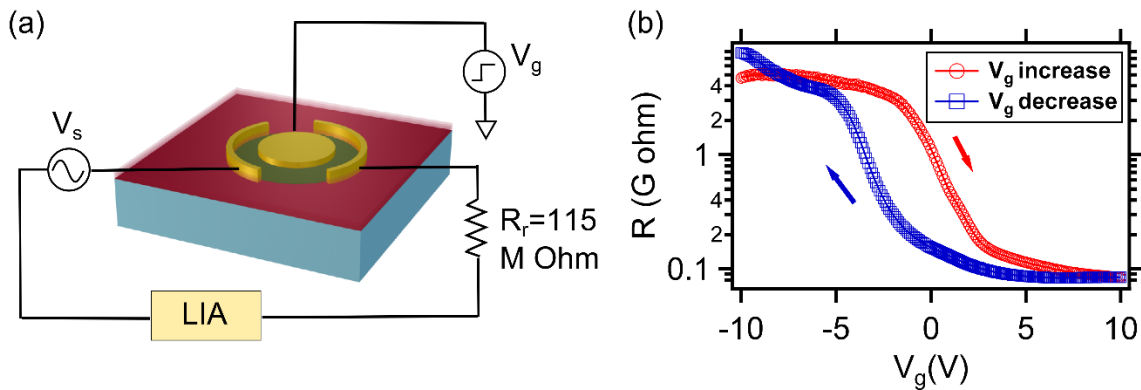


Fig. 4-2 Resistance measurements between two electrodes that contact the interface (a) Schematic diagram showing the interface resistance measurements (b) Resistance of the interface as a function of top gate bias. Results are shown for device A.

4.4.2 Capacitance and piezoresponse measurements

Simultaneous PFM and CV measurements are performed using the experimental configuration illustrated in Fig. 4-3(a). A combined dc and “dual-frequency ac signal” is applied to the interface:

$$V_{interface}(t) = -V_{dc} - V_{PFM} \cos(2\pi F_{PFM}t) - V_C \cos(2\pi F_C t) \quad (4-2)$$

The top gate is held at virtual ground in order to eliminate possible electrostatic interactions with the atomic force microscope (AFM) probe. Note that the dc component applied to the interface is $-V_{dc}$, so the equivalent top gate bias is V_{dc} . Adjusting V_{dc} tunes the LAO/STO interface between conducting and insulating phases. In order to measure the PFM response, an AFM tip is placed in contact with the top-gate electrode. The AFM tip deflection at the excitation frequency F_{PFM} is detected using a lock-in amplifier.

The capacitance as a function of gate bias $C(V_{dc})$ is measured simultaneously using a capacitance bridge similar to that described in Ref. 51. The capacitance bridge circuit is shown as the green circuit in Fig. 4-3(a). The sample is excited with an ac voltage V_C in one arm. In another arm, a synchronized ac voltage V_b with the same frequency and 180-degree phase shift is applied to a standard capacitor C_s (typically 10 pF). The signal at the balancing point is measured by a second lock-in amplifier. During the capacitance measurement, the phase and amplitude of V_C are held constant, while V_b is adjusted in a feedback loop to null the capacitance channel (out-of-phase or “Y” channel) at the balancing point. The sample capacitance is obtained from the equation:

$$C = C_s V_b / V_C \quad (4-3)$$

Both capacitance and piezoresponse measurements are performed in an enclosed AFM chamber with a small amount of scattered red light ($\lambda \geq 620$ nm), which does not have an observable effect on transport properties.

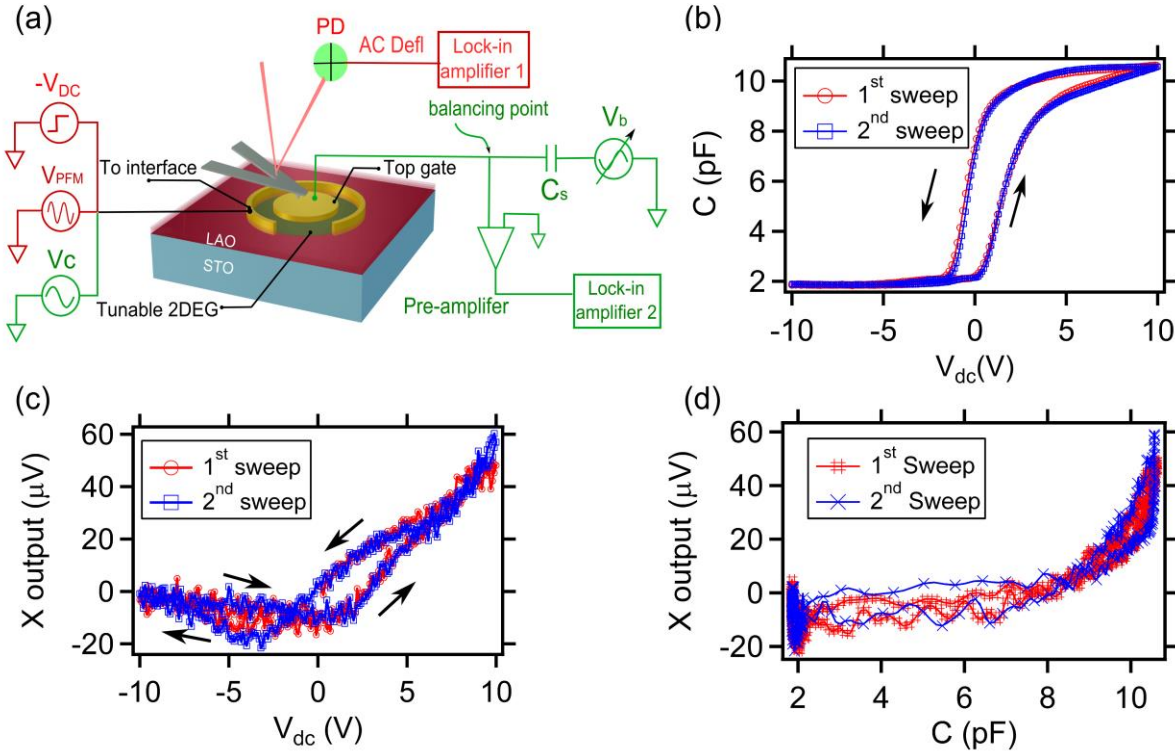


Fig. 4-3 Simultaneous PFM and capacitance measurement (a) Sample layout with circuit diagram of PFM measurement (red) is combined with a capacitance bridge (green). (b) C - V_{dc} curve taken at room temperature at $F_C=1$ kHz with the sweep rate of V_{dc} : 1/15 V/s, showing a hysteretic metal to insulator transition as V_{dc} is varied. Piezoresponse in-phase (c) signals at different values of V_{dc} with the excitation voltage given by $V_{PFM} = 20$ mV, $F_{PFM} = 293$ kHz. (d) Plot of piezoresponse versus capacitance signal shows a positive correlation between them. Results are shown for device A.

Fixed-frequency CV curves are also acquired using a commercial capacitance bridge (Andeen-Hagerling 2500A) with an ac excitation voltage given by $V_C = 10$ mV, $F_C = 1$ kHz and V_{dc} sweep at a rate $dV_{dc}/dt = 0.067$ V/s. Capacitance measurements (Fig. 4-3(b)) indicate a MIT as the gate bias V_{dc} is varied. When V_{dc} decreases ($V_{dc} < 2$ V), the capacitance signal begins to drop from its saturated value. As V_{dc} decreases further ($V_{dc} < 0$ V), the capacitance reaches a low and steady base level, indicating that the electron density underneath the circular top gate is

substantially depleted by the electric field. The depleted interface can be restored to a conducting state by increasing V_{dc} . As V_{dc} increases and becomes positive ($V_{dc} > 0$), the capacitance increases several-fold, indicating a conducting channel is restored at the interface. The capacitance variation during gate tuning is comparable to that reported in Refs. 51,52. The CV curve in Fig. 4-3(b) exhibits a stable hysteretic behavior, in agreement with previous studies^{52,54}.

Local piezoresponse measurements are also performed on the same devices (Fig. 4-3(c)). The piezoresponse signal (PRS) is measured at a fixed location on the top electrode as a function of V_{dc} . The ac excitation voltage is given by $V_{PFM} = 20$ mV and $F_{PFM} = 293$ kHz, with a voltage sweep rate $|dV_{dc}/dt| = 10$ mV/s. Far from resonance, any piezomechanical response of the sample should be either in phase or out of phase by 180° with respect to the V_{PFM} . The in-phase PFM signal contains most of the essential information of a PFM measurement,⁵⁶ while the out-of-phase PFM signal is negligibly small. Based on Fig. 4-3(c), the X-output (in-phase) piezoresponse signal is correlated with the capacitance signal: as V_{dc} decreases, the piezoresponse signal is suppressed and when V_{dc} increases, the piezoresponse signal becomes enhanced. Both hysteresis loops (Fig. 4-3(b,c)) are stable as V_{dc} is swept forward and backward for successive cycles. Parametric plotting of the X-output piezoresponse versus capacitance (Fig. 4-3(d)), shows that the hysteresis near $V_{dc} = 0$ V is highly correlated; however, there are significant deviations at both low and high values of the capacitance. Although the piezoresponse measurements are performed at a single location, this behavior is typical of measurements performed at other locations (Fig. 4-4).

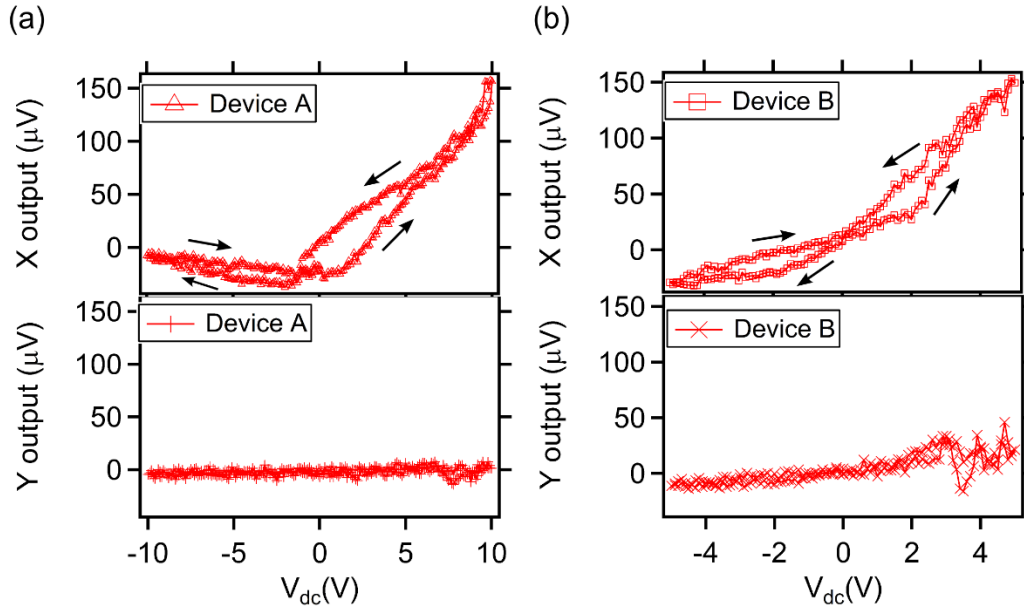


Fig. 4-4 Piezoresponse under electric field. (a) Piezoresponse signals on device A at a different tip location with the excitation voltage given by $V_{PFM}=50$ mV, $F_{PFM}=293$ kHz under varied V_{dc} . (b) Piezoresponse measurements on Device B with the excitation voltage given by $V_{PFM}=50$ mV, $F_{PFM}=301$ kHz. X, Y output represent the in-phase and 90 degrees out-of-phase piezoresponse signal respectively.

4.4.3 Quantitative PFM analysis

A non-zero piezoresponse implies that there is a lattice distortion as a result of the applied voltage. Therefore a quantitative analysis of the PFM⁵⁶⁻⁵⁹ measurement is performed (See Section 2.2.5 for a detailed discussion). A series of piezoresponse spectra (Fig. 4-5(a)) is acquired with $V_{PFM} = 20$ mV and F_{PFM} from 285 kHz to 305 kHz under a sequence of bias conditions $V_{dc} = 0$ V \rightarrow -10 V \rightarrow +10 V \rightarrow 0 V. The open circles in the intensity graph highlight the contact resonant frequency trajectory as V_{dc} is modulated. For better illustration, the contact resonant frequency is plotted with respect to V_{dc} in Fig. 4-5(b). The prominent resonant frequency change

as well as the hysteretic behavior suggests a change in the height as well as the restoring force of the LaAlO_3 surface as applied V_{dc} varies. Fig. 4-5(b) shares the same color legend as (a), which represents the PFM amplitude at each resonant frequency.

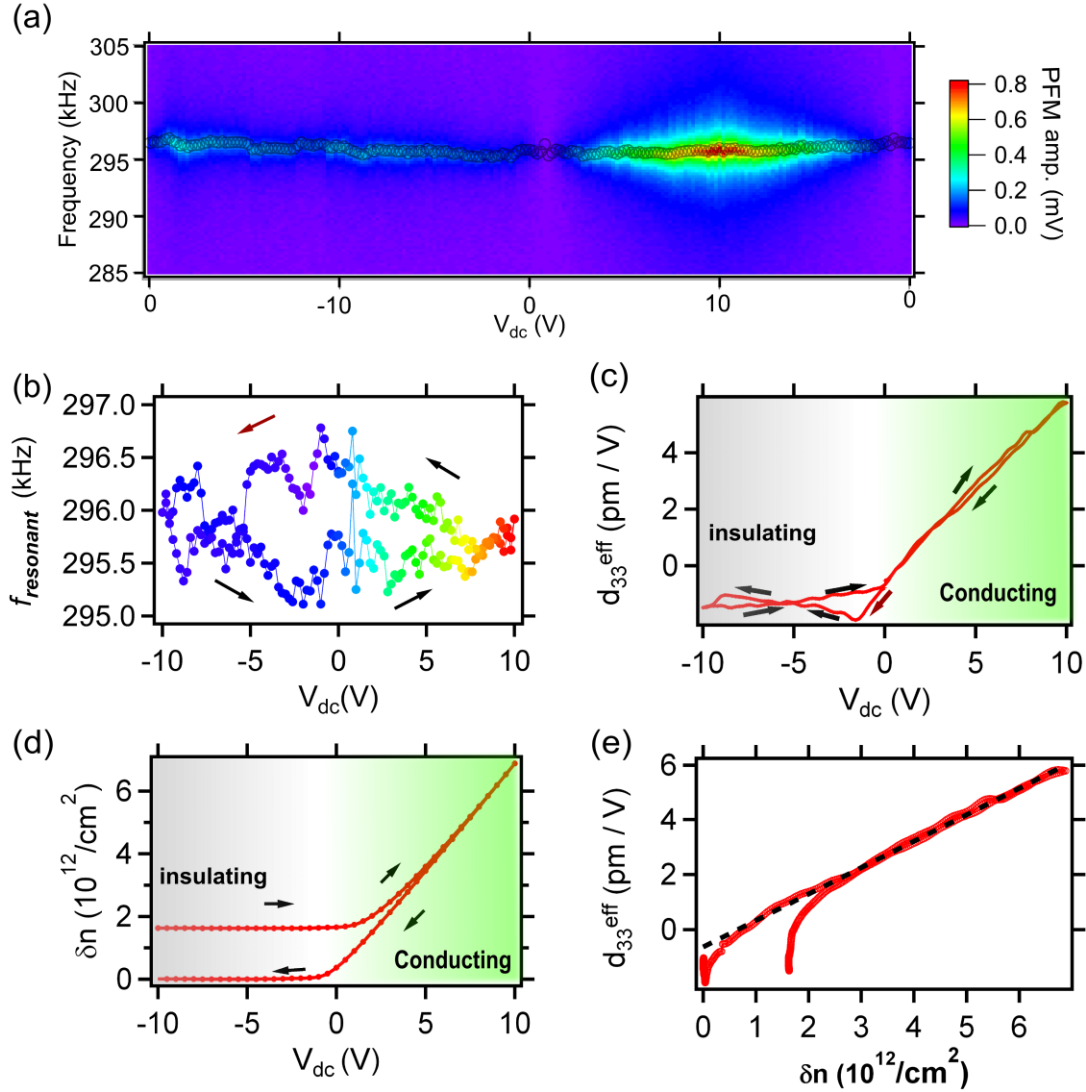


Fig. 4-5 Quantitative analysis of PFM spectra on device A. (a) Piezoresponse within a frequency band from 285 kHz to 305 kHz under various dc bias conditions (V_{dc} : 0 V \rightarrow -10 V \rightarrow 10 V \rightarrow 0 V, step 0.2 V). The open circles in this intensity graph represent the contact resonant frequency peak under each dc bias. (b) Contact resonant frequency is extracted from (a) and plotted as a function of V_{dc} . The color of each data point represents the piezoresponse amplitude at each resonant frequency. (a) and (b) share the same color scale legend. (c) $d_{33}^{\text{eff}}(V_{dc})$ is acquired from the

piezoresponse spectra in (a) using SHO model fitting. (d) Carrier density change: δn at the interface as a function of

V_{dc} . δn is calculated from equation: $\delta n = n(V_{dc}) - n(-10V) = \frac{\int_{-10V}^{V_{dc}} (C(V) - C(-10V))dV}{e \times \pi r^2}$ with $r = 50 \mu\text{m}$. (e) Plot of

$d_{33}^{eff}(V_{dc})$ with respect to δn .

The bias-dependence of the effective piezoelectric strain tensor element $d_{33}^{eff}(V_{dc})$ (Fig. 4-5(c)) can be used to quantify the lattice distortion. This coefficient is obtained by fitting the piezoresponse spectra (Fig. 4-5(a)) to a simple harmonic oscillator (SHO) model⁶⁰ (details are described in Section. 2.2.5) as a function of V_{dc} . The 2D carrier density change at the interface (Fig. 4-5(d)) is calculated as follows:

$$\delta n = n(V_{dc}) - n(-10V) = (1/eA) \int_{-10V}^{V_{dc}} (C(V) - C(-10V))dV \quad (4-4)$$

By plotting parametrically $d_{33}^{eff}(V_{dc})$ versus δn , (Fig. 4-5(e)), a linear relationship between the strain tensor and carrier density change is revealed:

$$d_{33}^{eff} = d_{33}' \cdot \delta n + d_{33}'' \quad (4-5)$$

where $d_{33}' = 0.96 (10^{-12} \text{pm cm}^2/\text{V})$ and $d_{33}'' = -0.63 \text{pm/V}$. In this manner, the effective piezoelectric strain tensor can be said to provide a direct measure of local carrier density.

4.4.4 Surface displacement calculation

The net vertical surface displacement as a function of V_{dc} at the location of the AFM tip can be obtained by integrating $d_{33}^{eff}(V_{dc})$ with respect to the applied voltage V_{dc} using Eq. (2-4).

The calculated surface displacement shows the lattice distortion under dc bias, which is due to

both LAO polarization and the interface distortion. The displacement in both sides of the MIT (Fig. 4-6(a)) are qualitatively different: for negative V_{dc} , the displacement is linear, which means there is a constant piezoresponse, plausibly from LAO polarization; for positive V_{dc} , the displacement is quadratic, which implies that the distortion is associate with charge accumulation at the interface. The contribution from the LAO layer can be estimated by a linear fit in the insulating regime (Fig. 4-6(a)). The interfacial distortion is obtained by subtracting the LAO contribution (Fig. 4-6(b)). The calculated dilation $\Delta d'(V_{dc} = 5V) - \Delta d'(V_{dc} = -5V) = 0.11 \text{ \AA}$ is consistent with previous experimental⁶¹ and theoretical^{45,62,63} reports.

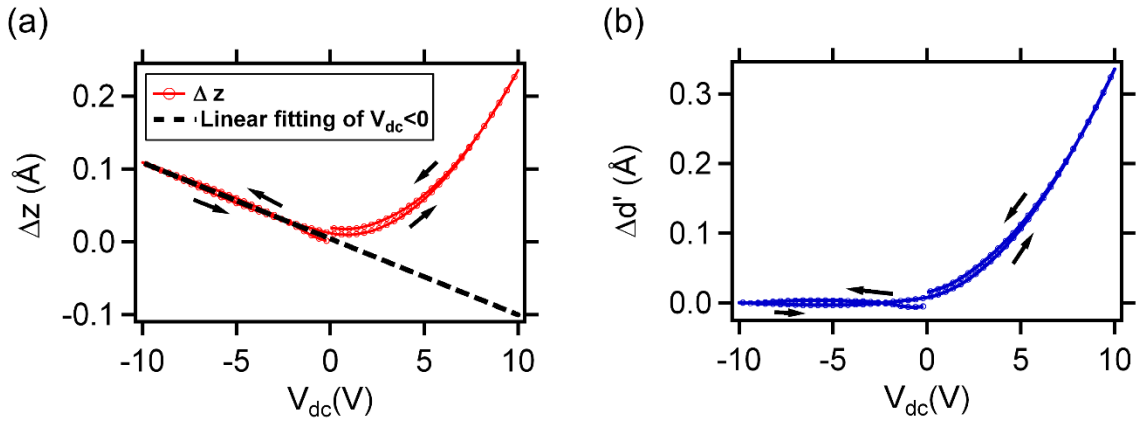


Fig. 4-6 Surface displacement calculation. (a) Surface displacement calculation based on $d_{33}^{eff}(V_{dc})$ in Fig. 4-5(c) from equation $\Delta z(V_{dc}) = \int_0^{V_{dc}} d_{33}^{eff}(V) dV$. For $V_{dc} < 0$ region, the displacement is linear with respect to the V_{dc} . The linear response is fitted as the black dashed line. (b) $\Delta d'$ as a function of V_{dc} acquired from (a) subtracting the linear fitting, which we interpret as interface distortion.

4.4.5 Simultaneous capacitance and piezoresponse measurements

To better understand the relationship between the capacitance and piezoresponse signals, the two signals are measured simultaneously with V_{dc} abruptly changing into or out of the MIT region (Fig. 4-7). The piezoresponse is integrated over a frequency band centered on the contact resonance frequency (~ 270 kHz), while the capacitance is monitored in parallel according to the arrangement in Fig. 4-3(a). Strong correlations exist between the PFM and capacitance signals for each of the voltage ranges explored, which led further support to the thesis that PFM can be employed as a sensitive local probe of the gate-tuned carrier density.

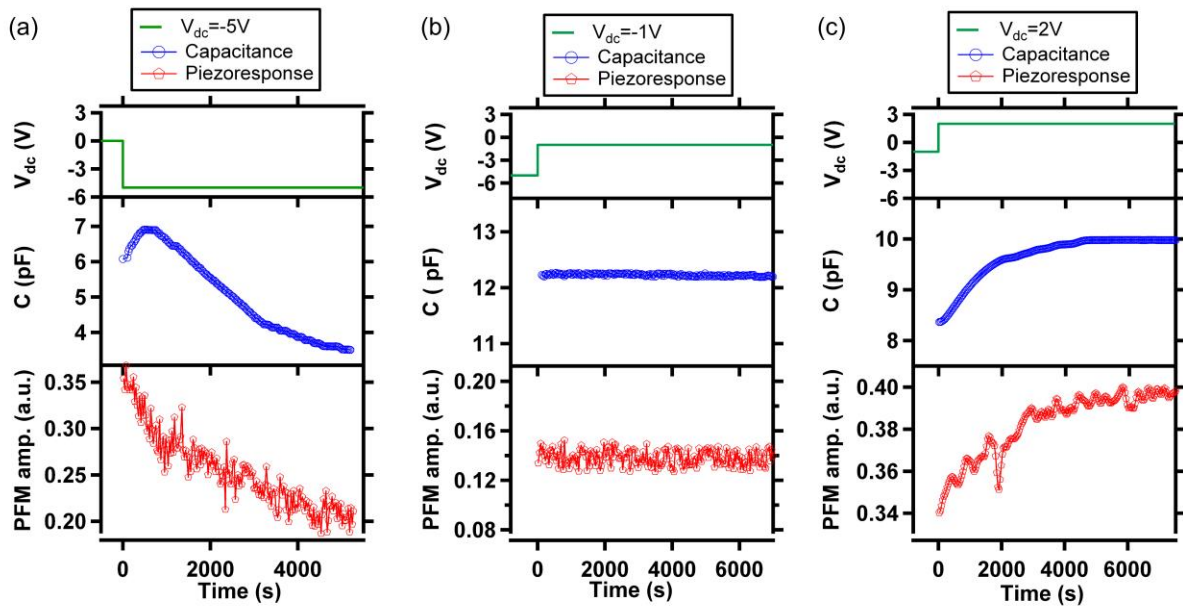


Fig. 4-7 Simultaneous time-dependent PFM and capacitance measurements at fixed top gate biases. (a) $V_{dc} = -5$ V. (b) $V_{dc} = -1$ V. (c) $V_{dc} = 2$ V. Top graph shows the V_{dc} bias history. V_C and V_b are applied at the capacitance bridge frequency 14 Hz. PFM response is measured at a frequency band centered on the contact resonant frequency between 290 kHz to 310 kHz with 200 Hz steps. To avoid the influence of resonance frequency changes, the PFM response is integrated in the frequency band from 290 kHz to 310 kHz. Results are shown for device B.

4.4.6 Time-resolved PFM measurements and frequency dependence of capacitance enhancement

A large capacitance enhancement on LAO/STO near the MIT was first reported by Li *et al.*⁵¹. A strong frequency dependence was observed, with enhanced capacitance values observed for frequencies below ~50-100 Hz. Fig. 4-8(a) shows *CV* measurements performed for Device A at frequencies ranging from 7 Hz – 100 Hz. An ac excitation voltage $V_C=20$ mV is employed, and V_{dc} is varied from 1 V to -6 V in steps of 0.1 V. In Fig. 4-8(a), when the device is depleted of electrons (V_{dc} decreasing from 0 V to -2 V), a capacitance upturn is observed. At its peak, the capacitance is enhanced significantly beyond the geometric limit, in accordance with prior reports⁵¹. The capacitance enhancement also shows a frequency dependence (Fig. 4-8(a)) that is in excellent agreement with Li *et al.* (Ref. 51) At excitation frequencies above $F_c\sim 70$ Hz, the capacitance enhancement decays, and vanishes completely by $F_c=1$ kHz. This enhancement is not present for positive gate sweeps (Fig. 4-8(b)); such sweeps were not reported in Ref. 51.

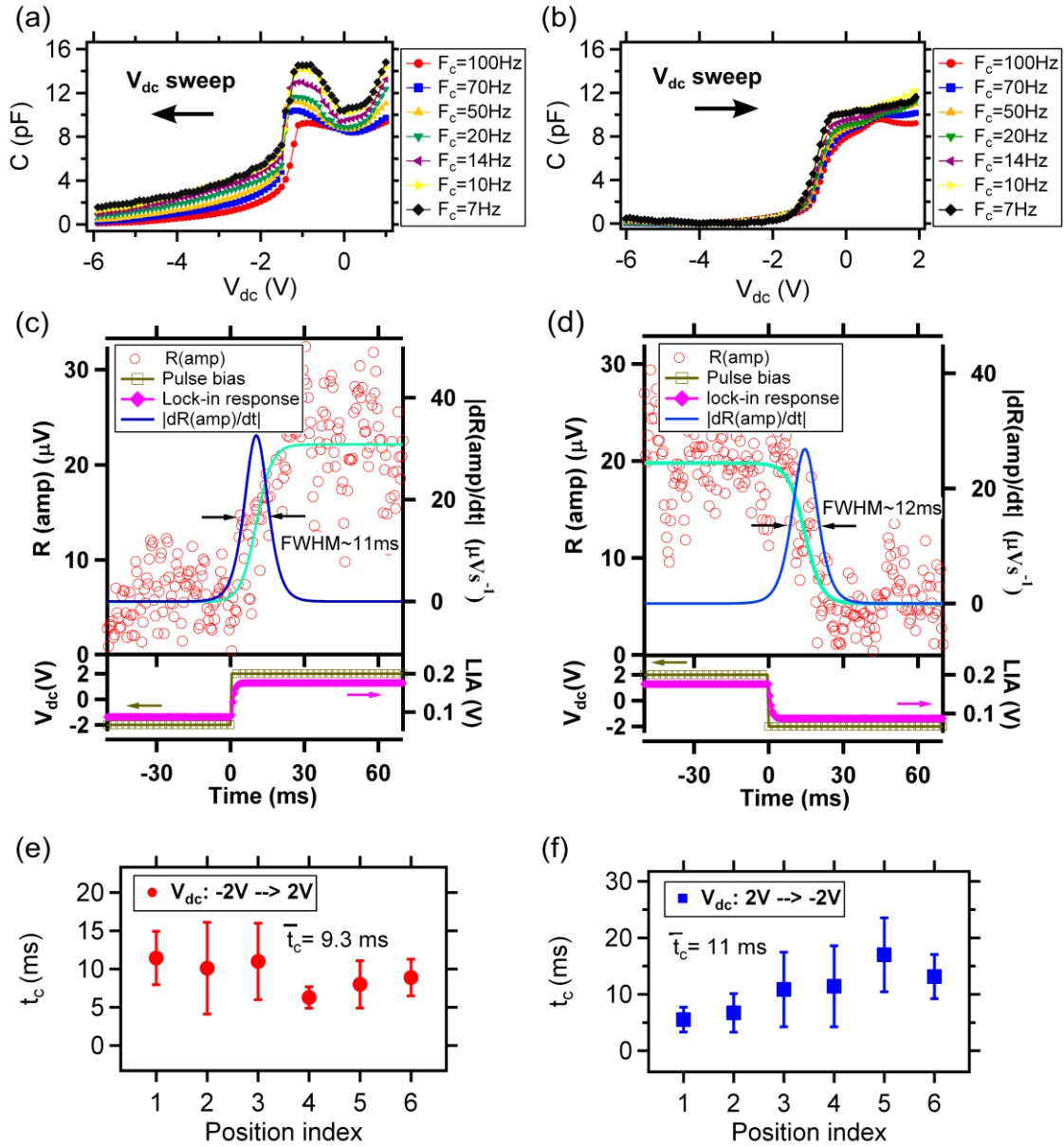


Fig. 4-8 Capacitance enhancement and time resolved PFM analysis. Capacitance is measured as dc bias decreases (a) or increases (b). Curves are taken at room temperature with frequency $F_C = 7$ Hz to 100 Hz. (c) Time resolved piezoresponse during an applied step-function dc bias. (d) Piezoresponse as the V_{dc} bias is removed. Red circles are data and the green line shows a fit to an empirical expression Eq. Front panel of the AFM lithography program. The response time t_c is defined by FWHM of $dR(amp)/dt$ and corresponds to frequency $f_c=1/t_c$. The diamond curves show that the lock-in amplifier equipment response time is around 1 ms ($TC=1$ ms, rolloff 6 dB/oct) from fitting. (e), (f) are time resolved piezoresponse analyses at different locations. At each location, measurements are repeated several times

and the mean \bar{t}_c and standard deviation σ are calculated. The mean value for all \bar{t}_c (local) is also noted, as \bar{t}_c in the graph. Data shown is from device A.

To gain insight into this phenomenon, time-resolved piezoresponse measurements are applied for different tip locations on the devices. The experimental setup is illustrated in Fig. 4-3(a): an ac excitation voltage $V_{\text{PFM}}=20$ mV at the resonant frequency together with a step-function pulse (blue curve, V_{dc} switches between -2 V and +2 V) are applied to the LAO/STO interface. Time-resolved PFM measurements are performed using a lock-in amplifier with time constant $T_c = 1$ ms and frequency rolloff 6 dB/oct. As a reference, the lock-in amplifier response to a sudden amplitude-modulated test wave is shown (bright pink diamond curve in Fig. 4-3(c-d)), confirming that the bandwidth of the instrumentation exceeds that of the sample response by approximately one order of magnitude.

Fig. 4-8(c) and (d) show the time-resolved piezoresponse amplitude (note as $R(\text{amp})$) as a $V_{dc}=\pm 2$ V pulse is turned on and off for Device A. Fitting the piezoresponse to an empirical expression

$$R(\text{amp}) = a_1 \cdot \tanh((t - t_0)/t_1) + a_2 \quad (4-6)$$

yields a characteristic response time $t_c = 1.76 t_1$, defined as the full width at half maximum (FWHM) of $dR(\text{amp})/dt$, and corresponding frequency $1/t_c$. The response times in Fig. 4-8(c) and Fig. 4-8(d) are 11 ms and 12 ms respectively, corresponding to $1/t_c = 90$ Hz and 84 Hz, respectively. These frequencies agree well with the observed frequency response in the CV experiments.

The time-resolved piezoresponse measurements are reproducible at different locations on the device. At each location, measurements are performed 5-10 times and the mean value is computed as well as the standard deviation. Fig. 4-8(e) and Fig. 4-8(f) show statistical results of measured response time on device A. The mean time for all these investigated locations is 9.3 ms in Fig. 4-8(e) and 11 ms in Fig. 4-8(f), which corresponds to ~108 Hz and 91 Hz respectively. Such results also agree with the frequency dependence of capacitance enhancement. Similar results are observed for the other devices.

4.4.7 Interfacial carrier density distribution mapping by spatially resolved PFM imaging

PFM has previously been reported to be highly correlated with the MIT⁵⁵. Considering the observed linear relation between piezoresponse and carrier density (Fig. 4-5(e)), PFM imaging can serve as a powerful local probe of interfacial charge density. Such spatially resolved PFM imaging can therefore provide insight into possible origins of hysteretic behavior and capacitance enhancement near the depletion region, which has not been reported before.

PFM imaging introduces some technical challenges. For example, if the AFM tip picks up a small particle or otherwise changes as it is scanning, the resonant frequency can shift. To minimize the influence of small frequency shifts during PFM imaging, a dual-ac resonance tracking (DART)⁶⁴ technique is used, with the parameters $f_{ac1} = 284.6$ kHz, $f_{ac2} = 287.6$ kHz and $V_{ac1} = V_{ac2} = 20$ mV.

Fig. 4-9 shows dual-frequency PFM amplitude images over a 500 nm × 500 nm area on the top-gate electrode of device A. Significant spatial variations in the critical voltage for strong enhancement of PFM on 25-50 nm scales are observed (Fig. 4-9(b)-(f)), while a superimposed

inhomogeneity of several hundreds of nanometers is found on Device C (Fig. 4-10). Fig. 4-9(a) shows the topographic image and (b-f) are PFM images taken under decreasing bias $V_{dc} = 3\text{ V}, 2\text{ V}, 1\text{ V}, 0\text{ V}, -2\text{ V}$, which traverse the MIT transition (Fig. 4-9(b)). Notice that for (b-f), each image is subtracted the mean value (from (b) to (f) is 4.24 a.u., 3.10 a.u., 1.91 a.u., 0.82 a.u., 0.35 a.u., respectively) to show a better PFM contrast. When $V_{dc} \geq 2\text{ V}$, the carrier density at the interface is relatively high. The PFM response is strong everywhere except for a few isolated regions. Also the inhomogeneity of the PFM signal is clearly shown in Fig. 4-9(b-c). In the images shown, green areas correspond to high PFM response (relatively higher carrier density), while red regions have lower PFM response (relatively lower carrier density). As V_{dc} decreases in the range $2\text{ V} > V_{dc} > -2\text{ V}$, the capacitance signal drops rapidly, indicating the depletion of mobile carriers at the interface. Within this range, the PFM signal becomes suppressed in some areas and PFM contrast is reduced (Fig. 4-9(d)-(e)), indicating large local variations in carrier density. When $V_{dc} \leq -2\text{ V}$, the PFM signal becomes small with greatly suppressed spatial variations (Fig. 4-9(f)), corresponding to the interface globally switching to an insulating state. The evolution of PFM contrast from Fig. 4-9(b) to (f) shows direct evidence of ~30-50 nm-diameter conducting islands at the interface.

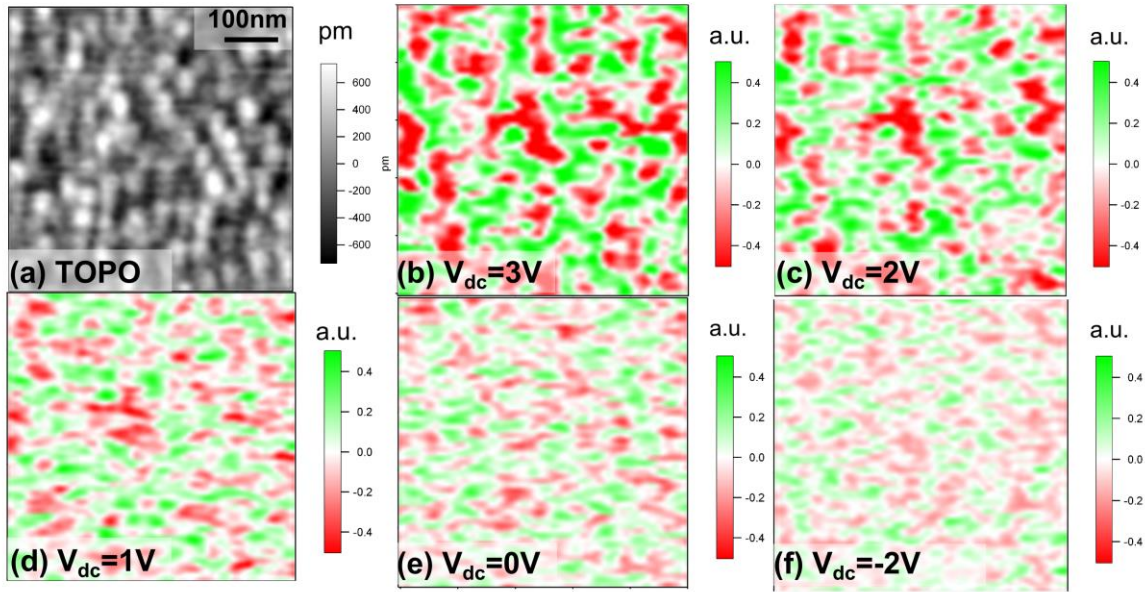


Fig. 4-9 Spatially-resolved dual frequency PFM images show inhomogeneity at the interface. The height image (a) and corresponding PFM images (b-f) are shown at bias values $V_{dc} =$ (b) 3V, (c) 2V, (d) 1V, (e) 0V (f) -2V with the mean value 4.24 a.u., 3.10 a.u., 1.91 a.u., 0.82 a.u., 0.35 a.u. subtracted. Scan size 500 nm \times 500 nm; results shown are from device A.

The observed fine spatial structures in PFM images are stable and reproducible, evidenced by the continuous scanning over the same area (Fig. 4-10) and scanning with fast and slow-scan axes reversed. Fig. 4-10 shows two sets of continuous PFM scanning under $V_{dc} = 3$ V ((a,b)) and $V_{dc} = 1.5$ V ((c,d)) separated by a time interval of 22 minutes. The fine spatial structure in PFM images at the same V_{dc} is reproducible, indicating the stability of conducting and insulating domains at the interface.

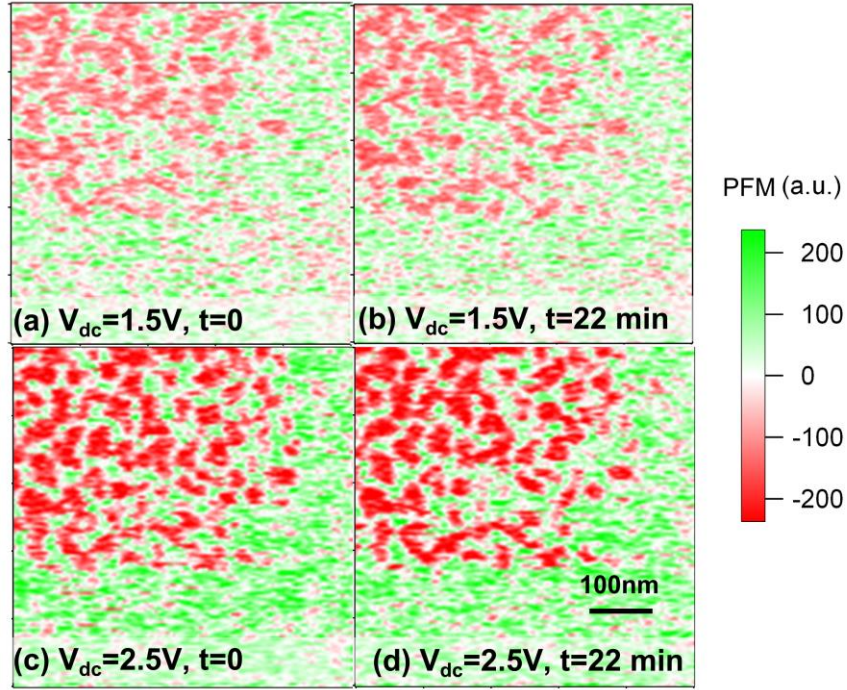


Fig. 4-10 Spatially resolved dual frequency PFM images (500nm×500nm) on device C. Images are taken under V_{dc} : 1.5 V (a),(b) and 2.5 V (c),(d) at different times after the bias application. The average PFM signals for (a) 0.22 a.u., (b) 0.23 a.u., (c) 0.33 a.u., (d) 0.34 a.u. are already subtracted from each image for the purpose of showing a better contrast.

4.4.8 RMS and histogram analysis of bias dependent inhomogeneity at the interface

The PFM images reveal inhomogeneity of the carrier density at the interface. To check the inhomogeneity of the piezoresponse signal over the scanned areas with respect to different V_{dc} , a normalized root-mean-square (RMS) analysis is applied to PFM images (500×500 nm²) taken under various values V_{dc} on different devices. This analysis is repeated at several locations using different sets of PFM images. Before calculating the RMS value, each PFM image is averaged

over $25 \text{ nm} \times 25 \text{ nm}$ area to reduce contributions due to intrinsic noise. The RMS PFM signal is then calculated as follows:

$$\text{Normalized RMS} = \frac{\text{RMS}(V_{dc})}{x(V_I)} = \frac{\sqrt{\frac{1}{n} \sum_{i=0}^{n-1} |x_i(V_{dc})|^2}}{\frac{1}{n} \sum_{i=0}^{n-1} x_i(V_I)} \quad (4-7)$$

Normalization is taken with respect to the average signal in the insulating region ($V_I = -5\text{V}$). With the resolution of 128×128 for all PFM images, $n = 128 \times 128$ in the formula. The normalized RMS signals for devices A, B and C are illustrated in Fig. 4-11, respectively. All of the normalized RMS curves show similar behavior: the normalized RMS signals are enhanced as V_{dc} increases in the conducting region, indicating large inhomogeneity at the interface.

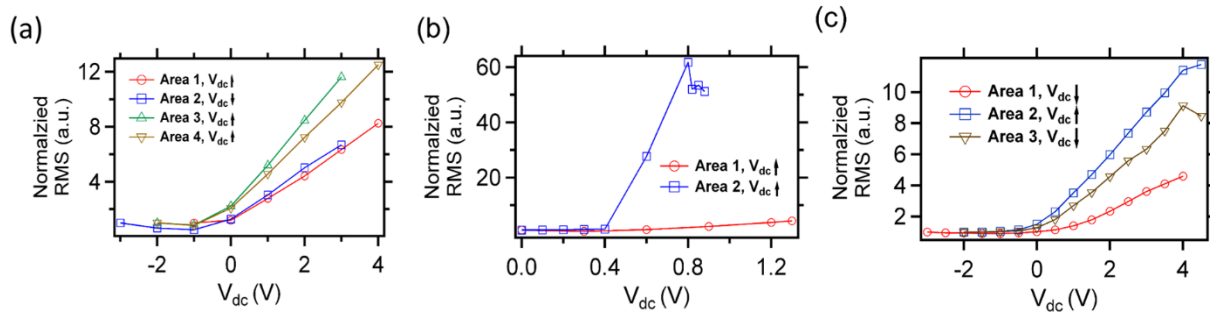


Fig. 4-11 Normalized RMS analysis for PFM images acquired over different locations on Device A (a), B (b) and C (c), respectively. The normalized RMS value is associated with the inhomogeneity at the interface.

4.5 CONCLUSION AND DISCUSSION

The combined PFM and capacitance measurements performed on top-gated LAO/STO devices reveal strong correlations between structural, capacitive, and metallic properties. Bark

*et al.*⁵⁵ proposed that the electrically-induced oxygen vacancy migration in the LAO layer is responsible for the hysteretic PFM response. The PFM is performed at relatively high frequencies (around 290 kHz), whereas oxygen vacancies have too small of a mobility $\sim 10^{-13}$ cm²/Vs,⁶⁵ for the piezoresponse signal to be attributed to oxygen vacancy motion. Furthermore, it is observed that in air the piezoresponse hysteresis exists even under a complete lack of local driving, but vanishes in vacuum with the same experiment setup⁶⁶, which cannot be explained by the oxygen vacancy mechanism. Finally, the samples described here are annealed in partial oxygen pressure ambient at 600 °C, conditions under which the majority of oxygen vacancies are expected to be removed in the STO substrate¹⁰.

The electromechanical response can be attributed to Jahn-Teller effects^{67,68}, which proposes that the electron accumulation on the Ti-3d band at the LAO/STO interface can induce oxygen octahedral distortion. There is evidence from both transmission electron microscopy⁶¹ and X-ray⁶⁹ measurements that when LAO is grown on (001) STO, distortions in TiO₆ octahedra happen at the interface. Such lattice distortions at the interface result in a biaxial strain and a strain gradient that can induce ferroelectric⁷⁰ and flexoelectric⁷¹ polarization in STO near the interface. Theoretical calculations^{45,62,63} of LAO/STO system also reveal carrier-mediated distortions at the interface. The calculated dilation at the interface of about $\delta z = 0.15$ Å is consistent with what is reported here.

The Jahn-Teller mechanism also helps to explain the strong correlation between capacitance signal and piezoresponse (Fig. 4-5, Fig. 4-7). In the insulating phase (large negative V_{dc}), the capacitance is small and approximately bias-independent. The piezoresponse is similarly small and independent of V_{dc} . As V_{dc} increases, electrons will eventually be introduced to the interface, leading to an enhancement of capacitance signal. These electrons can occupy/evacuate

the Ti-3d band at the interface under V_{PFM} modulation, which gives rise to a stronger oxygen octahedra distortion as well as an enhanced piezoresponse signal that scales with the local carrier density.

The spatially resolved PFM images show large local variations in PFM contrast, suggesting that the MIT is strongly inhomogeneous. Previous Kelvin probe force microscopy studies^{72,73} also show an inhomogeneous distribution of the surface potential in LAO/STO samples, which suggests an inhomogeneous carrier density at the interface. The frequency response of the PFM and CV measurements is marked by charging-discharging dynamics of nanoscale islands observed in PFM images. At the MIT, the characteristic frequency response compares well to the conductance measurement for a randomly mixed conductor-insulator system near the percolation threshold⁷⁴. The observed frequency dependence of capacitance enhancement may be understood in terms of an intrinsic time scale for island charging-discharging dynamics.

To summarize, capacitance characterization and PFM are combined to help understand the origin of observed piezoresponse signal, and the mechanism for hysteretic behavior in CV and PFM measurements. The frequency dependence of the capacitance enhancement in LAO/STO matches that of local PFM measurements and is otherwise highly correlated. A quantitative analysis of the piezoresponse indicates there is a structural distortion associated with the gate-tuned MIT at the LAO/STO interface. The carrier-mediated structural distortion is understood as a Jahn-Teller effect, with a magnitude that agrees with theoretical calculations. Spatially resolved PFM provides a direct visualization of the island charging/discharging process at the interface under gate tuning. Our experiments provide a fuller understanding of the interplay between electrons and lattice degrees of freedom, and may help to find more potential applications of oxide-based nanoelectronics.

5.0 ELECTRONICALLY CONTROLLED FERROMAGNETISM ON TOP-GATED LAO/STO AT ROOM TEMPERATURE

Reports of emergent conductivity, superconductivity, and magnetism have helped to fuel intense interest in the rich physics and technological potential of complex-oxide interfaces, such as LAO/STO heterostructure. This chapter demonstrates the efforts to search for room-temperature magnetism in the well-studied LAO/STO system using magnetic force microscopy and magnetoelectric force microscopy techniques. Using electrical top-gating to control the electron density at the oxide interface, we directly observe the emergence of an in-plane ferromagnetic phase as electrons are depleted from the interface. Itinerant electrons that are reintroduced into the interface align antiferromagnetically with the magnetization, at first screening and then destabilizing it as the conductive regime is approached. Repeated cycling of the gate voltage results in new, uncorrelated magnetic patterns. This newfound control over emergent magnetism at the interface between two non-magnetic oxides portends a number of important technological applications.

5.1 INTRODUCTION

Vigorous efforts have been made to integrate magnetism with semiconductors⁷⁵⁻⁷⁷. Ideally, a ferromagnetic semiconductor would possess full electrical control over its magnetic properties combined with strong coupling to the spin of mobile charge carriers. Efforts to identify suitable materials have focused on diluted magnetic semiconductors (DMS) such as (Ga,Mn)As⁷⁸, diluted

magnetic oxides (DMOs)⁷⁷, and magnetoelectric materials such as chromia⁷⁹. Strong electronic correlations⁸⁰ can also induce charge-ordered phases, produce electronic phase separation, and stabilize various types of magnetic order.

The two-dimensional electron liquid (2DEL) that forms at the interface between the two insulating non-magnetic oxides LaAlO₃ (LAO) and SrTiO₃ (STO)¹ has drawn widespread attention due to its possession of a remarkable variety of emergent behavior including superconductivity²⁰, strong Rashba-like spin-orbit coupling^{18,19}, and ferromagnetism²³⁻²⁷. The first signatures of magnetism at the LAO/STO interface were reported in magnetotransport measurements by Brinkman *et al.*²³ DC scanning quantum interference device (SQUID) magnetometry measurements by Ariando *et al.*²⁴ revealed ferromagnetic hysteresis extending to room temperature. Torque magnetometry measurements by Li *et al.*²⁶ showed evidence for in-plane magnetism with a high moment density ($\sim 0.3 \mu_B/\text{unit cell}$). Scanning SQUID microscopy by Bert *et al.*²⁵ revealed inhomogeneous micron-scale magnetic “patches”. X-ray circular dichroism measurements by Lee *et al.* indicate that the ferromagnetism is intrinsic and linked to d_{xy} orbitals in the Ti t_{2g} band²⁷.

Despite this variety of evidence, the existence and nature of magnetism in LAO/STO heterostructures has remained controversial. Neutron reflectometry measurements by Fitzsimmons *et al.* on LAO/STO superlattices⁸¹ found no magnetic signatures; their measurements established a bulk upper limit thirty times lower than what was reported by Li *et al.*²⁶ Salman *et al.* reported relatively small moments from LAO/STO superlattices ($\sim 2 \times 10^{-3} \mu_B/\text{unit cell}$) using β -detected nuclear magnetic resonance⁸².

Our search for magnetism at the LAO/STO interface is guided by the fact that most of the interesting behavior observed at the LAO/STO interface—superconductivity, spin-orbit

coupling, anisotropic magnetoresistance, and anomalous Hall behavior—depends strongly on carrier density^{21,60,83,84}. The electron density at the interface can be controlled using a number of techniques including back-gating¹², top-gating⁵², polar adsorbates⁸⁵, or via nanoscale control using conductive atomic force microscopy (AFM) lithography³⁵.

Here we investigate magnetism at the LAO/STO interface using magnetic force microscopy (MFM)⁸⁶. By using top-gated LAO/STO heterostructures we are able to search for magnetism as a function of mobile carrier density at the oxide interface. We directly observe the emergence of an in-plane ferromagnetic phase as electrons are depleted from the interface. Reintroducing the itinerant electrons, which align antiferromagnetically with the magnetization, into the interface at first screens and then destabilizes the magnetization as the conductive regime is approached.

5.2 SAMPLE GROWTH

LAO/STO heterostructures are fabricated by depositing 12 unit cell (u.c.) LAO films on TiO₂-terminated (001) STO substrates using pulsed laser deposition with in situ high-pressure reflection high energy electron diffraction (RHEED). Two different growth conditions are used for the substrate growth temperature T and chamber background partial oxygen pressure $P(\text{O}_2)$: (1) $T=550$ °C and $P(\text{O}_2)=10^{-3}$ mbar ; (2) $T=780$ °C, $P(\text{O}_2)=10^{-5}$ mbar and followed by annealing at 600 °C in $P(\text{O}_2)=300$ mbar for one hour to minimize oxygen vacancies. Details about sample growth are discussed in Section 1.2.

5.3 DEVICE GEOMETRY AND FABRICATION

The device fabricated is a two-terminal capacitor structure, consisting of a circular top electrode and an electrode contacting the LAO/STO interface. As shown in Fig. 5-1(c-e), the electrodes contacting the interface are arc-shaped with a width of 20 μm and fixed separation of 50 μm to the edge of the circular top gates. The capacitor electrodes are deposited on the LAO/STO samples via DC sputtering. The arch-shaped electrodes are prepared by creating 25 nm trenches via Ar-ion milling, followed by deposition of 4 nm of Ti and 30 nm of Au. A series of metallic circular top gates (4 nm Ti and 40 nm Au) are deposited on the LAO surface Fig. 5-1(b). The entire sample (5 mm \times 5 mm \times 0.5 mm) is affixed to a ceramic chip carrier using silver paint. Electrical contacts to bonding pads on the device are made with an ultrasonic wire bonder using gold wires. (Fig. 5-1(a))

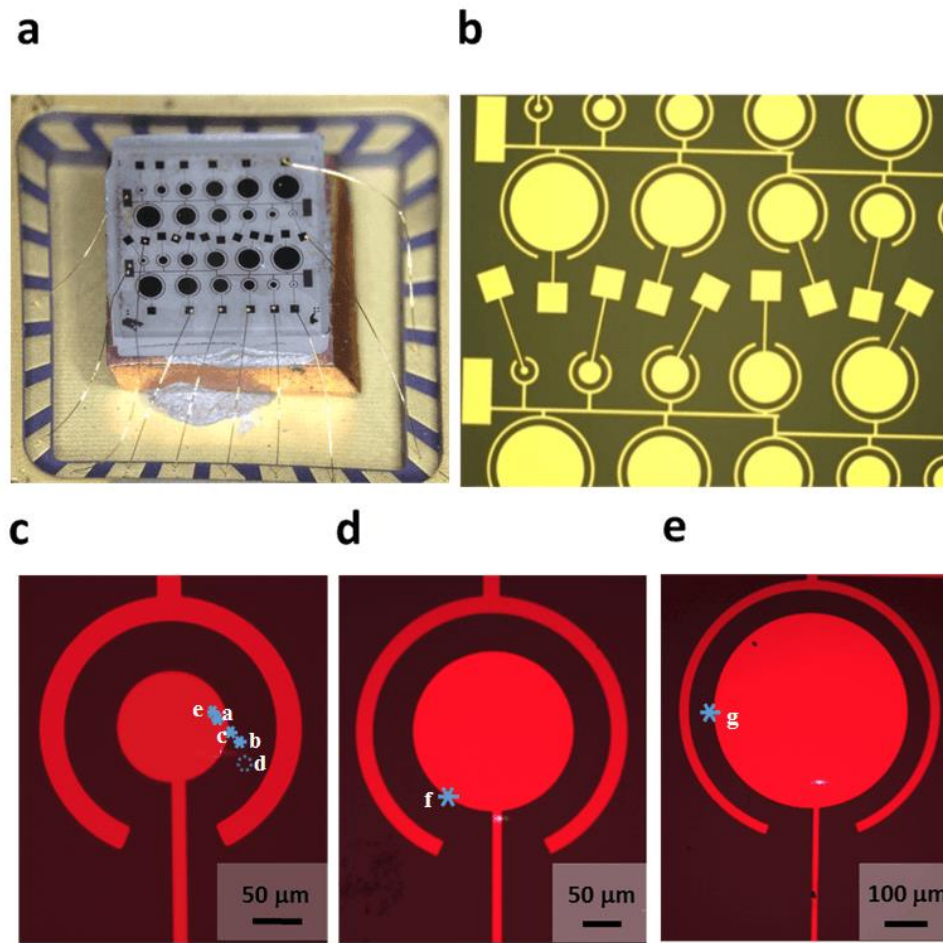


Fig. 5-1 Optical images of fabricated devices. (a), sample loaded in chip carrier with electric connections bonded. (b), fabricated devices under optical microscope. (c-e), images showing the Device A-C respectively. All the investigated areas are indicated by the markers. The red hue arises from the use of red filters to avoid any photo-excitation to the device during the experiments.

Experimental measurements are presented for three devices whose parameters are summarized in [Table 5-1](#). For consistency, the main results are presented for Device A. A summary of all experimentally investigated locations including the other two devices marked in [Fig.](#)

5-1(c- e) and a full list of all these locations with the corresponding figures are shown in Table 5-2.

	Top gate diameter	LAO thickness	Growth condition
Device A	100 μm	12 u.c.	Grow at $T= 780\text{ }^\circ\text{C}$, $P(\text{O}_2)=10^{-5}$ mbar; anneal at $T= 600\text{ }^\circ\text{C}$, $P(\text{O}_2)= 300$ mbar
Device B	200 μm	12 u.c.	Grow at $T= 780\text{ }^\circ\text{C}$, $P(\text{O}_2)=10^{-5}$ mbar; anneal at $T= 600\text{ }^\circ\text{C}$, $P(\text{O}_2)= 300$ mbar
Device C	400 μm	12 u.c.	Grow at $T= 550\text{ }^\circ\text{C}$, $P(\text{O}_2)=10^{-3}$ mbar

Table 5-1 Sample information and device parameters.

Investigated Location	Figure
a	Fig. 5-4, Fig. 5-5, Fig. 5-7, Fig. C8
b	Fig. 5-6
c	Fig. 5-8, Fig. 5-9
d	Fig. C5
e	Fig. C9
f	Fig. C7(a-c)
g	Fig. C7(d-f)

Table 5-2 List of scanning locations and corresponding figures.

5.4 EXPERIMENT METHODS AND SETUP

In this chapter, all measurements are performed in ambient conditions at room temperature. The sample is kept within a darkened chamber during experiments in order to minimize photoexcitation of carriers.

A two-terminal capacitor device is used to electrically gate the LAO/STO interface (Fig. 5-2(a)). The top circular electrode is grounded and a voltage $-V_{dc}$ is applied to the annular interface contact. (This configuration is equivalent to grounding the interface and applying $+V_{dc}$ to the top electrode.) Decreasing V_{dc} depletes the interface of mobile electrons, while increasing V_{dc} leads to electron accumulation and results in a conductive interface. The critical voltage for the metal-insulator transition (MIT) is device-dependent and generally exhibits voltage hysteresis in the range 0 V to -2 V. The transition is readily identified as an inflection point in the capacitance-voltage (CV) spectrum (Fig. 5-2(b)). The leakage current is device-dependent (Fig. 5-3) and does not scale with the top electrode area, suggesting the existence of pinholes. These leakage currents are approximately eight orders of magnitude lower than what is required to generate a measurable magnetic signal^{87,88}.

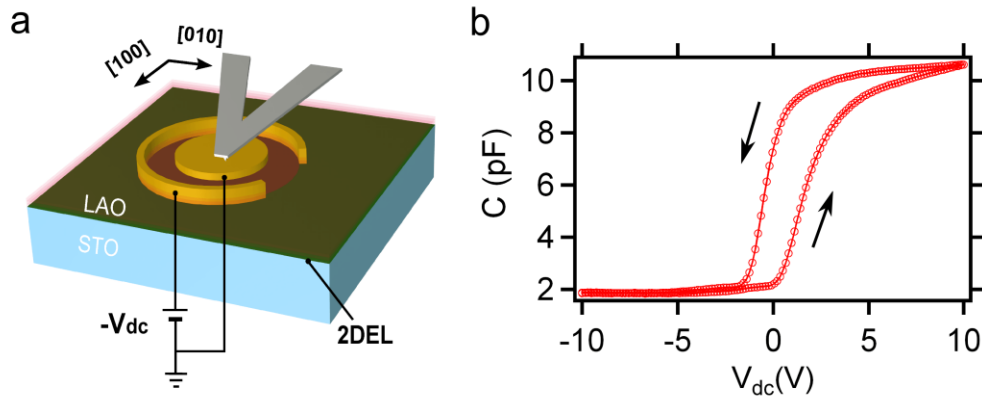


Fig. 5-2 Sketch of experimental setup and CV characterization. (a), The MFM tip is mechanically driven by a piezoelectric transducer near its resonant frequency and kept at a constant height Δh above the surface. The top electrode and MFM tip are both grounded and a dc bias is directly applied to the interface. Frequency modulation is used to lock the phase of the mechanical response at 90° . The frequency shift Δf is proportional to the force gradient. (b), CV characterization of Device A.

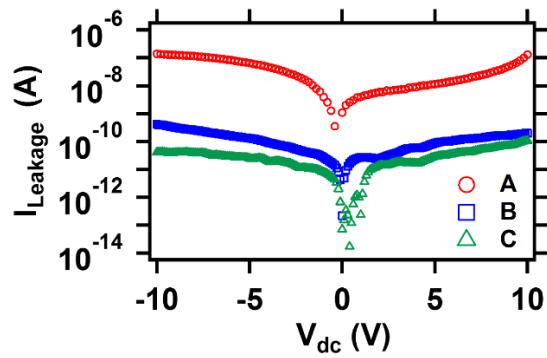


Fig. 5-3 Leakage current between top electrode and interface. Measurements are performed for Devices A-C.

A CoCr-coated AFM tip is first characterized (Appendix C: Fig. C1) and then magnetized (Appendix C: Fig. C2) with magnetic field up to 2000 Oe. A reference sample is used to verify the tip is properly magnetized (Appendix C: Fig. C3). The AFM scanning environment is shown in Appendix C: Fig. C4. In MFM mode, the cantilever is mechanically driven by a piezoelectric

transducer near its resonant frequency f_0 and kept a constant height Δh above the surface. When the tip is placed in proximity to a sample, the cantilever's resonant motion is altered in ways that can be traced directly to the force gradient $\partial F_z / \partial z$, which in turn produces changes in the amplitude ΔA , phase $\Delta \phi$ and frequency Δf of the cantilever resonance^{86,89} (Eq. (2-12),(2-13),(2-14)). Notice that the force gradients may arise from magnetic or non-magnetic interactions, so it is important to conduct experiments that can distinguish the two sources of contrast.

5.5 MEASUREMENTS

5.5.1 MFM on top-gated LAO/STO with different tip magnetization configurations (out-of-plane and in-plane) and modulated interfacial carrier density

MFM imaging using frequency modulation⁸⁹ is performed directly over the top electrode (Fig. 5-2(a)). The MFM tip and top gate are both grounded, eliminating any possible electrostatic coupling. The topographic image in Fig. 5-4(a) has nanometer-scale surface roughness associated with inhomogeneity in the Au layer. The tip is magnetized perpendicular to the LAO/STO interface and cantilever frequency-shift images are obtained for conducting ($V_{dc} = 0$ V, Fig. 5-4(b)) and insulating ($V_{dc} = -2$ V, Fig. 5-4(c)) states of the LAO/STO interface. The frequency shift is negligibly small for both voltage gating conditions, with the exception of a few topographic features. The RMS frequency shift is $\Delta f = 0.43$ Hz for $V_{dc}=0$ V and $\Delta f = 0.44$ Hz for $V_{dc} = -2$ V, close to the noise floor of 0.27 Hz for the measurement.

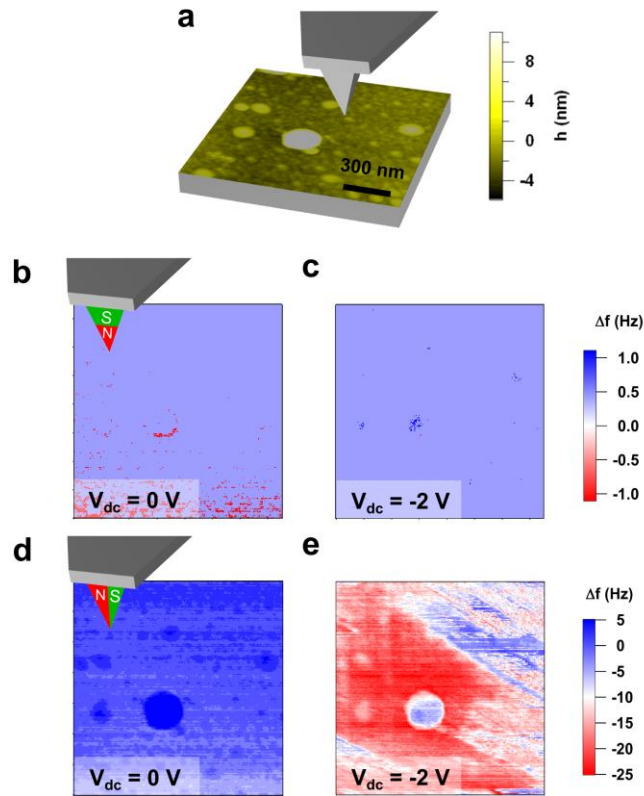


Fig. 5-4 MFM on top-gated LAO/STO. (a), AFM Surface topography data over the investigated $1.4 \mu\text{m} \times 1.4 \mu\text{m}$ area on the top electrode. (b-c), MFM frequency-shift images using vertically magnetized tip with $V_{\text{dc}} = 0 \text{ V}$ and -2 V . (d-e), MFM frequency images over the same area using tip that is magnetized horizontally along the [010] direction. Images are taken under $V_{\text{dc}} = 0 \text{ V}$ and -2 V .

The tip is then magnetized along the in-plane [010] orientation, and frequency-shift images are acquired with the same tip, over the same region on the sample, under the same voltage bias conditions as with Fig. 5-4(b-c). In the conductive state ($V_{\text{dc}} = 0 \text{ V}$, Fig. 5-4(d)), the image shows negligible spatial variations in the frequency shift. In the insulating state ($V_{\text{dc}} = -2 \text{ V}$, Fig. 5-4(e)), the frequency-shift image shows significant contrast, of order 20 Hz peak-to-peak (note the change in frequency-shift scale). The calculated force gradient magnitude, based on Eq. (2-14) and the

cantilever properties (Appendix C, Fig. C1), is of order 10^{-4} N/m. The boundaries between domains of approximately equal frequency shift are sharp, straight, and aligned approximately 30-40 degrees relative to the horizontal axis. Experiments performed at various angles between the MFM tip and the sample show that the stripe contrast is maximized for tip magnetization oriented along the [100] or [010] direction, and vanishes for tip magnetizations that approach the [110] and direction (Appendix C, Fig. C5). Experiments performed with a nonmagnetic tip show no visible contrast at any gate voltage in the range -3 V to +3 V (Fig. 5-5).

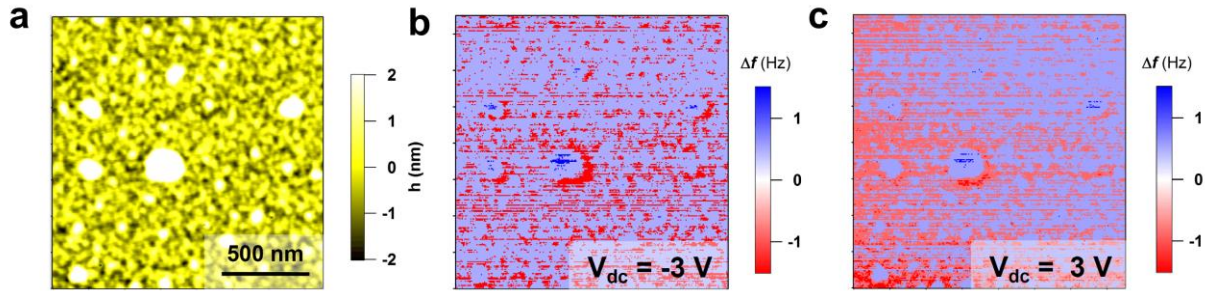


Fig. 5-5 Control MFM experiments using non-magnetic tip on top electrode over a $1.5 \mu\text{m} \times 1.5 \mu\text{m}$ area. (a), Height image. (b-c), MFM frequency image with $V_{dc} = -3$ V and $V_{dc} = 3$ V. Results are shown for Device A. The Tip is driven at its resonant frequency $f_0 = 70$ kHz at a height $\Delta h = 20$ nm above the top electrode surface.

The experiments described above provide compelling evidence for a ferromagnetic phase localized at the LAO/STO interface. The MFM tip is electrically screened by the grounded top electrode, thus ruling out contrast mechanisms that are electrical in nature. Furthermore, the strong sensitivity of the MFM contrast to the magnetization direction of the tip (Appendix C, Fig. C5, Fig. C6), holding all other experimental parameters fixed, provide compelling evidence for a magnetic interaction with an in-plane magnetized phase.

5.5.2 MFM on bare LAO close to top gate with modulated interfacial carrier density

The experiments described so far are performed over the Ti/Au-coated LAO/STO heterostructure. To help understand possible contributions associated with the metal deposition itself, as well as possible local leakage currents from the top electrode, MFM experiments are also performed directly over the LAO surface in a region $\sim 10 \mu\text{m}$ from the edge of the circular top electrode (Fig. 5-6(a)). The exposed LAO surface is atomically flat with clearly-resolved single-unit-cell 0.4 nm steps. To check that electrical gating is possible several micrometers away from the circular electrode edge, the surface potential is mapped using Kelvin-probe force microscopy (KFM). Fig. 5-6(b) shows the surface potential distribution over the investigated area with the top gate grounded and the interface biased at 3 V. A cross-sectional profile analysis shows that the electrode-induced top gating decays gradually over tens of micrometers from the top electrode edge (Fig. 5-6(c)). Within the rectangular area marked by a dashed line, MFM measurements are performed as a function of gate voltage (Fig. 5-6(d)). The first MFM image, taken at $V_{dc} = -4 \text{ V}$ (“State 1”, Fig. 5-6(d)), shows strong contrast in the frequency channel similar to that seen over the electrode. No correlation of the frequency shift with unit-cell terraces is observed. As the gate bias is increased, the contrast between domains diminishes. For $V_{dc} = -2 \text{ V}$ the domain contrast has nearly vanished, with new horizontal bands appearing parallel to the fast scan axis. For $V_{dc} = 0$, the contrast is absent. Subsequent decrease of V_{dc} restores the magnitude of the response but with a new domain pattern that is uncorrelated with the previous one (“State 2”, Fig. 5-6(d)). The observed magnetic contrast away from the electrode is qualitatively consistent with images taken directly over top electrode, indicating that neither surface leakage currents nor metal/oxide

chemistry is responsible for the magnetism. Similar results are also shown for Devices B and C in Appendix C: Fig. C7. The slight decrease in magnitude is correlated with charge hysteresis in the CV spectrum (Fig. 5-2(b)) during voltage gate sweeps.

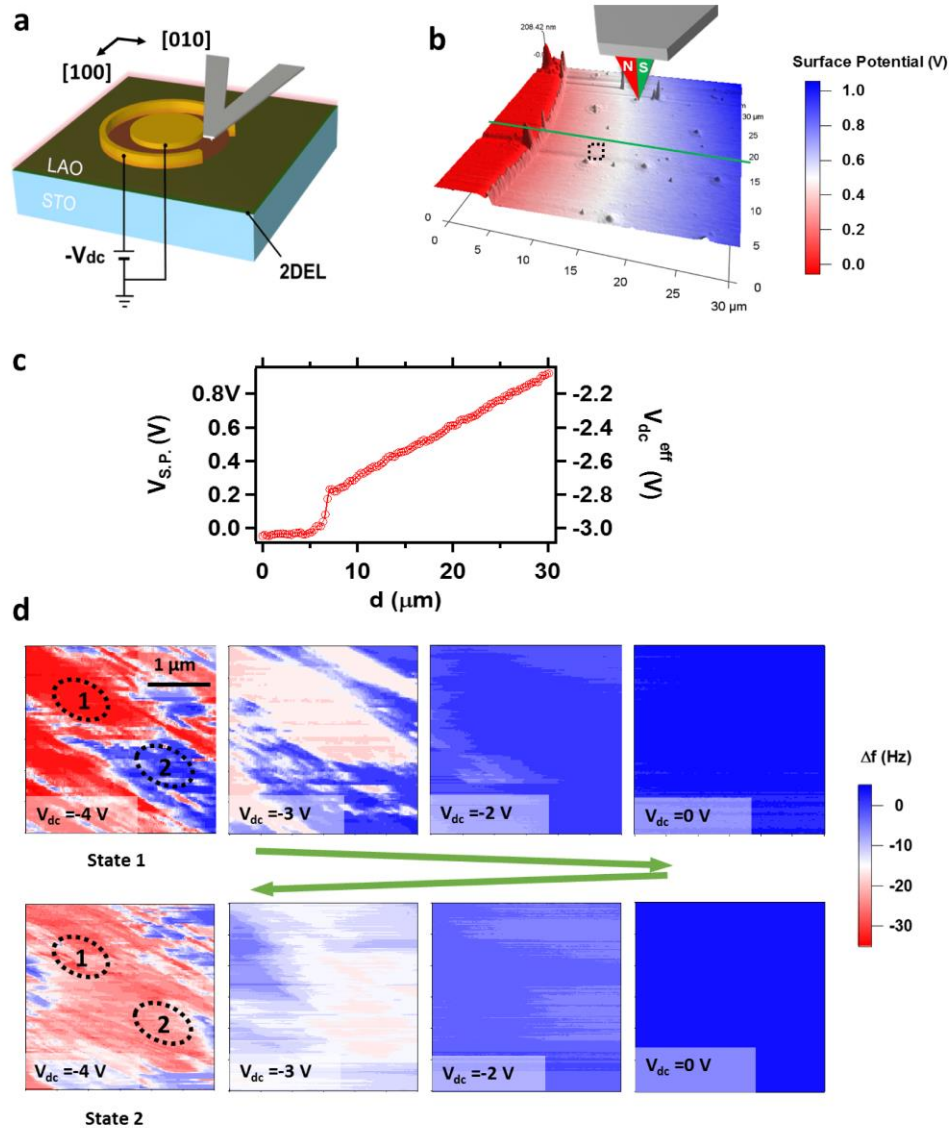


Fig. 5-6 MFM experiments performed over the exposed LAO region.(a), experimental setup, similar to that of Fig. 5-2(a), except the scanning location is now over the exposed LAO surface, approximately 10 μm away from the electrode edge. (b), Kelvin probe force microscopy measurement of a region that includes the area for which MFM

measurements are made. The voltage bias is $V_{dc} = 3$ V. The topography is shown as height, while the color maps onto the measured surface potential (the work function is already subtracted). (c), a linecut of the surface potential map, showing that voltage gating decays but is reduced by ~ 1 V in the area over which MFM images are acquired. The axis: \mathbf{d} is the coordinate along the green line in (c). (d), MFM frequency images over a $3 \mu\text{m} \times 3 \mu\text{m}$ area indicated by the black dashed line enclosed region in (b). The MFM tip is magnetized horizontally parallel to the [010] sample direction. MFM frequency images for V_{dc} increasing from -4 V to 0 V then decreasing back to -4 V. Magnetic domain features are clearly observed for $V_{dc} < -2$ V. The final State 2, obtained after cycling the voltage to $V_{dc} = 0$, is different from the initial State 1. The regions enclosed by dashed lines give example of where magnetic contrast is unchanged (region 1) or reversed (region 2) after voltage cycling.

5.5.3 Sample interfacial magnetization reorientation in successive scans

The observed large-scale domain structures in the MFM images are generally reproducible from one scan to the next (Fig. 5-7(a-b)), but there are differences in fine domain structures from successive scans that suggest tip-induced magnetization switching. The subtle changes from images acquired in succession are readily seen by examining the phase error channel (Fig. 5-7(c,d)), which is used to maintain a constant phase shift between the driving signal and the tip response. Acting as a high-pass spatial filter, the phase error image accentuates sharp features in the MFM images. A line cut perpendicular to the domain boundaries (Fig. 5-7(e)) shows that the first image taken at $V_{dc} = -2$ V exhibits domains that are as narrow as 30 nm in width; this fine domain structure is largely absent in the subsequently acquired image. Considering the MFM experiments are operated in non-contact mode and the tip never comes in contact with the surface,

the observed magnetic re-orientation of the sample is most likely due to magnetization reorientation from the magnetic tip.

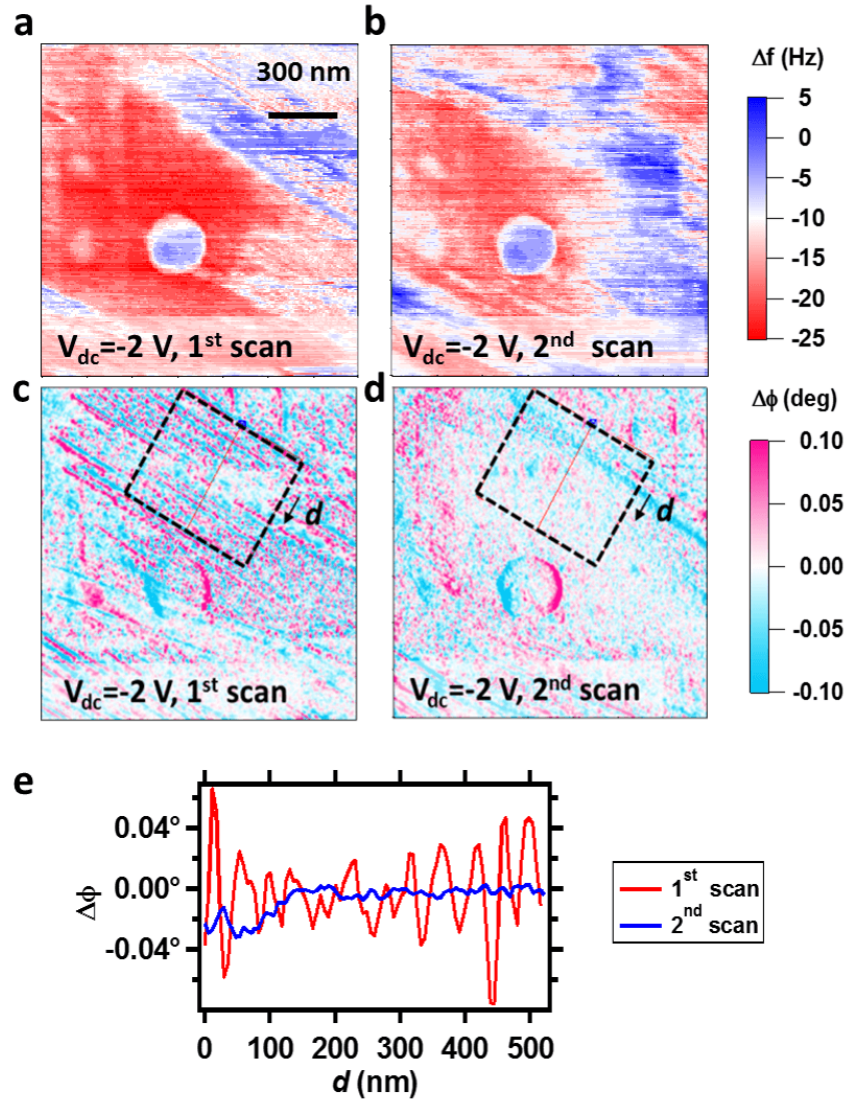


Fig. 5-7 MFM images acquired in succession. (a-b), two successive MFM frequency images and corresponding phase offset images with $V_{dc} = -2$ V. (c-d), the corresponding phase error images. (e), Averaged line scans (in the dashed box) perpendicular to domain patterns for two successive scans at $V_{dc} = -2$ V illustrate how the fine domain structure is altered by the MFM tip. Stripe domains with widths as small as 30 nm, observed in the first scan, are no longer present in the subsequent scan.

5.5.4 Dynamic magneto-electric force (MeFM) microscopy mapping

The gate dependence of the MFM images demonstrates a strong interaction between ferromagnetism and itinerant electrons. To help explore this connection, we perform dynamic magneto-electric force microscopy (MeFM) experiments (Fig. 5-8). The MeFM working principle is introduced in Section 2.2.7. The experiment set up is illustrated in Fig. 5-8(a). A bias $V_{IF} = -(V_{dc} + V_{ac} \sin(2\pi ft))$ is applied to the interface with $V_{ac} = 0.14$ V and $f = 70.6$ kHz. The tip remains at a constant height $\Delta h = 20$ nm above the LAO surface and is scanned over a $1.5 \mu\text{m}$ square area on Device A. During MeFM, the tip is not mechanically driven; instead, the interface potential is electrically modulated at the mechanical resonance of the cantilever, and the resulting ac magnetic field from the LAO induces resonant motion of the magnetized cantilever. The surface topography image is included in Fig. 5-8(b). MeFM amplitude (Fig. 5-8(c)) and phase (Fig. 5-8(d)) images are acquired at values of V_{dc} cycling between -3.5 V and 0 V. As the carrier density decreases, the contrast in MeFM images becomes stronger and sharper; while as the carrier density increases, the contrast in MeFM images becomes weaker and more diffuse. Similar contrast is also observed in MeFM images taken over the top electrode. The observed stripe domains and the contrast changes in MeFM images agree qualitatively with the results obtained by conventional MFM imaging. The coupling of the magnetic response to carrier density establishes that the electrons entering the interface become spin-polarized, aligning antiferromagnetically with the magnetic domains. The observed voltage hysteresis in the magnetic response (Fig. 5-8(c-d)) can be traced back to observed hysteresis in the CV spectrum (Fig. 5-2(b)).

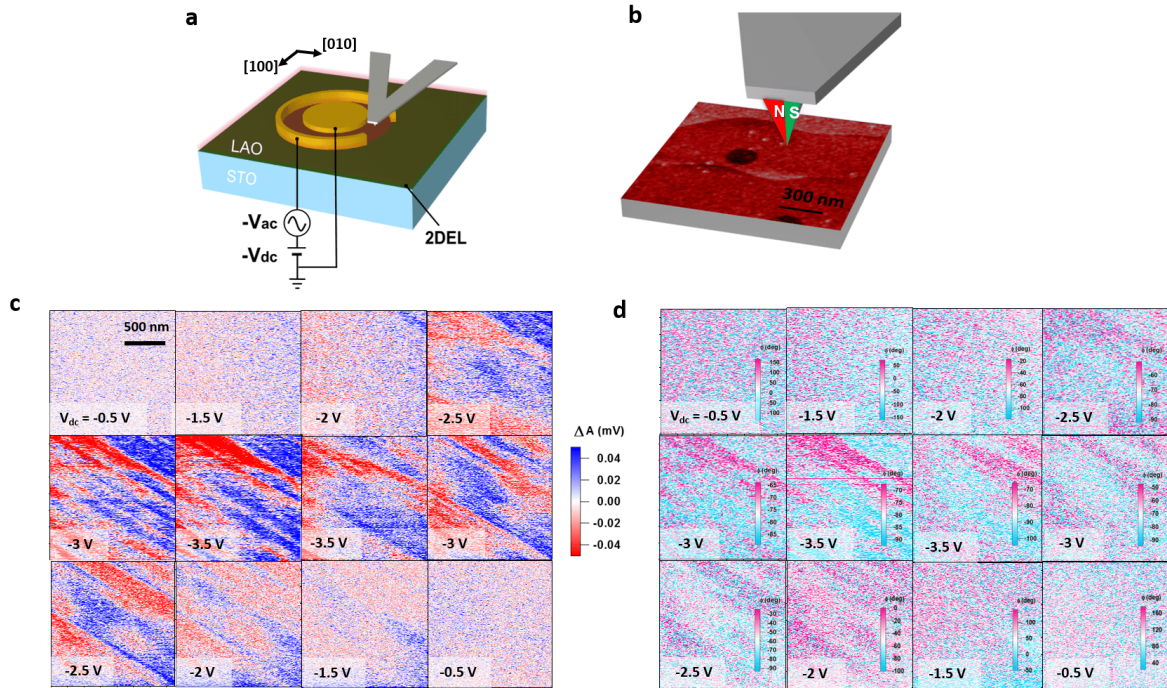


Fig. 5-8 Magneto-electric force microscopy (MeFM) experiments above the exposed LAO surface near the top electrode. (a), Sketch of the experimental setup. A combined ac and dc bias is applied to the interface with the top gate grounded. The ac bias is at a fixed frequency equal to the cantilever's free resonant frequency. Unlike MFM, the tip is not driven mechanically. The tip is electrically isolated and kept at a constant height above the sample surface during imaging. (b), Topographic image of the sample where MeFM images are acquired. Image size is $1.5 \mu\text{m} \times 1.5 \mu\text{m}$ about $\sim 5 \mu\text{m}$ away from the edge of the top electrode. (c), MeFM amplitude images acquired with V_{dc} increasing from -3.5 V to 0 V . Each image is shown with the average value subtracted: 0.04 mV , 0.05 mV , 0.09 mV , 0.2 mV , 0.3 mV , 0.4 mV , 0.3 mV , 0.2 mV , 0.1 mV , 0.09 mV , 0.06 mV , 0.06 mV . (d), Corresponding MeFM phase images.

5.5.5 2D FFT analysis of MeFM images

In order to analyze the sharpness of the domain features, 2D Fourier analysis is applied to a series of MeFM images (Fig. 5-9(a)). The corresponding 2D fast Fourier transform (FFT) spectra are shown in Fig. 5-9(b). There is a sharp peak in the 2D FFT image for $V_{dc} = -3.5\text{ V}$. As V_{dc} increases, the peak is gradually suppressed, vanishing for $V_{dc} \geq -1\text{ V}$. To quantitatively analyze the peak in the 2D FFT, a 1D section is plotted along the peak for each dc bias (Fig. 5-9(c)). The FFT results for $V_{dc} \geq -0.5\text{ V}$ are used to normalize these profiles. In Fig. 5-9(c), the cross points (black circle data) between black dashed line: $\log_{10}(\text{power spectrum}) = 0.5$ and FFT curves are defined as the cut off k_0 . As V_{dc} increases, k_0 decreases, which suggests the corresponding length scale $L_0 \sim 1/k_0$ increases. The L_0 is associated with the contrast sharpness in Fig. 5-9(a), which quantitatively shows the domain wall width.

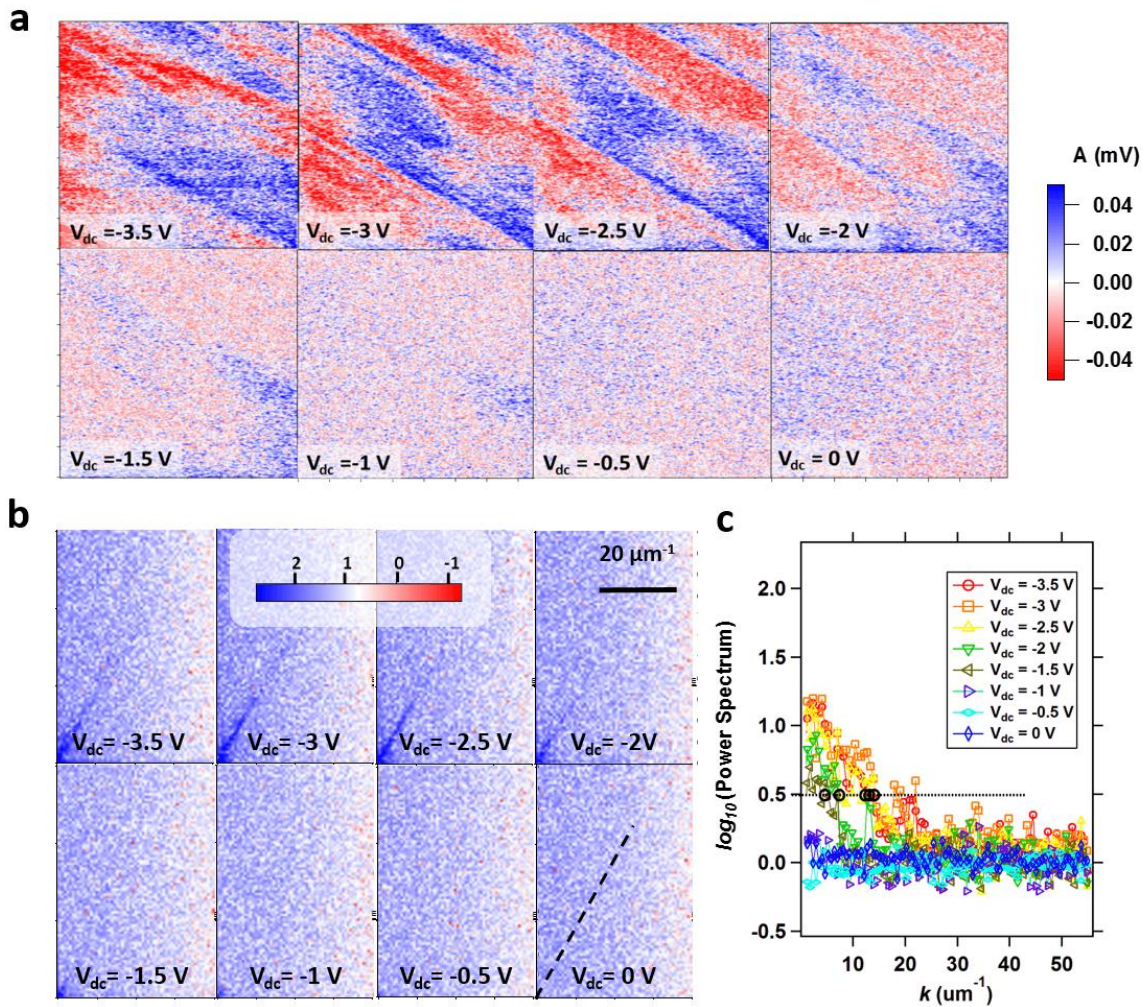


Fig. 5-9 2D Fourier analysis of MeFM results. (a), MeFM images taken under different V_{dc} . The amplitude of each image is offset 0.26 mV, 0.19 mV, 0.14 mV, 0.09 mV, 0.06 mV, 0.06 mV, 0.06 mV, 0.07 mV respectively. The scan size is $1.5 \mu\text{m} \times 1.5 \mu\text{m}$. (b), 2D FFT results for each image in (a). For each FFT image, the x axis has range from 0 to $40 \mu\text{m}^{-1}$ and the y axis has range from 0 to $60 \mu\text{m}^{-1}$. (c), FFT section profile along the dash line in (b). We have averaged the FFT results for $V_{dc} \geq -0.5$ V as the background. Each power spectrum is normalized by the value at $V_{dc} = 0$ V. The black circles show the cross points (black circle data) between the black dashed line: $\log_{10}(\text{Power Spectrum}) = 0.5$ and FFT curves.

5.5.6 Histogram analysis of MFM images

The dependence of the magnetic contrast on gate voltage V_{dc} can be quantified by performing a histogram analysis on a sequence of MFM images across the domain boundary (Fig. 5-10). The average value of the two central domains can be identified by the peaks in the double-valued histogram (Fig. 5-10(b)). Fig. 5-10(c) shows the dependence on gate voltage, which is approximately linear in the range. Scans at increasingly negative gate voltages are not performed due to a rapid increase in leakage current through the LAO.

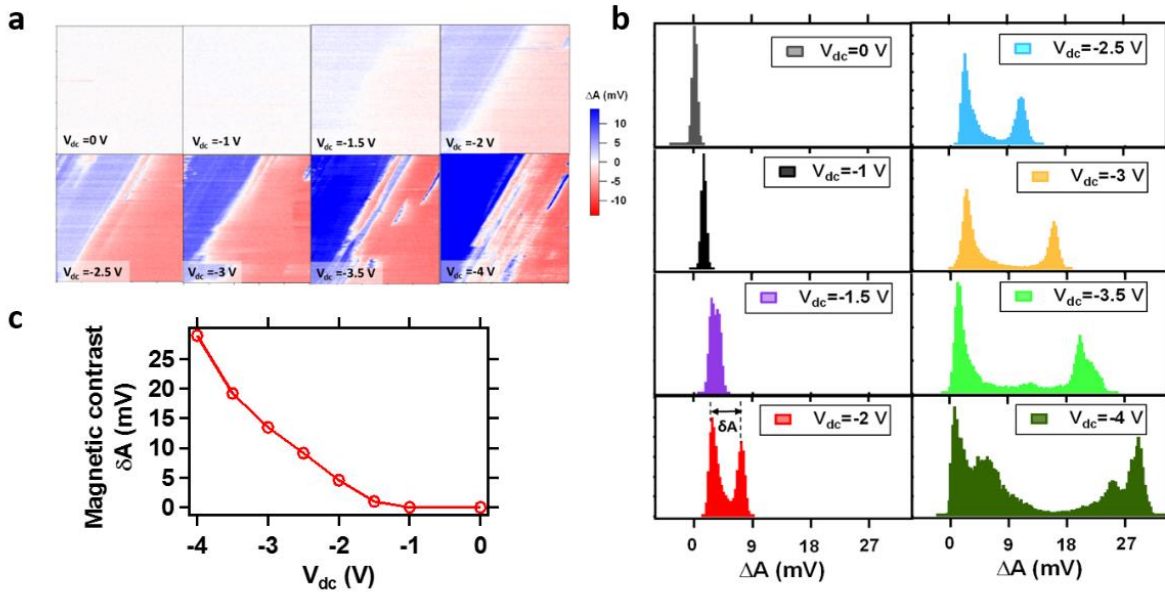


Fig. 5-10 Histogram analysis of MFM images on magnetic domain boundary. (a), MFM images on LAO near top electrode. ($1 \mu\text{m} \times 1 \mu\text{m}$). For V_{dc} from 0 V to -4 V, each image is offset 565 mV, 567 mV, 568 mV, 569 mV, 569 mV, 573 mV, 573 mV, 573 mV respectively. (b), histogram analysis of MFM images in (a). The peak in the histogram of $V_{dc}=0$ corresponds to $\Delta A=0$. The observed double peaks in histogram figures correspond to the different contrast of two magnetic domains in (a). We therefore define the magnetic contrast to be the gap δA between the two peaks, which is plotted in c as a function of V_{dc} .

5.6 DISCUSSION AND PERSPECTIVE

The MFM tip strongly perturbs the magnetic domain structure, as can be seen from successive scans (e.g. Fig. 5-7). Angle-dependent MFM measurements (Appendix C: Fig. C5) can be interpreted as evidence for in-plane anisotropy along the $[1\ 0\ 0]$ and $[0\ 1\ 0]$ directions, but it is more likely that the domains are aligned along the $[1\ 1\ 0]$ and $[\bar{1}\ 1\ 0]$ directions, with domain structure that is stable against perturbation from the MFM tip only close to $\theta=0^\circ$ (θ is the angle of sample rotation in clockwise direction). The domain walls themselves are generally sharp and resolution-limited, with apparent widths that depend on V_{dc} (Fig. 5-9). The absence of features in MFM images with vertically magnetized tips (Fig. 5-4(b-c)) has several possible explanations. One is that the domain walls are Néel-type, with magnetization rotating in the plane of the sample or vanishing at the domain wall⁹⁰. An alternate explanation is that the magnetization of the tip is too strongly perturbing of the domain state to allow them to be imaged. A third possibility is that the domain walls are too narrow to be detected.

Theories of magnetism at the LAO/STO interface generally invoke localized unpaired d_{xy} electron spins at the interface that couple via exchange with itinerant carriers. The mechanism depends on the relative density of localized versus itinerant electrons, as well as their orbital character^{84,91,92}. Fidkowski *et al.* describe a ferromagnetic Kondo model⁹² in which local d_{xy} moments couple ferromagnetically to delocalized d_{xz}/d_{yz} carriers; models with ferromagnetic exchange are also described by Joshua *et al.*⁸⁴ and Bannerjee *et al.*⁹³. Michaeli *et al.*⁹⁴ describe a model based on Zener (antiferromagnetic) exchange between localized and delocalized d_{xy} carriers⁹⁵.

The local moments themselves are postulated to arise either from electronic correlations⁹⁶ or interfacial disorder^{92,94}, or are related to oxygen vacancies^{91,97}. Extrinsic sources of magnetic impurities have been ruled out experimentally^{23,24,98}. The decrease in net magnetization with increasing carrier density (Fig. 5-10(c)) indicates that the exchange is primarily antiferromagnetic and distinct from the Kondo-related⁹⁹ ferromagnetism¹⁰⁰ reported for electrolyte-gated STO. The source of the local moments is not obviously constrained by these experiments, except for the fact that they appear to be highly uniform-domain walls are sharp and highly linear and not pinned by fluctuations in moment density. The two growth conditions explored here (see Table 5-1) are both believed to have a low density of oxygen vacancies near the interface.

The existence of room-temperature ferromagnetism at the insulating LAO/STO interface offers a pathway to resolve many of the contradictory reports regarding magnetism at the LAO/STO interface. Most experimental investigations have been performed with conducting interfaces, a regime for which higher-temperature ferromagnetism is suppressed. Any inhomogeneity that locally depletes the interface, e.g. defects or surface adsorbates⁸⁵, could give rise to local insulating regions that exhibit magnetic behavior. Similarly, LAO/STO structures grown at pressures close to the insulating transition (e.g., $P(\text{O}_2)=10^{-2}$ mbar for Ref. 24) may contain local insulating regions that exhibit room-temperature ferromagnetic behavior. Experiments by Kalitsky *et al.* suggest that there could be a critical density of interfacial carriers below which magnetism is not observed¹⁰¹. At higher carrier densities (and lower temperatures), a distinct class of magnetic behavior is observed, with signatures such as anomalous Hall effect, anisotropic magnetoresistance, and coexistence of superconductivity. Above the Lifshitz transition, local moments are predicted to align ferromagnetically with the d_{xz}/d_{yz} electrons, from Hund's rule

coupling^{84,92,93}. Such properties are distinct from the room-temperature ferromagnetism reported here.

There are many unresolved questions regarding the nature of the ferromagnetic state. First and foremost, the density of localized moments, and the relative density of delocalized carriers, is not well characterized by these MFM measurements. The magnetic moment density is a quantity that in principle can be obtained from MFM measurements but is challenging here given the fact that the magnetization is so strongly perturbed by the MFM tip. The magnetic easy axes are not readily identified, although there is clear in-plane magnetic anisotropy. Future refinements of these experiments as well as new ones will undoubtedly answer these questions and help to constrain theoretical descriptions.

The discovery of electrically-controlled ferromagnetism at the LAO/STO interface at room temperature provides a new and surprising route to a wide range of spintronics applications. Many effects - not yet demonstrated - are nevertheless expected, such as spin-torque transfer, spin-polarized transport, electrically controlled spin-wave propagation and detection, magnetoresistance effects, and spin-transistor behavior. This versatile spintronic functionality may also be combined with conductive AFM control over the metal-insulator transition³⁵, both for room temperature spintronics applications and low-temperature quantum devices.

6.0 LaAlO_3 THICKNESS WINDOW FOR ELECTRONICALLY CONTROLLED MAGNETISM IN LAO/STO HETEROSTRUCTURES

Complex-oxide heterostructures exhibit rich physical behavior such as emergent conductivity, superconductivity, and magnetism that are intriguing for scientific reasons and have the potential for technological applications. It was recently discovered that in-plane magnetism at the LAO/STO interface can be electronically controlled at room temperature¹⁰². Here we employ magnetic force microscopy to investigate electronically controlled ferromagnetism at the LAO/STO interface with LAO thickness t varied from 4 u.c. to 40 u.c. Magnetic signatures are observed only within a thickness window 8 u.c. $< t < 30$ u.c. Capacitance measurements for identical devices differing only in the thickness show that those devices which lack magnetic signals all have a capacitance value far below the geometric value. Outside of this thickness window, direct or Zener tunneling cause significant leakage, preventing effective top-gating of the capacitor structure.

6.1 INTRODUCTION

Advances in the growth of precisely tailored complex-oxide heterostructures have led to new emergent behavior and associated discoveries and surprises. One of the most celebrated examples consists of heterostructures formed from ultrathin layers of LaAlO_3 (LAO) deposited on TiO_2 -terminated SrTiO_3 (STO) substrates, where a two-dimensional electron liquid (2DEL) was

found at the interface¹. Other emergent properties, including tunable metal-insulator transition^{2,12,53}, superconductivity^{20,21}, strong Rashba-like spin-orbit coupling^{18,19} and ferromagnetism²³⁻²⁷ have also been reported. Among them, spin-orbit interactions and magnetism at the LAO/STO interface are of particular interest for spintronic applications.

Previous investigations of magnetism at LAO/STO interfaces are discussed earlier in the thesis, especially in Section 5.1. Among these studies, the scanning SQUID measurements performed at low temperature shows that there is a critical LAO thickness for the interfacial magnetization.¹⁰³ The magnetic patterns were observed by scanning SQUID only when the LAO thickness exceeds 3 u.c. On the other hand, our magnetic force microscopy (MFM) measurements revealed a new electronically controlled ferromagnetic phase at room temperature¹⁰² (Section 5.0). It will be intriguing to study the LAO thickness dependence of such electronically controlled ferromagnetism.

6.2 SAMPLE GROWTH

A series of LAO/STO heterostructures are prepared with LAO thickness range from 4 u.c. to 40 u.c. using the pulsed laser deposition method. Details about sample growth are discussed in Section 1.2. Here all the investigated samples are listed in [Table 6-1](#).

description	Growth condition
4 u.c. LAO/ (100)STO	Sample growth at 780 °C with oxygen partial pressure 10^{-5} mbar. The STO substrate miscut angle $< 0.2^\circ$
6 u.c. LAO/ (100)STO	
8 u.c. LAO/ (100)STO	
10 u.c. LAO/ (100)STO	
16 u.c. LAO/ (100)STO	
20 u.c. LAO/ (100)STO	
25 u.c. LAO/ (100)STO	
30 u.c. LAO/ (100)STO	
40 u.c. LAO/ (100)STO	

Table 6-1 Sample information.

6.3 DEVICE GEOMETRY AND EXPERIMENT METHOD

The two-terminal-capacitor devices, consisting of a circular shape top electrode and arc-shaped interface electrode, are fabricated on LAO/STO to modulate the carrier density at the interface. As shown in [Fig. 6-1](#), the gold circular top electrodes with a size of $100\ \mu\text{m}$ and thickness of $10\ \text{nm}$ are deposited on the LAO surface via DC sputtering. The arc-shaped electrodes contacting the interface are prepared by creating $25\ \text{nm}$ trenches via Ar-ion milling, followed by deposition of $4\ \text{nm}$ of Ti and $30\ \text{nm}$ of Au. These interfacial electrodes have a width of $20\ \mu\text{m}$ and fixed separation of $50\ \mu\text{m}$ to the edge of the circular top gates. The entire sample ($5\ \text{mm} \times 5\ \text{mm} \times 0.5\ \text{mm}$) is affixed to a ceramic chip carrier using silver paint. Electrical contacts to bonding pads on the device are made with an ultrasonic wire bonder using gold wires.

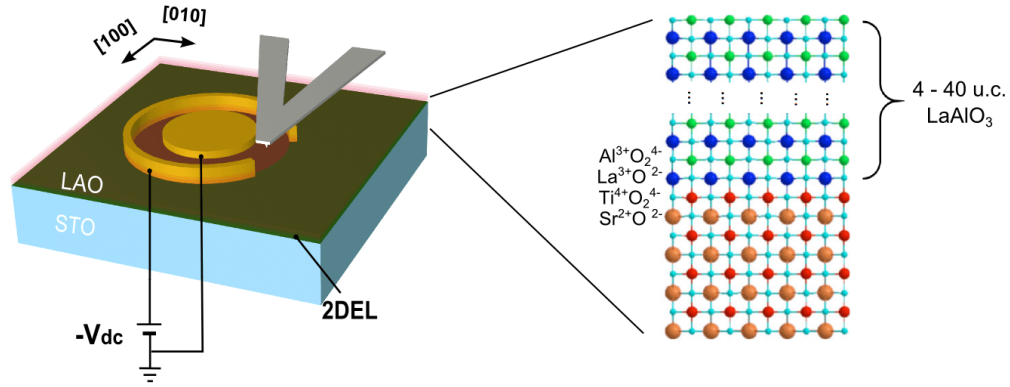


Fig. 6-1 Schematic of experimental setup and devices.

6.4 MEASUREMENTS

The experimental set up is illustrated in Fig. 6-1. The top electrode is grounded to minimize the electro-static interaction with the AFM probe. A DC bias ($-V_{dc}$) is applied to the arc-shaped electrode, which contacts the interface (equivalent to applying $+V_{dc}$ to the top gate while keeping the interface grounded). Decreasing V_{dc} suppresses the carrier density at the interface, while increasing V_{dc} will restore electrons to the interface and an associated conductive phase.

Magnetic force microscopy (MFM)⁸⁶ is employed to search for magnetic domain structure at the LAO/STO interface with varied LAO thickness. The MFM probe with CoCr coating was horizontally magnetized in a uniform magnetic field (2000 Oe). During the MFM imaging, the tip oscillates near its resonant frequency and keeps a constant height Δh above the sample surface. Any magnetic interaction between tip and sample will alter the cantilever's resonant motion, leading to a shift of resonant frequency (Eq. (2-14)).

MFM imaging using the frequency modulation method⁸⁹ (Section 2.2.6) is performed over $1 \mu\text{m} \times 1 \mu\text{m}$ area above the LAO close to the edge of top electrodes for all the investigated samples. The phase between the driving signal and the tip response is kept at 90° through a frequency feedback loop. The MFM images are obtained by tracking the frequency during spatial scanning. With the interface in conducting phase, there is no observable magnetic contrast in the MFM images, which agree with the previous reports. When the interface is modulated at the low carrier density region by decreasing V_{dc} , the magnetic contrast in MFM image is observed in a finite LAO thickness window. Below or beyond a certain LAO thickness, the magnetic signal is undistinguished from noise. Fig. 6-2 shows the MFM frequency images for samples with varied LAO thickness and $V_{dc} < -1 \text{ V}$. When LAO thickness is 4 u.c. and 6 u.c., the magnetic signal is negligible. As an LAO thickness of 8 u.c., the stripe like magnetic domain patterns appear in the MFM images. Notice at 16 u.c., the sample displays the sharpest domain wall with the size about tens of nanometers. As the LAO thickness is increased further, the domain structures become broader (20 u.c. and 25 u.c.) and finally vanish beyond 30 u.c.

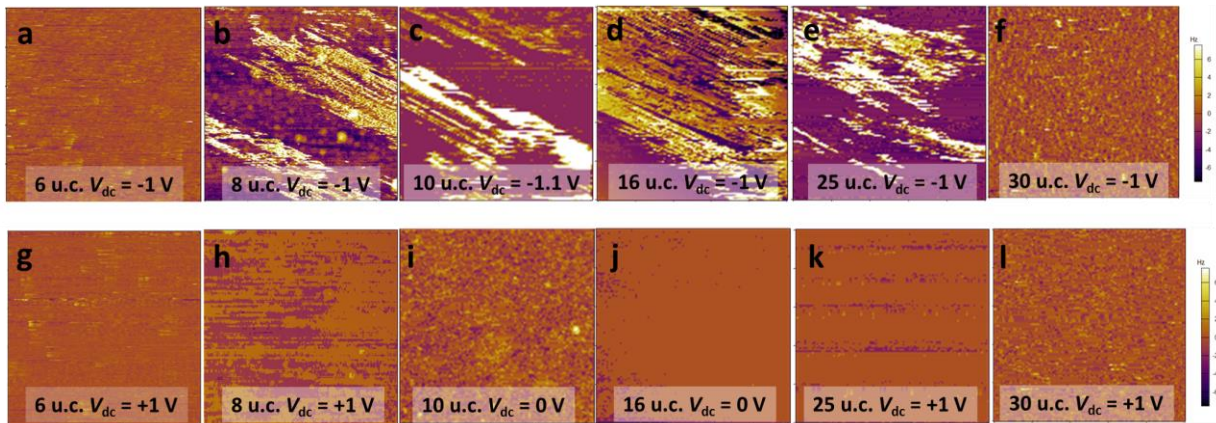


Fig. 6-2 MFM on LAO/STO with LAO thickness range from 4 u.c. to 40 u.c. (a-f), MFM frequency shift images for samples with LAO thickness 6 u.c., 8 u.c., 10 u.c., 16 u.c., 25 u.c., 30 u.c. when the interface is tuned to be insulating. (g-l), MFM frequency shift images for MFM images over the same investigated areas while the interface is conducting.

To understand why there might be a LaAlO₃ thickness window for electronically controlled magnetism, we measured the thickness dependence of the capacitance (Fig. 6-3) when the interface is the conducting phase ($V_{dc} = 0.2$ V). Interestingly, there is also a thickness window from 8 u.c. to 25 u.c., where the capacitance value can be fit to the following formula:

$$C = C_0 + \frac{\varepsilon A}{d} \quad (6-1)$$

where the fitting gives the coefficient $C_0 = 0.5$ nF and $\varepsilon A = 6.2 \times 10^{-18}$ F·m. (Corresponding to $\varepsilon_r \sim 14$, this value is lower than the dielectric constant of a LAO single crystal, close to the reported value $\varepsilon_r \sim 18$ in Ref. 51). Outside the thickness window, the device's capacitance is greatly reduced. The thickness window observed in capacitance measurements matches with the window observed in MFM measurements (the green filled data plots show the samples with electronically controlled ferromagnetism).

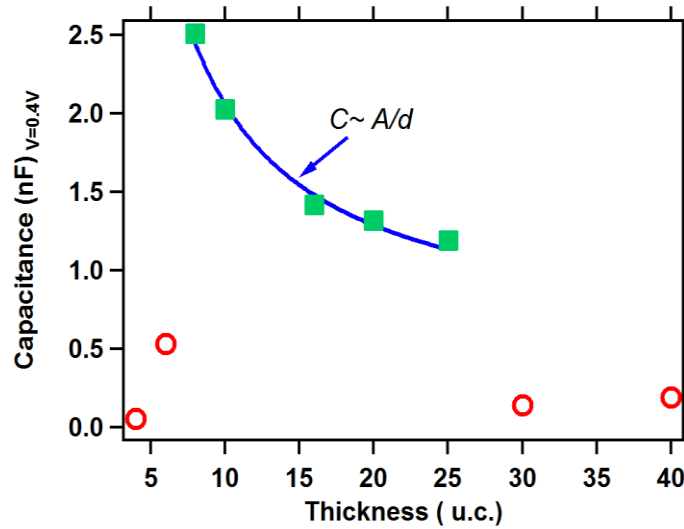


Fig. 6-3 Device capacitance with respect to the LAO thickness.

6.5 DISCUSSION AND CONCLUSION

We propose that the electronically controlled magnetism depends on the effective tuning of mobile carriers at LAO/STO interface. When the LAO thickness is less than 8 u.c. or larger than 25 u.c., the capacitance value is far below the geometry capacitance, indicating a large tunneling current through LAO. Increased tunneling current below or above a certain LAO thickness agrees with the results of tunneling experiments performed by Singh-Bhalla *et al.*⁵⁴, who showed that when the LAO thickness falls below ~ 10 u.c., the tunneling current increases drastically, dominated by direct tunneling through the LAO. When the LAO thickness exceeds ~ 20 u.c., a sharp increase of tunneling current is observed, which is associated with Zener tunneling across the polar LAO layer. For the magnetism experiments, the existence of large tunneling currents can prevent the electron density from reaching a value at which magnetism is observed. The tunneling of unpolarized electrons can also destabilize a magnetic state even if a highly insulating phase could be reached. Previous reports of ferromagnetism using scanning SQUID microscopy have reported a lower critical thickness of 4 u.c.¹⁰³ These experiments were performed at cryogenic temperatures (~ 4 K) and the magnetic phase boundary as well as the tunneling properties may have a temperature dependence that can interpolate between these two distinct results; alternatively, the magnetic “patches” could have a different physical origin from the room-temperature effects reported here.

To summarize, electronically controlled ferromagnetism experiments at room temperature are performed on samples with varied LAO thickness. Results demonstrate that ferromagnetism is only observed within a finite LAO thickness window. Such phenomenon is attributed to the tunneling current within LAO, where outside the LAO thickness window, the tunneling current

increases abruptly and makes the capacitor device lose the electronic control of ferromagnetism at the interface.

7.0 SUMMARY AND OUTLOOK

Oxide semiconductors, especially LAO/STO, show a wide range of emergent properties. Many high-performance novel devices are demonstrated in this platform.

In this thesis, we use AFM to investigate the mechanism of conductive-AFM lithography on 3 u.c. LAO/STO. We employ piezoresponse force microscopy to study the electro-mechanical response of the top-gated device on LAO/STO. We also use MFM to demonstrate the existence of electronically controlled ferromagnetism at the LAO/STO interface at room temperature and its dependence of LAO thickness. All these projects show the different interesting properties of LAO/STO. A lot of future experiments can be expected.

The mechanism of AFM lithography on LAO/STO reveals that the surface chemical process plays a key role to create or erase the conducting channels at the interface. Therefore engineering the LAO surface could have a large influence on the interface properties. Future experiments, such as AFM lithography on self-assembled monolayer coated LAO/STO or ferroelectric material coated LAO/STO, can be expected to increase the lifetime of written nanostructures.

PFM study of LAO/STO demonstrates that PFM is a powerful tool to resolve the carrier density difference at the LAO/STO interface. An obvious application is using PFM to directly image the conducting nanostructures that are created by c-AFM lithography, which is already reported by Huang *et al.*³⁷ in our group. Future experiments will be employing PFM to investigate a sketched single electron transistor at low temperature using our home designed low temperature AFM system (Appendix B).

MFM experiments on top gated LAO/STO exhibit the electronically controlled ferromagnetism at the LAO/STO interface. However, such experiments do not give the coercive field and the magnitude of the observed magnetization. MFM experiments under external magnetic field will be expected to gain the information about the coercive field. Other experiments such as X-ray magnetic circular dichroism measurements, neutron reflectometry measurements and superconducting quantum interference device measurements, are scheduled to obtain the magnitude of the observed magnetism.

APPENDIX A

AFM LITHOGRAPHY SOFTWARE

A LabVIEW™-based AFM lithography program is developed to perform conductive AFM lithography on several different AFM systems in the laboratory. The program converts vector-based graphics (predefined .svg file) into a lithography toolpath and then drives the tip to move along the path on the sample surface with the specified speed v and dc voltage V_{tip} . The program uses the state-machine architecture and the front panel is displayed as [Fig. A1](#).

Here I make a brief introduction about each labeled part of the front panel in [Fig. A1](#):

1. Command list, which includes ‘configure’, ‘run’ and ‘end’ commands. ‘Configure’ command updates all the lithography parameters. ‘Run’ command executes the lithography. ‘End’ command finishes all the lithography.
2. Command execution button, which triggers the command execution.
3. Image window, which shows the AFM lithography pattern overlay on the AFM height image.
4. This page is about AFM image loading, lithography patterns loading and lithography setting.
5. This page is about data acquisition setting and instrument set up.
6. This page is about lithography sequence setting, pattern selection and lithography loading force setting.
7. This page shows all the monitored 9 channels.
8. This page is about the lithography pattern adjustment (x , y offset, rotate, scale etc.).
9. This page is about AFM image setting, including resolution, cropping, etc.

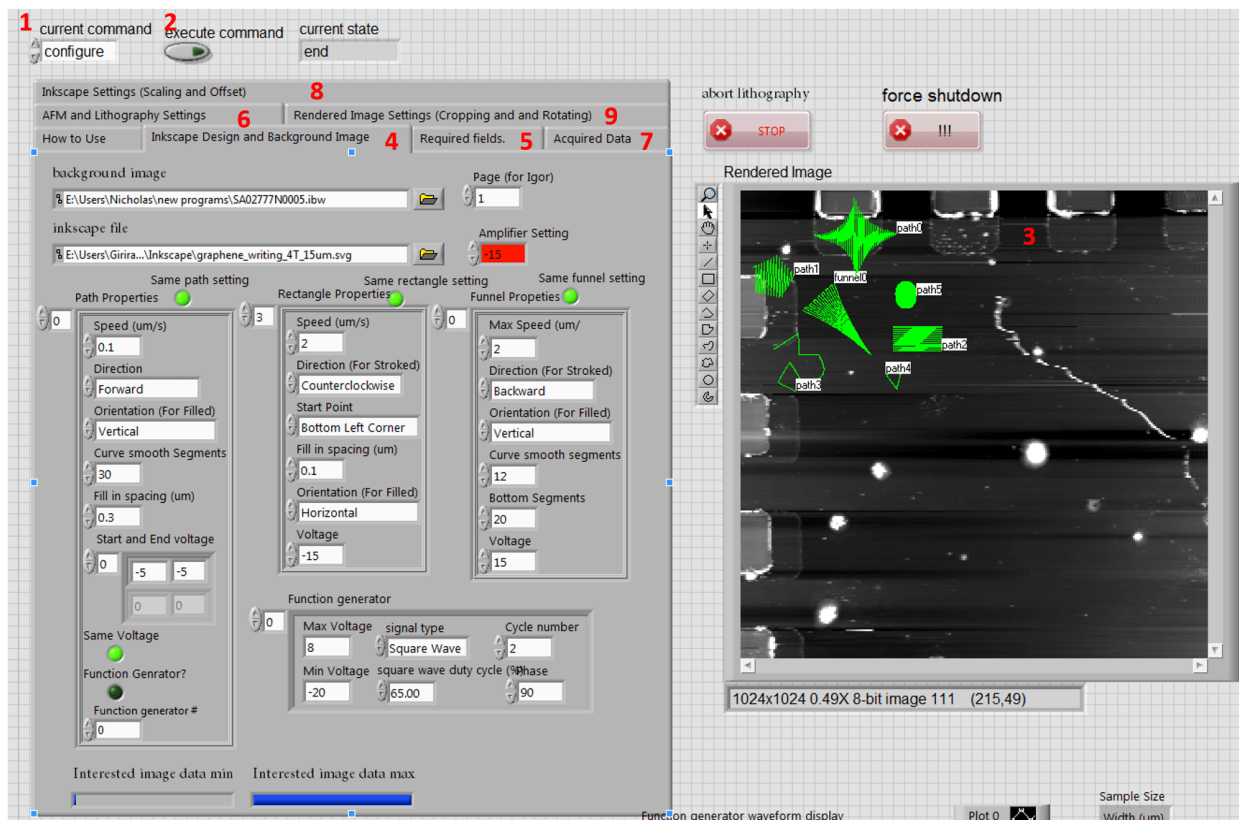


Fig. A1 Front panel of the AFM lithography program.

The front panel details in tab controller 4-9 are shown in [Fig. A2](#). Here is the explanation of each labeled part.

10. File path of AFM image.

11. File path of predefined lithography patterns. (.svg file)

12. Layer selection of AFM image. For contact mode image, 0- height; 1- deflection; 2- Z sensor. For AC mode image, 0-height; 1- amplitude; 2- phase; 3- Z sensor. Sometimes, deflection layer or amplitude layer shows a sharper surface feature, which could be helpful for lithography pattern alignment.

13. Tip voltage gain setting. Set the gain value if a voltage amplifier is used for tip bias.

14. Parameter settings for lithography patterns, which include lithography speed, pattern fill spacing, tip voltage and lithography orientation.
15. AFM image contrast adjustment. It sets the low coercive value: min% and high coercive value: max%. This function is good to enhance contrast of the small height difference features, e.g. graphene on LAO/STO.
16. Function generator setting for AFM tip bias. It can be used to generate pulses for quantum dot array writing or generate a saw tooth wave for diode device writing.
17. Setting the six data acquisition channels: z height, x tip position, y tip position, deflection, 4-terminal current, 4-terminal voltage.
18. Parameter settings of two lock-in amplifiers for 4-terminal measurements.
19. Option to display the saved .tdms lithography data.
20. Setting the file path and file name for the lithography data (.tdms format).
21. Indicator showing the AFM scan offset.
22. Contact set point during the lithography. This value should be higher than the AFM deflection. The higher the set point, the larger the tip loading force.
23. Contact set point when the tip moves from the end of one pattern to the beginning of another pattern. If you set the value higher than the deflection, the tip will engage on the surface when moving from the end of one pattern to the beginning of another pattern. If you set the value lower than the deflection, the tip will retract from the surface when moving from the end of one pattern to the beginning of another pattern.
24. Option to turn off /remain on all the PIDS loops after the lithography.
25. Option to withdraw / engage the tip after the lithography.
26. Spacing of interpolated points.

27. Lithography patterns selection. Reset button can refresh the lithography pattern list in 28.

28. Lithography patterns list. You can change the lithography sequence here or select a portion of patterns for lithography. Notice here 'r' means rectangular, 'p' means path (polyline or curve), 'f' means funnel.

29. Nine x - y graph indicators showing the Z height, tip x position, tip y position, deflection, tip voltage, two-terminal conductance, two-terminal resistance, four-terminal conductance, and four-terminal resistance graph.

30. Option to discard/keep the x - y graph history. Discarding can save memory if you do not want to display the previous lithography data.

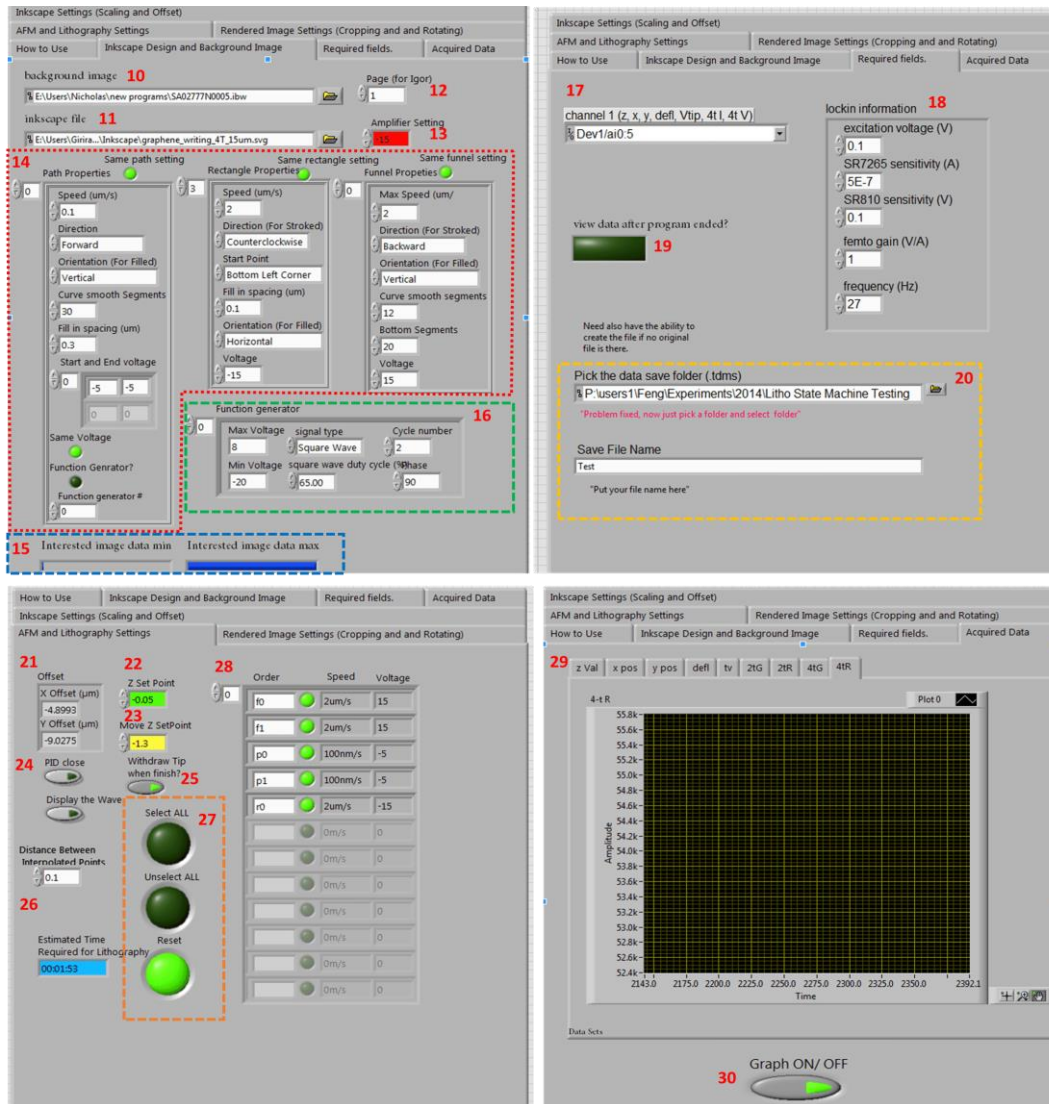


Fig. A2 Front panel of important tab pages (4-7 in Fig. A1).

The program structure (block diagram) shown in Fig. A3 consists of the state machine part and the data acquisition part.

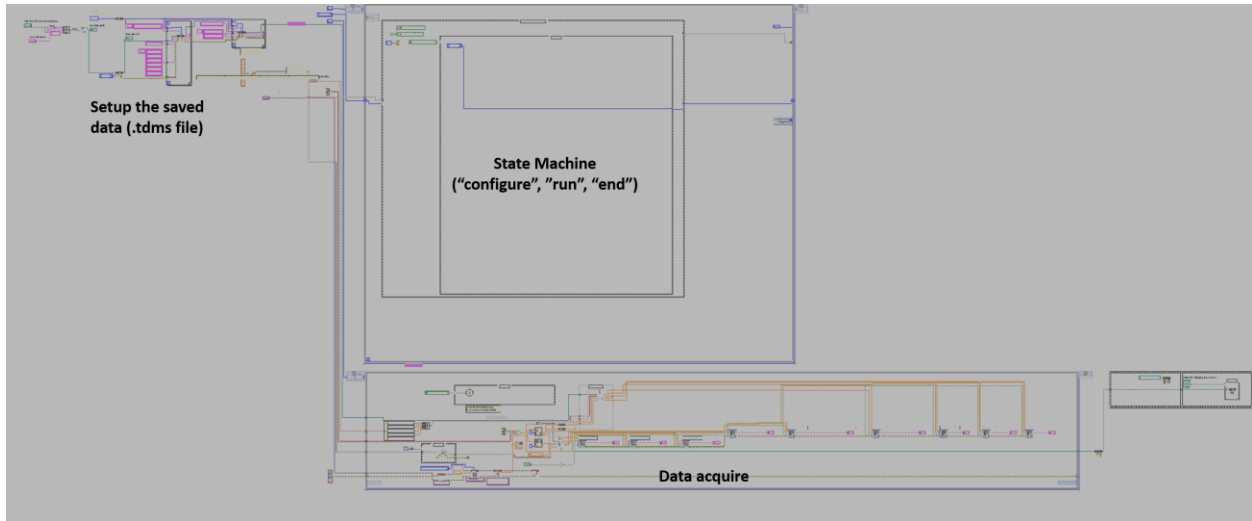


Fig. A3 Block diagram of the program.

The key parts of the program are the state machine frames. Fig. A4 exhibits the ‘initialize’ case of the state machine. The subVIs communicate with *Igor Pro* (AFM operation platform), and read out the sensitivities of linear variable differential transformer (LVDT) sensor. (If the AFM lithography program needs to run in a simulation mode without the AFM hardware connection, please replace these subVIs with constant parameters.)

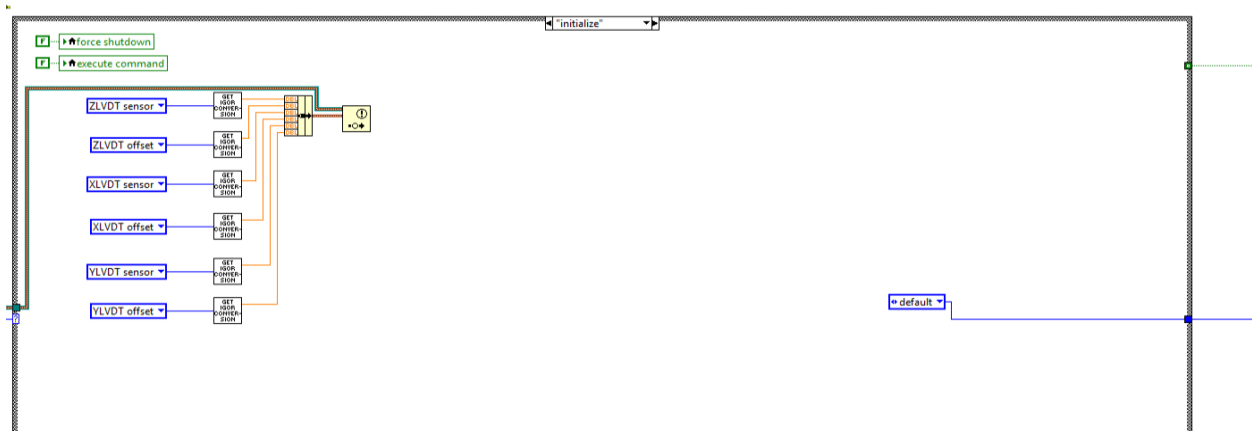


Fig. A4 ‘initialize’ case of the state machine.

Fig. A5 exhibits the ‘Configure’ case of the state machine, which loads the AFM image and lithography patterns, and overlays them with each other. The functions of labeled subVIs are explained here.

31. ‘Config A’ subVI loads the predefined lithography patterns from the .svg file and extracts the critical nodes $[(x_0, y_0), (x_1, y_1) \dots (x_n, y_n)]$ for each pattern.

32. ‘Config B’ subVI makes lithography pattern adjustments, including offset, scaling, rotation, etc.

$$\begin{bmatrix} x'_n \\ y'_n \end{bmatrix} = \begin{bmatrix} \cos \theta & \sin \theta \\ -\sin \theta & \cos \theta \end{bmatrix} \begin{bmatrix} x_n \times \alpha\% \\ y_n \times \beta\% \end{bmatrix} + \begin{bmatrix} d_x \\ d_y \end{bmatrix}$$

The critical nodes becomes $[(x'_0, y'_0), (x'_1, y'_1) \dots (x'_n, y'_n)]$ after transformation.

33. ‘Litho interpolate’ subVI fills the lithography pattern with polylines or Bezier curves based on the line spacing and lithography orientation. So in this step, the lithography pattern converts to toolpath.

34. This subVI loads the AFM image and overlays the generated lithography toolpath on the AFM image using NI-IMAQ tools.

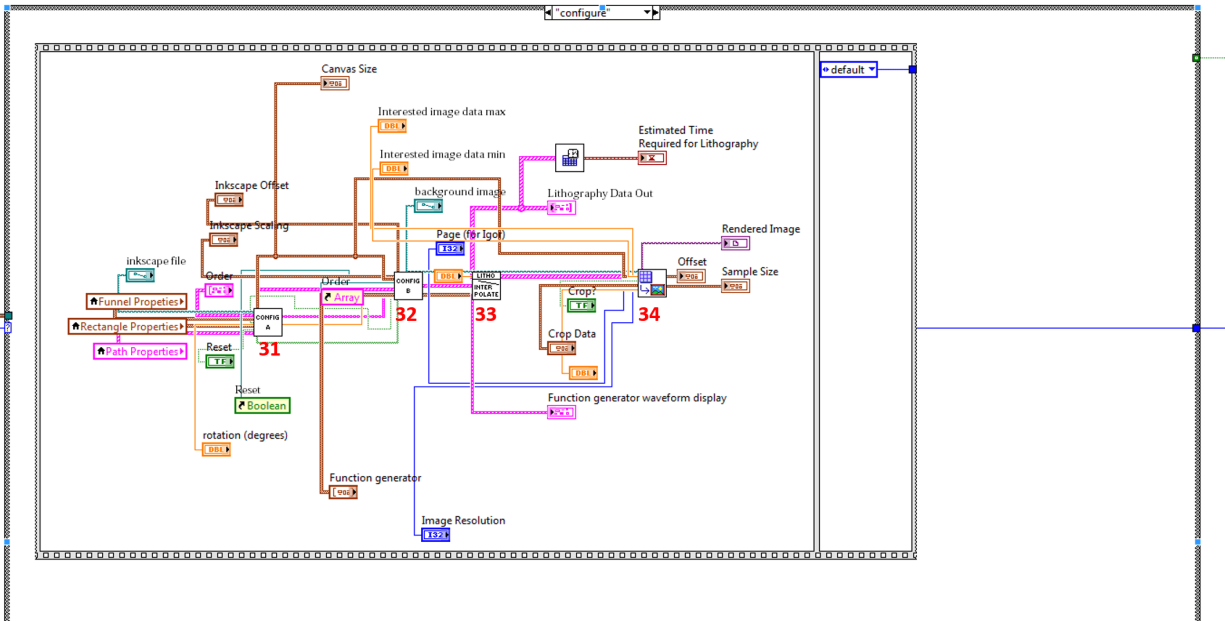


Fig. A5 ‘Configure’ case of the state machine.

Fig. A6 exhibits the ‘Run’ case of the state machine, which communicates with the AFM and sends out Igor commands to execute the lithography according to the toolpath (labeled 35 part). For different AFM systems, the corresponding AFM drive program needs to be used in frame 35.

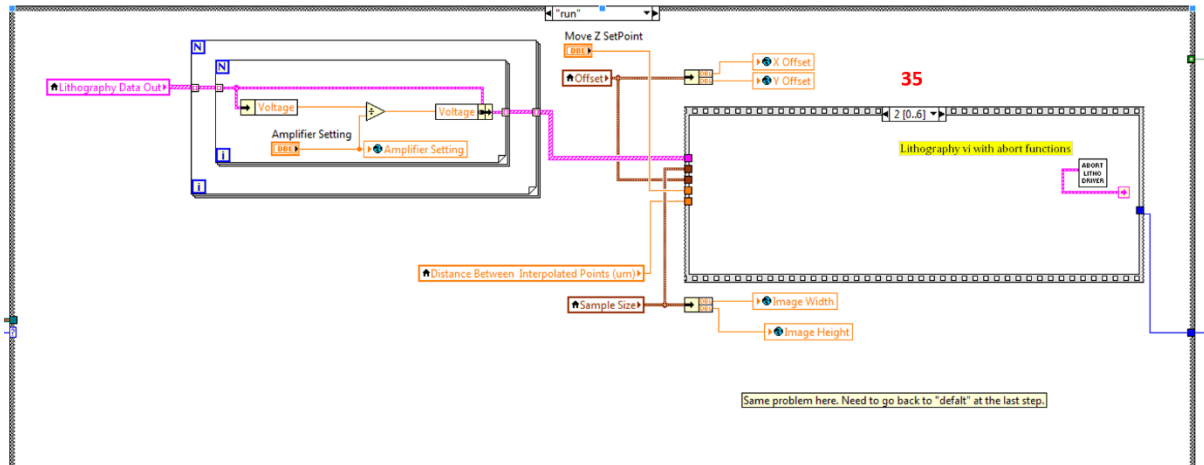


Fig. A6 ‘Run’ case of the state machine.

Here I just document my Cypher/MFP3D AFM drive codes (*Igor Pro* code) as follows. Notice these are the script codes that written in .ipf (*Igor* procedure file). It can be saved to the *Igor* library and called as a customized function. (In the *LabVIEW* program, I just make each of the commands here as a subVI and send them to *Igor*).

Function `LevyLabRamp(size, MoveSetPoint, MoveTime)` actually moves the tip from its current position to the start point of the lithography pattern. The lithography toolpath is pre-stored in a .txt file. In the function, ‘size’ means the number of nodes in lithography toolpath, ‘MoveSetPoint’ is the contact mode deflection set point and ‘MoveTime’ is the time that is required to move the tip from the current position to the start point of the lithography pattern.

Function LevyLabRamp(size, MoveSetPoint, MoveTime)

```
Variable MoveSetPoint
Variable MoveTime
Variable size
Variable Error=0

Make/O/N=(size) XMove YMove XMove1 YMove1
Make/O/N=2 XRamp YRamp
LoadWave/O/A/J/D/W/K=0 "E:litho wave file:XMove wave.txt"
LoadWave/O/A/J/D/W/K=0 "E:litho wave file:YMove wave.txt"

GetGains()
//read out original PID parameters.
NVAR X_IGain, X_SGain, Y_IGain, Y_SGain

XMove = XMove1
YMove = YMove1

//Display YMove vs XMove
ModifyGraph mode=4

Error += td_stop()
Error += td_StopInWaveBank(-1)

Error += ir_SetPISLoop(0, "Always,Never", "XSensor", NAN, 0, X_IGain, X_SGain, "Output.X",-10, 150)
Error += ir_SetPISLoop(1, "Always,Never", "YSensor", NAN, 0, Y_IGain, Y_SGain, "Output.Y",-10, 150)
Error += ir_SetPISLoop(2, "Always,Never", "Fast%Input", MoveSetPoint, 0, 1000, 0, "Output.Z",-10,150)

XRamp[0] = td_RV("PIDSLoop.0.Setpoint")
YRamp[0] = td_RV("PIDSLoop.1.Setpoint")
XRamp[1] = XMove[0]
YRamp[1] = YMove[0]

Error += td_xSetOutWavePair(0, "0", "PIDSLoop.0.Setpoint", XRamp,"PIDSLoop.1.Setpoint",YRamp, -50000*MoveTime)
Error += td_WriteString("Event.0", "once")

if(Error)
    print "Error in LevyRamp", Error
endif
End
```

Function LevyLabShortLitho(size, interpolatepoint, LithoSetPoint) moves the tip through the entire lithography toolpath. ‘size’ represent the number of nodes in the lithography toolpath. ‘interpolatepoint’ will be the total lithography time times -50000. The ‘LithoSetPoint’ is contact mode deflection set point during lithography.

```

Function LevyLabShortLitho(size, interpolatepoint, LithoSetPoint)
//This function need to used with LevyRamp function. First ramp from current position to start point. Then do the litho following your
//path. This function do not include the PID setting since it is set in LevyRamp function.

Variable size
Variable interpolatepoint
Variable LithoSetPoint
Variable Error=0

Make/O/N=(size) XMove YMove XMove1 YMove1 VoltageWave OutWave4
Make/O/N=(size) XTrack YTrack VoltageTrack Wave4Track
LoadWave/O/A/J/D/W/K=0 "E:litho wave file:XMove wave.txt"
LoadWave/O/A/J/D/W/K=0 "E:litho wave file:YMove wave.txt"

XMove = XMove1
YMove = YMove1

VoltageWave [0,size] = 1
OutWave4 [0,size] = 0
//just type in a test wave for voltage and 4th wave.

Error += td_writestring("arc.crosspoint.ina", "outa")
Error += td_writestring("arc.crosspoint.inb", "outb")
//setup crosspoint panel.
// !!! outa and output.A are different. I need to ask Mario to make it clear !!!

Error += td_xSetOutWavePair(0, "0", "PIDSLoop.0.Setpoint", XMove,"PIDSLoop.1.Setpoint",YMove, interpolatepoint)
//Pipe litho wave to DSP. First do this and then do engage is reasonable for litho. Make sure to let the interpolatepoint to
//be negative so it is linear rather than cubic spling.

Error += td_xSetOutWavePair(1, "0", "Output.A", VoltageWave, "Output.B", OutWave4, interpolatepoint)
//Setup another output wave pair: voltage wave and 4th wave. Output.A should hook to tip vltge. need to check about this later...

Error += td_xSetInWavePair(0, "0", "XSensor", XTrack, "YSensor", YTrack, "", interpolatepoint*(-1))
Error += td_xSetInWavePair(1, "0", "Input.A", VoltageTrack, "Input.B", Wave4Track, "", interpolatepoint*(-1))
//Important Notes!! For the input wave, wave length must be a multiple of 32 !!!

Error += ir_SetPISLoop(2, "Always,Never", "Fast%Input", LithoSetPoint, 0, 1000, 0, "Output.Z",-10,150)
//Tip engage for litho.
//NewPath/O WaveMonitor "E:Users:WaveMonitor:"
//Sleep/S 1
//Give time for tip engage

Error += td_WriteString("Event.0", "once")
//Triger litho.

Save/O/T/P=WaveMonitor XTrack as "XTrack.itx"
Save/O/T/P=WaveMonitor YTrack as "YTrack.itx"
Save/O/T/P=WaveMonitor VoltageTrack as "VoltageTrack.itx"
Save/O/T/P=WaveMonitor Wave4Track as "Wave4Track.itx"
Display YTrack XTrack
Display VoltageTrack Wave4Track
//Display VoltageTrack Wave4Track
//In order to see the trajectory of litho. but data are with Volt. unit. can be convert to um later.

if(Error)
    print "Error in execution", Error
endif

```


APPENDIX B

LOW TEMPERATURE AFM DESIGN AND UPGRADE FOR FUTURE

EXPERIMENTS

The low temperature AFM, having the functions of both cooling down the sample and scanning probe microscopy, is a powerful tool to explore the novel physics phenomenon.

For LAO/STO heterostructures, a variety of emergent properties are found at low temperature. For example, the electron mobility is found to be greatly enhanced as the temperature decreases. Below critical temperature ~ 200 mK, the interface becomes superconducting. The Shubnikov–de Haas effect is also reported for LAO/STO at low temperature. In addition, low temperature is also an important condition for many high performance sketched nanoelectronic devices, such as the sketched single electron transistor ($< \sim 30$ K), sketched nanowire cavities (~ 1 K) and sketched superlattice for quantum simulation (< 50 mK), etc. On the other hand, at low temperature, the thermal noise for an AFM tip is greatly suppressed, resulting in a higher resolution in piezoresponse force microscopy, scanning tunneling microscopy and magnetic force microscopy. Therefore, developing a low temperature AFM is important for the further study of LAO/STO.

B.1 INSTRUMENT HARDWARE DESIGN

The new system is designed based on a commercial vacuum AFM (JEOL SPM 5200). A pulse tube cryostation (Cryomech inc., PT410 model) with the cooling power 0.9 W at 4.2 K is integrated to the AFM to cool down the sample. Fig. B1 illustrates the newly designed cryogen-free cooling system with the vacuum AFM.

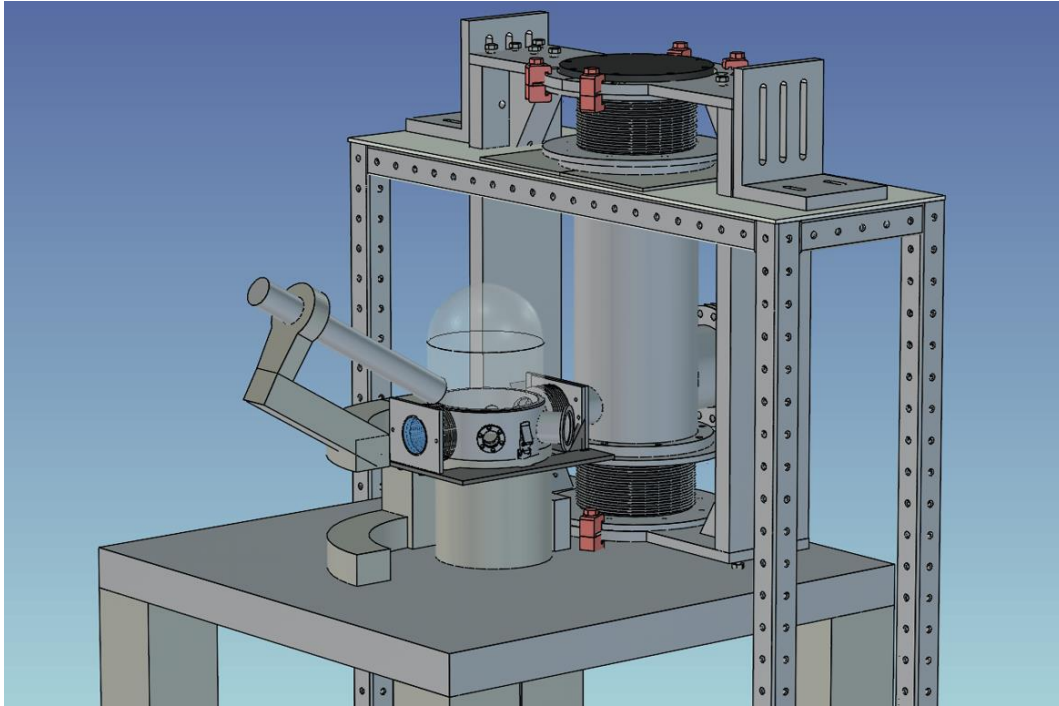


Fig. B1 3D design of the cooling system for the vacuum AFM.

Fig. B2 exhibits the details about the design. The pulse tube sits on the vacuum jacket (part # 2, in Fig. B2(a)). The two flexible bellows, connected by a rigid frame (part # 3, Fig. B2(a)), form a balance structure between the pulse tube and the vacuum jacket so that the vibrations generated by the pulse tube will be greatly reduced. The rigid frame is then anchored to the desk using two “L” shape brackets (part # 8, Fig. B2(a)). Notice that on the back of the vacuum jacket,

there is a 6 inch CF flange with a 32 pin Fisher electrical feed-through. Such CF flange is also reserved for the possible gas feed-through in the future.

Inside the vacuum jacket (Fig. B2(b)), a cylindrical shape radiation shield (part # 6, Fig. B2(b)) made of bronze is attached to the first cooling stage of the pulse tube cold head (31.5 W @ 45 K). There is also a radiation shield tube extended from the radiation shield cylinder to protect the cold finger from thermal radiation. Inside the radiation shield (Fig. B2(c)), a colder finger with the supporting plate is attached to the second cooling stage of the pulse tube cold head (0.9 W @ 4.2 K). Both of these two pieces are made of oxygen free high thermal conductivity (OFHC) copper.

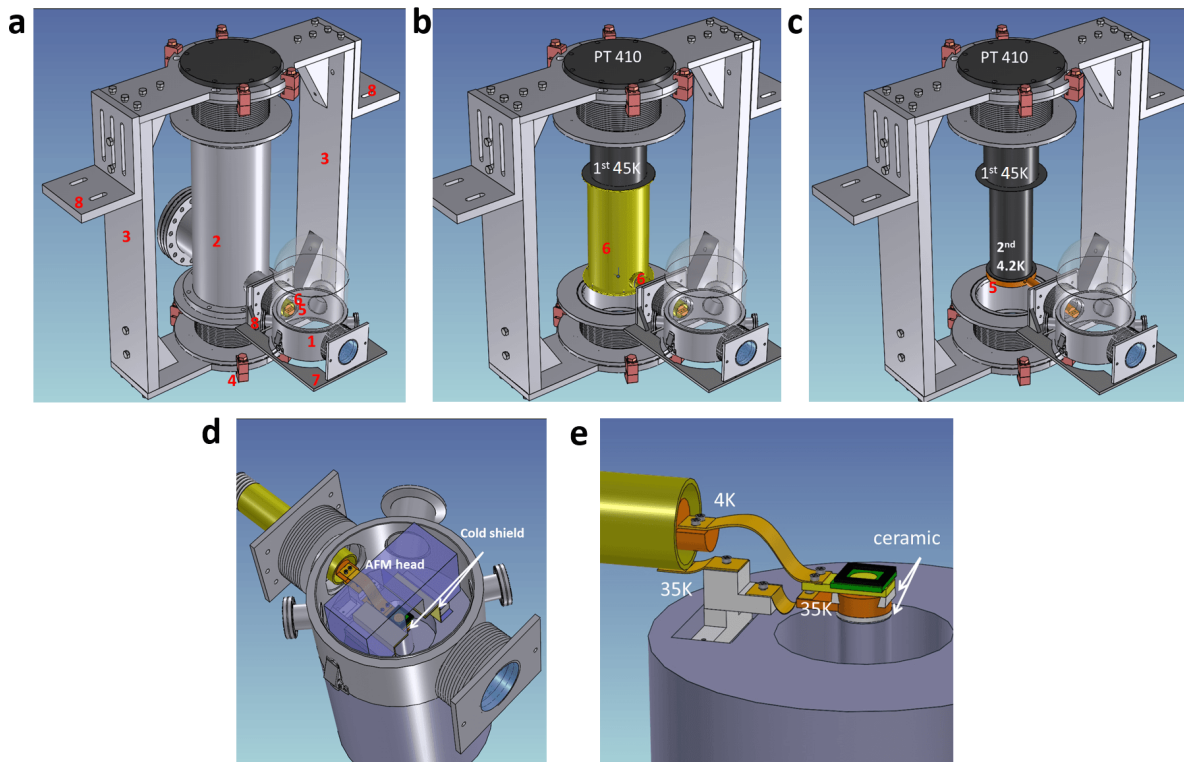


Fig. B2 Essential parts of designed system. (a), Designed pieces for the pulse tube and AFM. (b), Inside of the vacuum jacket, the radiation shield (yellow color) is attached to 1st cooling stage (31.5 W, 45K) of the pulse tube. (c), Inside of the radiation shield, the OFHC copper cold finger with supporting plate is attached to the 2nd stage (0.9 W, 4.2 K)

of the pulse tube. (d), Design of the pieces for AFM part, which including the AFM collar, cold shields, sample socket and thermal flexible connection. (e), The thermal link between cold finger and sample stage.

For the AFM part, the AFM collar is designed (Fig. B2(d)). On the AFM collar, there are two flexible bellows ($k = 28 \text{ N/cm}$) and three flange ports (2 KF flange and 1 CF flange for electrical feed through). The two bellows are connected by a rigid frame (part # 7 in Fig. B2(a)). There is also an optical window on the front bellow. The thermal link is shown in Fig. B2(e). A flexible thermal connection (annealed and Au coated) is made between the end of the cold finger and the sample stage. To reduce the thermal leak, the sample stage is isolated from the scanner by a ceramic piece.

The actual assembled system is shown in Fig. B3.



Fig. B3 Picture of assembled low temperature AFM system.

B.2 SYSTEM PERFORMANCE

The system performance is evaluated in three aspects: (1) vacuum level, (2) base temperature, (3) noise during AFM scanning. The vacuum pressure within the chamber is monitored by a wide range ion gauge. Fig. B4 shows the pressure log history when the system is pumped down by a mechanical pump and a turbo pump. The pressure within the chamber can reach $\sim 9 \times 10^{-6}$ Torr after pumping for 1 hour.

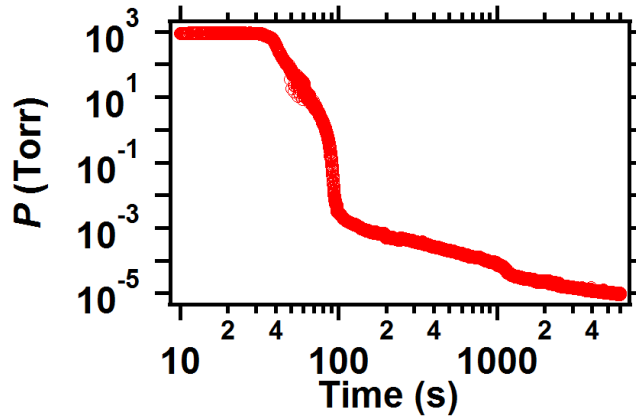


Fig. B4 System pressure during pumping down.

The cooling performance is evaluated by using a Si diode temperature sensor (Lakeshore, SD 670). Both the temperature at the end of the cold finger and the sample stage are recorded during the cool down process. Fig. B5 demonstrates that the base temperatures at the end of the cold finger and sample stage are ~ 7 K and ~ 10 K, respectively.

Both the pump and the pulse tube will generate periodic vibration during operation. To reduce the mechanical coupling between the cooling system and the AFM, the balance bellows

design (Fig. B2(a)) is used. To evaluate the AFM noise during operation, we performed the AFM imaging in contact mode on a reference grating under different conditions.

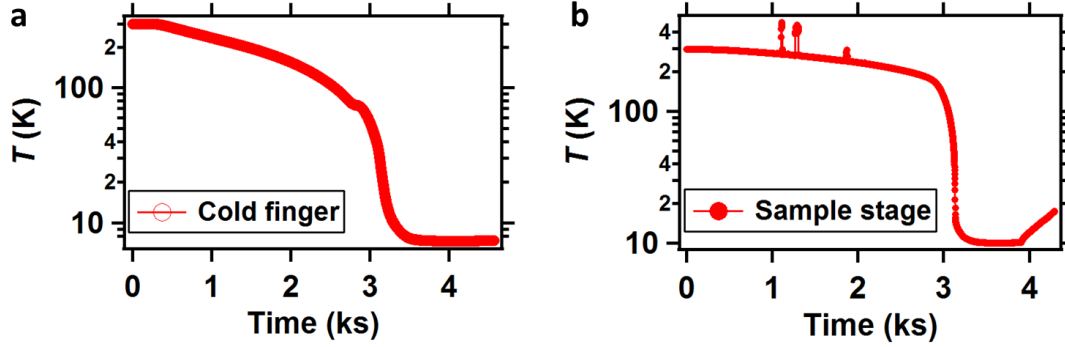


Fig. B5 System cool down history. (a), the temperature history at the end of cold finger during cool down process. (b), the temperature history on the sample stage during the cool down and warm up (after $t = 4000$ s).

Fig. B6(a-c) show the AFM height images under (a) room temperature at 1 atm, (b) room temperature at 2×10^{-4} Torr and (c) 10 K at 1×10^{-5} Torr. No obvious periodic noise is found in these AFM images. The AFM retrace data for (b) and (c) are shown as

Fig. B6(d) and (e), which suggests the noise is below 1 nm.

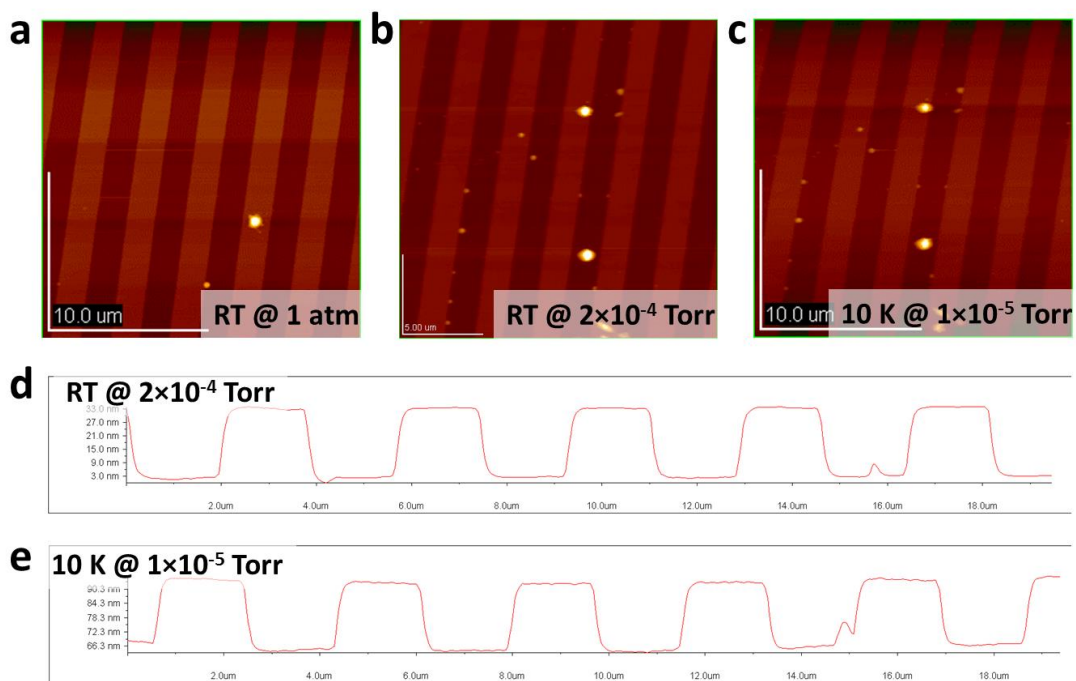


Fig. B6 AFM height image of a grating sample in ambient air at room temperature. (a), in vacuum 2×10^{-4} Torr at room temperature (b) and in vacuum 1×10^{-5} at 10 K (c). (d) and (e) show the cross section height profile of image (b) and (c) respectively.

APPENDIX C

MAGNETIC FORCE MICROSCOPY USING CYPHER AFM

This section documents the regular routines applied during the MFM experiments ([Section 5.0](#)).

C.1 MFM TIP CHARACTERIZATION

The tip is manufactured by Asylum Research (Model: ASYMFM) with 50 nm CoCr coating, 400 Oe coercive field and a total magnetization 10^{-13} emu. The mechanical properties of the cantilever, such as the spring constant and resonant frequency, are obtained by performing thermal spectroscopy. During this measurement, the AFM monitors the cantilever's deflection fluctuation as a function of time. Based on the time-domain measurement, the AFM extracts the power spectral density (PSD), which is shown in [Fig. C1](#). The cantilever's thermal noise response with respect to frequency is then fitted to a simple harmonic oscillator equation [Eq. \(2-11\)](#), from which we obtain the spring constant $k = 1.2$ N/m and quality factor $Q = 136$.

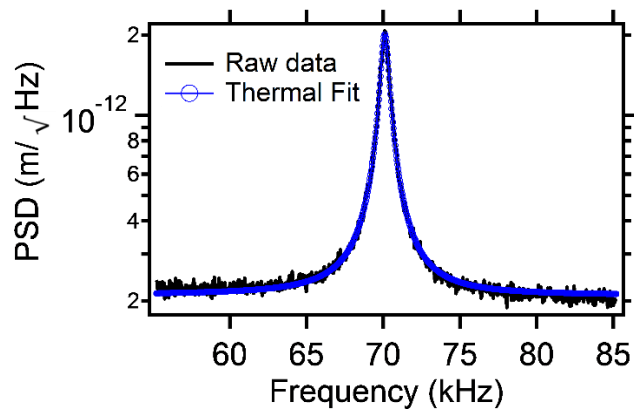


Fig. C1 Thermal spectroscopy of the MFM cantilever.

C.2 MFM TIP MAGNETIZATION

The MFM tip is magnetized using an electromagnet shown in [Fig. C2](#), which can apply a uniform magnetic field up to 2000 Oe. During the magnetization, tip is placed in the gel box at the middle of two electromagnets. By rotating the tip holder, the tip can be magnetized horizontally or vertically.

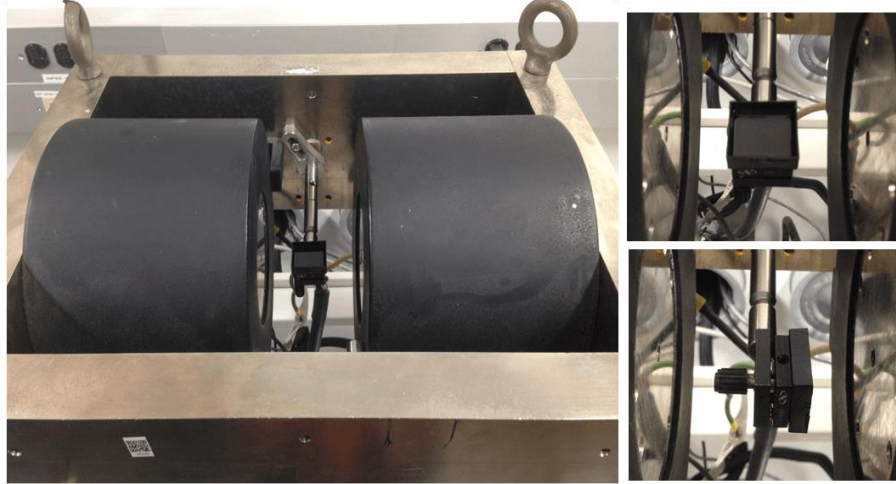


Fig. C2 Electromagnets system used to magnetize the AFM tip

C.3 TIP MAGNETIZATION ORIENTATION VALIDATION

To verify that the tip is properly magnetized, MFM measurements are performed on a commercially available (Bruker, model “MFMSAMPLE”) test sample with periodic in-plane magnetic domain structures and out-of-plane domain walls. During the MFM imaging, the tip-surface distance Δh is kept at 50 nm. With the tip vertically magnetized, MFM images are acquired with the sample rotated clockwise 0° and 37° (Fig. C3(a-b)). Since the tip magnetization is perpendicular to the sample, Fig. C3(a-b) should show the same contrast, independent of the angle. A quantitative analysis of the averaged section profiles perpendicular to the domain wall is demonstrated in Fig. C3(c) to show good agreement with the expected result.

The horizontal tip magnetization is checked using a similar method. Based on Eq. (2-14)

$$\Delta f \propto m \cdot \frac{\partial B}{\partial z} \cdot \cos \theta \quad (\text{C-1})$$

where θ is the angle between the tip and the sample's magnetization orientation. Changing the relative angle between sample and tip will change the magnetic signal. Fig. C3(d-e) are MFM images with sample rotated. The angle between the tip and the sample's magnetization in Fig. C3(d-e) is $\theta_d = 15^\circ$ and $\theta_e = 63^\circ$, respectively. Fig. C3(e) shows a significantly lower signal than Fig. C3(d), which is also directly displayed in Fig. C3(f). The magnetic signal contrast: ΔF_d and ΔF_e in Fig. C3(d) and Fig. C3(e) can be simply defined as the averaged difference between peaks and values of the curves in Fig. C3(f). With $\Delta F_d = 16.8$ Hz and $\Delta F_e = 7.3$ Hz, then

$$\frac{\Delta F_d}{\Delta F_e} = \frac{16.8}{7.3} = 2.3 \quad (\text{C-2})$$

On the other hand, for the tip with horizontal magnetization, theoretic calculation from Eq. (C-1) gives

$$\frac{\Delta f_d}{\Delta f_e} = \frac{\cos \theta_d}{\cos \theta_e} = \frac{\cos 15^\circ}{\cos 63^\circ} = 2.1 \quad (\text{C-3})$$

Considering $\frac{\Delta F_d}{\Delta F_e} \approx \frac{\Delta f_d}{\Delta f_e}$, we claim the tip is properly magnetized in plane.

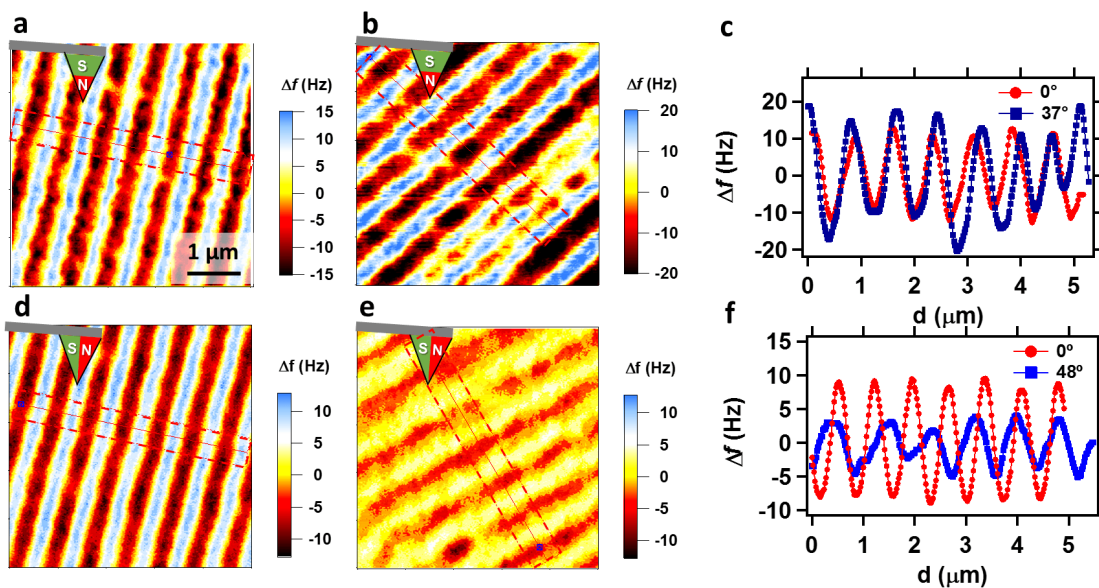


Fig. C3 MFM images on reference sample. (a-b) MFM images are obtained with reference sample rotated clockwise at 0° and 37° respectively. Tip is magnetized vertically as indicated in the figure. (c) Averaged section profile along the red lines in (a) and (b). (d-e) Tip is magnetized horizontally. MFM images are obtained with sample rotated clockwise at 0° and 48° respectively. (f) Averaged section profile along the red lines in (d) and (e).

C.4 MFM SCANNING ENVIRONMENT

[Fig. C4](#) illustrates the scanning environment in a commercial AFM. There is a magnetic holder (blue) directly attached to the scanner. The sample is loaded in a chip carrier on a printed circuit board (grey). A circular steel specimen disc is glued to the bottom of the PC board (dark grey). The magnetic force between the steel disc and magnetic holder ensures that the sample sticks to the scanner during the scanning. Using a magnetic sensor, the measured magnetic field on the sample surface is: $B_z = 1.1$ Gauss, $B_x = 1.8$ Gauss, $B_y = 0.8$ Gauss. This static magnetic field (which includes the Earth's contribution) exists during all of the experiments described. For [Fig. C5](#), the sample rotates with the steel disc, while the magnetic holder remains fixed in place.

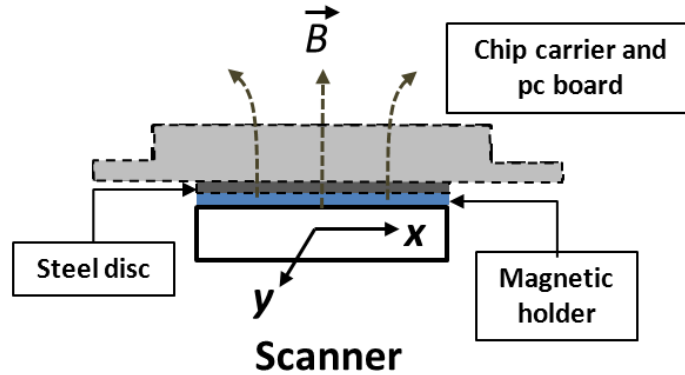


Fig. C4 Schematic showing the AFM scanning environment. There is a weak (~ 1 Oe) magnetic field from the magnetic holder.

C.5 MFM WITH VARIOUS RELATIVE ANGLES BETWEEN THE TIP MAGNETIZATION AND THE SAMPLE ORIENTATION

As discussed in Appendix C3, when the relative angle between the tip and the sample is changed, the MFM images contrast will change accordingly. Here we magnetize the tip horizontally and perform the MFM measurements with the sample rotated. Such experiments can help to identify the orientation of the magnetic domains.

A series of MFM images is shown in [Fig. C5](#) at $V_{dc} = -1$ V, where the relative angle θ between the MFM tip and the sample is varied. The tip magnetization is fixed along the y direction and the sample is rotated clockwise with various angles ranging from 0° to 42° . The MFM amplitude contrast is largest at $\theta = 0^\circ$. As the sample rotates, the stripe-shaped feature rotates by approximately the same angle; however, the magnitude of the signal decreases. At $\theta = 42^\circ$, the

stripe-shaped features vanish, resulting in a spatially uniform signal over the measured area. The results indicate the sample's magnetization resides in-plane.

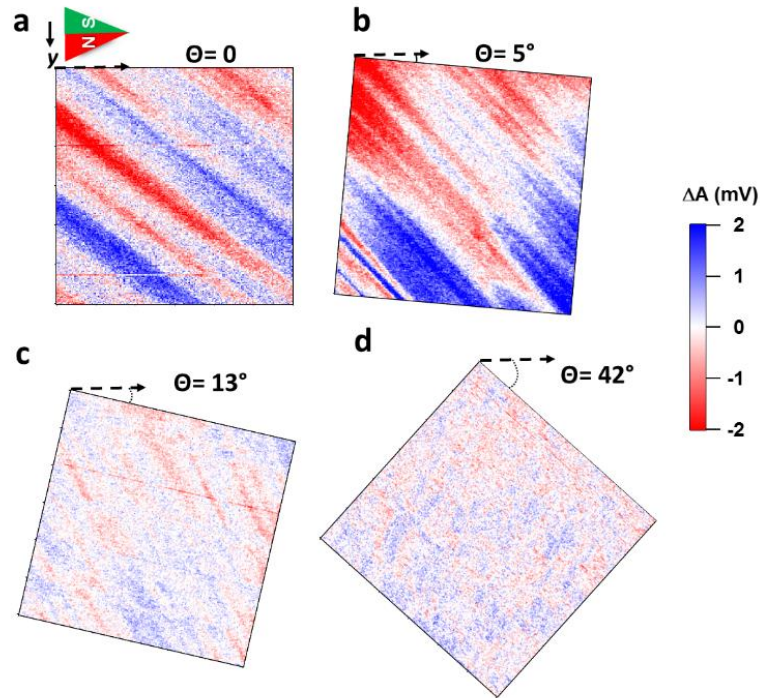


Fig. C5 MFM images ($3 \mu\text{m} \times 3 \mu\text{m}$) acquired for various relative angles between the tip magnetization and the sample orientation. The slope detection method is applied with the cantilever driven at a fixed frequency 67 kHz slightly off resonance. The tip magnetization direction is kept unchanged while the sample is rotated clockwise with angle 0° (a), 5° (b), 13° (c), 42° (d).

The MFM experiments are also performed with the tip magnetization orientation reversed, which is equivalent to changing the relative angle between the MFM tip and the sample by 180° . Here the results are presented for Device A with $V_{\text{dc}} = -1 \text{ V}$. The surface profile of the investigated area is shown in Fig. C6(a) and the tip is magnetized horizontally. The obtained MFM image (Fig. C6(b)) displays clear magnetic contrast. Then the tip is remagnetized with the magnetization flipped. By using the green circled topographic features (Fig. C6(c)) as markers, we perform the

MFM image over the same area. The results show the magnetic contrast is reversed, which further demonstrates that the sample magnetization is in-plane.

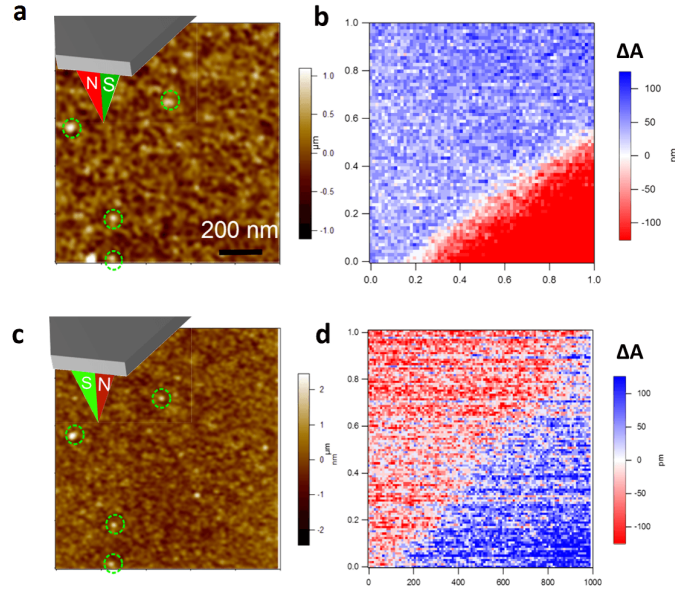


Fig. C6 MFM image over the same area on the top electrode of Device A with tip magnetization reversed. (a,c), surface topography over the investigated $1 \mu\text{m} \times 1 \mu\text{m}$ area before and after the tip remagnetization. The green circled topographic features serve as natural alignment marks. (c,d), MFM image before and after the tip magnetization is flipped. These images clearly show that the magnetic contrast also reversed.

C.6 SUPPLEMENTAL MFM EXPERIMENTS DATA

In Section 5.5, the main results are presented for Device A. Here I include the experiment results for other devices (Device B, C in [Fig. 5-1\(d,e\)](#)).

MFM experiments were performed on the top gate of Devices B and C, respectively ([Fig. C7](#)). Both [Fig. C7 \(b\)](#) and [\(e\)](#) show the same characteristic stripe domains under low carrier

density, similar to results observed in Device A in Section 5.5. At the same time, (c) and (f) show significantly diminished contrast for $V_{dc} = 1$ V bias. The results agree qualitatively with the observations for Device A.

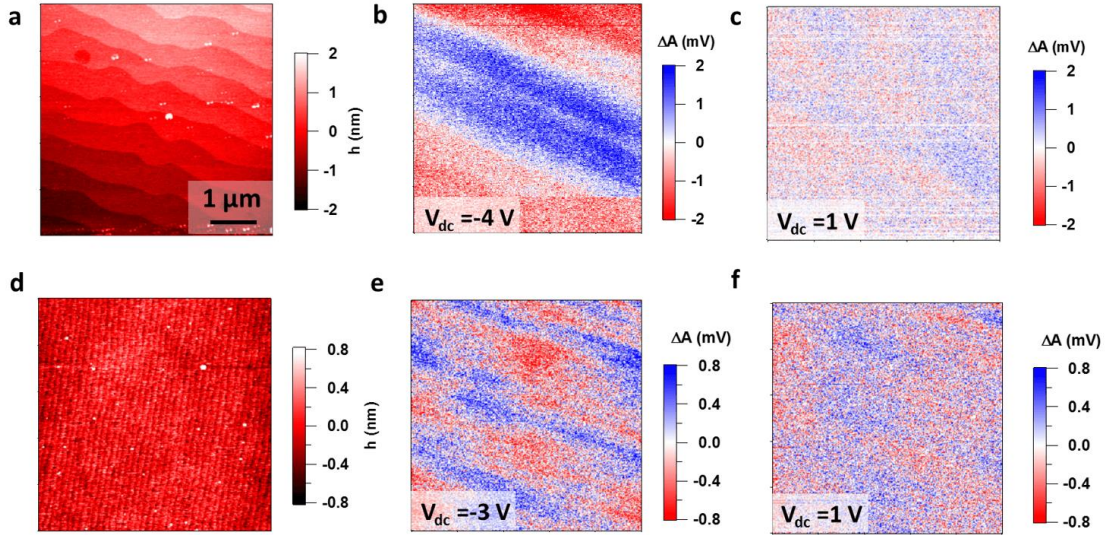


Fig. C7 MFM on exposed LAO surface close to the top electrode for Devices B and C. The image size is 5 μm . (a) Surface morphology of investigated area on Device B. (b, c) MFM amplitude images under $V_{dc} = -4$ V and 1 V, respectively, on Device B. (d) Surface morphology of investigated area on Device C. (e, f) MFM amplitude images under $V_{dc} = -3$ V and 1 V, respectively, on Device C.

The MeFM data shown in Section 5.5 is performed on LAO close to the top gate for Device A. Here I will show the same MeFM experiments on the top electrode for Device A. Fig. C8 is performed on location A in Fig. 5-1 and Fig. C9 is performed on location E in Fig. 5-1. The results agree qualitatively with the observations in Fig. 5-8.

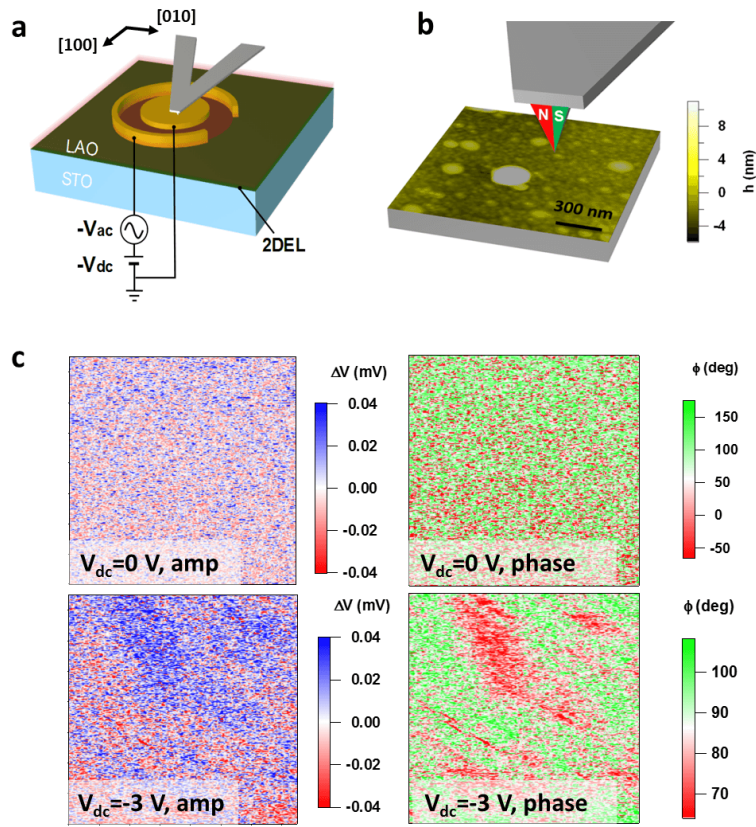


Fig. C8 MeFM scanning above top electrode on Device A. (a) Sketch of experiment setup. The combined ac and dc voltage is applied to the interface with $V_{ac} = 0.14$ V at $f = 70.6$ kHz and V_{dc} held at various fixed values. The separation between the tip and top electrode is 20 nm. (b) The surface height image over $1.4 \times 1.4 \mu\text{m}^2$ square. (c) MeFM amplitude and phase images with $V_{dc} = 0$ V and -3V.

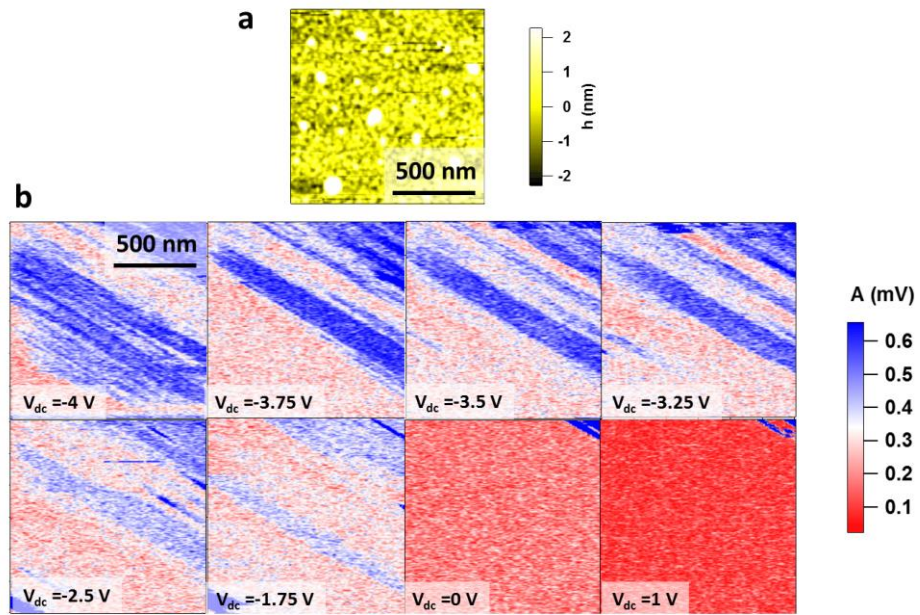


Fig. C9 MeFM scanning over another $1.2 \times 1.2 \mu\text{m}^2$ square on Device A. (a), The surface height image. (b), A sequence of MeFM amplitude images as V_{dc} increases from -4 V to 1 V.

APPENDIX D

2-AXIS IN-PLANE MAGNETIC FIELD GENERATOR MODULE FOR CYPHER AFM

A 2-axis in-plane magnetic field generator is designed and machined for the Cypher AFM. [Fig. D1\(a\)](#) shows the 3D CAD design of such magnetic field generator module on the AFM. The key parts are two “U” shaped electromagnets, which are colored with red and blue. These two electromagnets will generate a localized magnetic field through the sample. [Fig. D1\(b\)](#) shows the machined pieces of the module. The “U” shaped electromagnets are made of soft iron. The number of turns is $N_r = 580$ and $N_b = 400$ for the red and blue electromagnets, respectively. The assembled module added on to the AFM is shown in [Fig. D1\(c\)](#). The performance of this module is measured using a Gauss meter ([Fig. D1\(d\)](#)). By changing the source voltage to the electromagnets, a controllable magnetic field range from ~ -220 Gauss to ~ 220 Gauss is achieved in both the x and y in-plane direction.

This 2-axis in-plane magnetic field generator module will be used for further investigation of electronically controlled ferromagnetism of LAO/STO. The MFM experiments will be performed on top-gated LAO/STO under external \mathbf{B} field, from which the coercive field of LAO/STO magnetization is expected to be obtained.

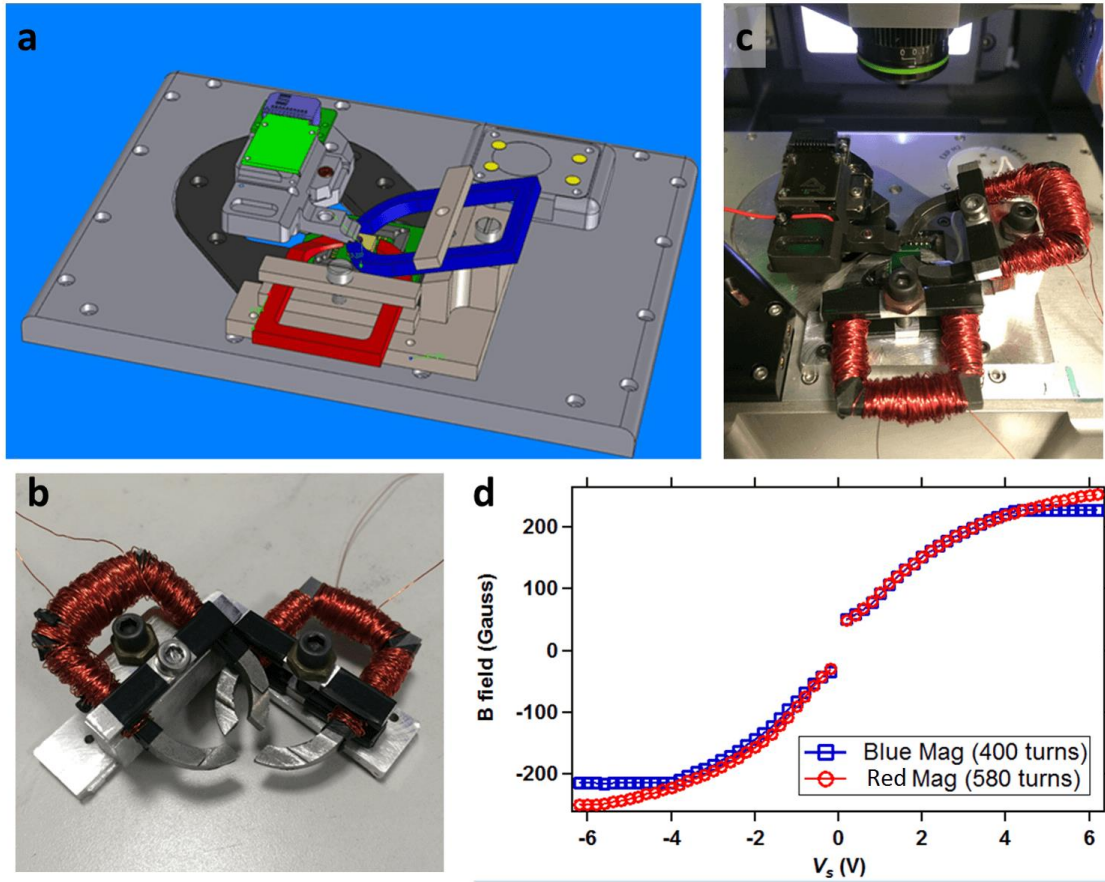


Fig. D1 2-axis in-plane magnetic field generator module for Cypher AFM. (a), 3D CAD design of the 2-axis electromagnets. (b), Machined electromagnets. (c), Assembled magnetic field generator module in Cypher AFM. The generated in-plane field will be localized near the sample. (d), Generated magnetic field as a function of power source voltage. The red and blue curve correspond to the red and blue electromagnets in (a).

BIBLIOGRAPHY

- 1 Ohtomo, A. & Hwang, H. Y. A high-mobility electron gas at the LaAlO₃/SrTiO₃ heterointerface. *Nature* **427**, 423-426, (2004).
- 2 Liao, Y. C., Kopp, T., Richter, C., Rosch, A. & Mannhart, J. Metal-insulator transition of the LaAlO₃-SrTiO₃ interface electron system. *Phys Rev B* **83**, 075402, (2011).
- 3 Irvin, P. *et al.* Anomalous High Mobility in LaAlO₃/SrTiO₃ Nanowires. *Nano Lett* **13**, 364-368, (2013).
- 4 Herranz, G., Sanchez, F., Dix, N., Scigaj, M. & Fontcuberta, J. High mobility conduction at (110) and (111) LaAlO₃/SrTiO₃ interfaces. *Sci Rep-Uk* **2**, 758, (2012).
- 5 Smith, H. M. & Turner, A. F. Vacuum Deposited Thin Films Using a Ruby Laser. *Appl Optics* **4**, 147, (1965).
- 6 A. Y. Cho, J. R. A. Molecular beam epitaxy. *Progress in Solid State Chemistry* **10**, 157-191, (1975).
- 7 El Kazzi, M. *et al.* Photoemission (XPS and XPD) study of epitaxial LaAlO₃ film grown on SrTiO₃(001). *Mat Sci Semicon Proc* **9**, 954-958, (2006).
- 8 Podkaminer, J. P. *et al.* Creation of a two-dimensional electron gas and conductivity switching of nanowires at the LaAlO₃/SrTiO₃ interface grown by 90 degrees off-axis sputtering. *Appl Phys Lett* **103**, 071604, (2013).
- 9 Sbrockey, N. M. *et al.* LaAlO₃/SrTiO₃ Epitaxial Heterostructures by Atomic Layer Deposition. *J Electron Mater* **41**, 819-823, (2012).
- 10 Siemons, W. *et al.* Origin of charge density at LaAlO₃ on SrTiO₃ heterointerfaces: Possibility of intrinsic doping. *Phys Rev Lett* **98**, 196802, (2007).
- 11 Kalabukhov, A. *et al.* Effect of oxygen vacancies in the SrTiO₃ substrate on the electrical properties of the LaAlO₃/SrTiO₃ interface. *Phys Rev B* **75**, 121404, (2007).
- 12 Thiel, S., Hammerl, G., Schmehl, A., Schneider, C. W. & Mannhart, J. Tunable quasi-two-dimensional electron gases in oxide heterostructures. *Science* **313**, 1942-1945, (2006).
- 13 Warusawithana, M. P. *et al.* LaAlO₃ stoichiometry is key to electron liquid formation at LaAlO₃/SrTiO₃ interfaces. *Nature Communications* **4**, 2351, (2013).
- 14 Qiao, L., Droubay, T. C., Kaspar, T. C., Sushko, P. V. & Chambers, S. A. Cation mixing, band offsets and electric fields at LaAlO₃/SrTiO₃(001) heterojunctions with variable La:Al atom ratio. *Surf Sci* **605**, 1381-1387, (2011).
- 15 Nakagawa, N., Hwang, H. Y. & Muller, D. A. Why some interfaces cannot be sharp. *Nat Mater* **5**, 204-209, (2006).
- 16 Willmott, P. R. *et al.* Structural basis for the conducting interface between LaAlO₃ and SrTiO₃. *Phys Rev Lett* **99**, 155502, (2007).
- 17 Sulpizio, J. A., Shahal Ilani, Patrick Irvin, and Jeremy Levy. Nanoscale Phenomena in Oxide Heterostructures. *Annu. Rev. Mater. Res.* **44**, 117-149, (2014).
- 18 Ben Shalom, M., Sachs, M., Rakhmilevitch, D., Palevski, A. & Dagan, Y. Tuning Spin-Orbit Coupling and Superconductivity at the SrTiO₃/LaAlO₃ Interface: A Magnetotransport Study. *Phys Rev Lett* **104**, 126802, (2010).

- 19 Caviglia, A. D. *et al.* Tunable Rashba Spin-Orbit Interaction at Oxide Interfaces. *Phys Rev Lett* **104**, 126803, (2010).
- 20 Reyren, N. *et al.* Superconducting interfaces between insulating oxides. *Science* **317**, 1196-1199, (2007).
- 21 Caviglia, A. D. *et al.* Electric field control of the LaAlO₃/SrTiO₃ interface ground state. *Nature* **456**, 624-627, (2008).
- 22 Koga, T., Nitta, J., Akazaki, T. & Takayanagi, H. Rashba spin-orbit coupling probed by the weak antilocalization analysis in InAlAs/InGaAs/InAlAs quantum wells as a function of quantum well asymmetry. *Phys Rev Lett* **89**, 046801, (2002).
- 23 Brinkman, A. *et al.* Magnetic effects at the interface between non-magnetic oxides. *Nat Mater* **6**, 493-496, (2007).
- 24 Ariando *et al.* Electronic phase separation at the LaAlO₃/SrTiO₃ interface. *Nature Communications* **2**, 188, (2011).
- 25 Bert, J. A. *et al.* Direct imaging of the coexistence of ferromagnetism and superconductivity at the LaAlO₃/SrTiO₃ interface. *Nat Phys* **7**, 767-771, (2011).
- 26 Li, L., Richter, C., Mannhart, J. & Ashoori, R. C. Coexistence of magnetic order and two-dimensional superconductivity at LaAlO₃/SrTiO₃ interfaces. *Nat Phys* **7**, 762-766, (2011).
- 27 Lee, J. S. *et al.* Titanium d_{xy} ferromagnetism at the LaAlO₃/SrTiO₃ interface. *Nat Mater* **12**, 703-706, (2013).
- 28 Dikin, D. A. *et al.* Coexistence of Superconductivity and Ferromagnetism in Two Dimensions. *Phys Rev Lett* **107**, 056802, (2011).
- 29 Klinov, D. & Magonov, S. True molecular resolution in tapping-mode atomic force microscopy with high-resolution probes. *Appl Phys Lett* **84**, 2697-2699, (2004).
- 30 Lauritsen, J. V. & Reichling, M. Atomic resolution non-contact atomic force microscopy of clean metal oxide surfaces. *J Phys-Condens Mat* **22**, 263001, (2010).
- 31 Binnig, G. K. Atomic-Force Microscopy. *Phys Scripta* **T19a**, 53-54, (1987).
- 32 Kenton, B. J., Fleming, A. J. & Leang, K. K. Compact ultra-fast vertical nanopositioner for improving scanning probe microscope scan speed. *Rev Sci Instrum* **82**, 123703, (2011).
- 33 Huo, F. W. *et al.* Polymer pen lithography. *Science* **321**, 1658-1660, (2008).
- 34 Geng, Y. N. *et al.* Direct visualization of magnetoelectric domains. *Nat Mater* **13**, 163-167, (2014).
- 35 Cen, C. *et al.* Nanoscale control of an interfacial metal-insulator transition at room temperature. *Nat Mater* **7**, 298-302, (2008).
- 36 Xie, Y. W., Bell, C., Yajima, T., Hikita, Y. & Hwang, H. Y. Charge Writing at the LaAlO₃/SrTiO₃ Surface. *Nano Lett* **10**, 2588-2591, (2010).
- 37 Huang, M. C. *et al.* Direct imaging of LaAlO₃/SrTiO₃ nanostructures using piezoresponse force microscopy. *Apl Mater* **1**, 052110, (2013).
- 38 Cen, C., Thiel, S., Mannhart, J. & Levy, J. Oxide Nanoelectronics on Demand. *Science* **323**, 1026-1030, (2009).
- 39 Irvin, P. *et al.* Rewritable nanoscale oxide photodetector. *Nat Photonics* **4**, 849-852, (2010).
- 40 Bogorin, D. F. *et al.* Nanoscale rectification at the LaAlO₃/SrTiO₃ interface. *Appl Phys Lett* **97**, 013102, (2010).
- 41 Cheng, G. L. *et al.* Sketched oxide single-electron transistor. *Nature Nanotechnology* **6**, 343-347, (2011).
- 42 Hellberg, C. S. *American Physical Society*, (2009).

- 43 Xie, Y., Bell, C., Yajima, T., Hikita, Y. & Hwang, H. Y. Charge Writing at the LaAlO₃/SrTiO₃ Surface. *Nano Lett* **10**, 2588-2591, (2010).
- 44 Herranz, G. *et al.* High Mobility in LaAlO₃/SrTiO₃ Heterostructures: Origin, Dimensionality, and Perspectives. *Phys Rev Lett* **98**, 216803, (2007).
- 45 Popovic, Z. S., Satpathy, S. & Martin, R. M. Origin of the Two-Dimensional Electron Gas Carrier Density at the LaAlO₃ on SrTiO₃ Interface. *Phys Rev Lett* **101**, 256801, (2008).
- 46 Yoshimatsu, K., Yasuhara, R., Kumigashira, H. & Oshima, M. Origin of metallic states at the heterointerface between the band insulators LaAlO₃ and SrTiO₃. *Phys Rev Lett* **101**, 026802, (2008).
- 47 Pavlenko, N. & Kopp, T. Structural relaxation and metal-insulator transition at the interface between SrTiO₃ and LaAlO₃. *arXiv:0901.4610v4*, (2009).
- 48 Schwingschlogl, U. & Schuster, C. Surface effects on oxide heterostructures. *Epl* **81**, 17007, (2008).
- 49 Rijnders, G. J. H. M., Koster, G., Blank, D. H. A. & Rogalla, H. In situ monitoring during pulsed laser deposition of complex oxides using reflection high energy electron diffraction under high oxygen pressure. *Appl Phys Lett* **70**, 1888-1890, (1997).
- 50 Mannhart, J. & Schlom, D. G. Oxide interfaces—an opportunity for electronics. *Science* **327**, 1607-1611, (2010).
- 51 Li, L. *et al.* Very Large Capacitance Enhancement in a Two-Dimensional Electron System. *Science* **332**, 825-828, (2011).
- 52 Jany, R. *et al.* Diodes with breakdown voltages enhanced by the metal-insulator transition of LaAlO₃-SrTiO₃ interfaces. *Appl Phys Lett* **96**, 183504, (2010).
- 53 Forg, B., Richter, C. & Mannhart, J. Field-effect devices utilizing LaAlO₃-SrTiO₃ interfaces. *Appl Phys Lett* **100**, 8023, (2012).
- 54 Singh-Bhalla, G. *et al.* Built-in and induced polarization across LaAlO₃/SrTiO₃ heterojunctions. *Nat Phys* **7**, 80-86, (2011).
- 55 Bark, C. W. *et al.* Switchable Induced Polarization in LaAlO₃/SrTiO₃ Heterostructures. *Nano Lett* **12**, 1765-1771, (2012).
- 56 Soergel, E. Piezoresponse force microscopy (PFM). *J Phys D Appl Phys* **44**, 464003, (2011).
- 57 Eliseev, E. A., Kalinin, S. V., Jesse, S., Bravina, S. L. & Morozovska, A. N. Electromechanical detection in scanning probe microscopy: Tip models and materials contrast. *J Appl Phys* **102**, 014109, (2007).
- 58 Zhao, M. H., Wang, Z. L. & Mao, S. X. Piezoelectric characterization of individual zinc oxide nanobelt probed by piezoresponse force microscope. *Nano Lett* **4**, 587-590, (2004).
- 59 Agronin, A. G., Rosenwaks, Y. & Rosenman, G. I. Piezoelectric coefficient measurements in ferroelectric single crystals using high voltage atomic force microscopy. *Nano Lett* **3**, 169-171, (2003).
- 60 Seri, S. & Klein, L. Antisymmetric magnetoresistance of the SrTiO₃/LaAlO₃ interface. *Phys Rev B* **80**, 180410, (2009).
- 61 Maurice, J. L. *et al.* Electronic conductivity and structural distortion at the interface between insulators SrTiO₃ and LaAlO₃. *Physica Status Solidi a-Applications and Materials Science* **203**, 2209-2214, (2006).
- 62 Willmott, P. R. *et al.* Structural Basis for the Conducting Interface between LaAlO₃ and SrTiO₃. *Phys Rev Lett* **99**, 155502, (2007).

- 63 Pentcheva, R. & Pickett, W. E. Avoiding the Polarization Catastrophe in LaAlO₃
64 Overlayers on SrTiO₃(001) through Polar Distortion. *Phys Rev Lett* **102**, 107602, (2009).
- 64 Rodriguez, B. J., Callahan, C., Kalinin, S. V. & Proksch, R. Dual-frequency resonance-
65 tracking atomic force microscopy. *Nanotechnology* **18**, 475504, (2007).
- 65 Jiang, W. *et al.* Mobility of oxygen vacancy in SrTiO₃ and its implications for oxygen-
66 migration-based resistance switching. *J Appl Phys* **110**, 034509, (2011).
- 66 Huang, M. C. *et al.* Non-local piezoresponse of LaAlO₃/SrTiO₃ heterostructures. *Appl Phys
Lett* **104**, 161606, (2014).
- 67 Jahn, H. A. & Teller, E. *Proc. R. Soc. (London)* **161**, 220, (1937).
- 68 Park, M. S., Rhim, S. H. & Freeman, A. J. Charge compensation and mixed valency in
LaAlO₃/SrTiO₃ heterointerfaces studied by the FLAPW method. *Phys Rev B* **74**, 205416,
(2006).
- 69 Vonk, V. *et al.* Interface structure of SrTiO₃/LaAlO₃ at elevated temperatures studied in
situ by synchrotron x rays. *Phys Rev B* **75**, 235417, (2007).
- 70 Haeni, J. H. *et al.* Room-temperature ferroelectricity in strained SrTiO₃. *Nature* **430**, 758-
761, (2004).
- 71 Zubko, P., Catalan, G., Buckley, A., Welche, P. R. L. & Scott, J. F. Strain-Gradient-
Induced Polarization in SrTiO₃ Single Crystals. *Phys Rev Lett* **99**, 167601, (2007).
- 72 Popok, V. N. *et al.* Kelvin Probe Force Microscopy Study of LaAlO₃/SrTiO₃
Heterointerfaces. *Journal of Advanced Microscopy Research* **5**, 26-30, (2010).
- 73 Kalabukhov, A. S. *et al.* Cationic Disorder and Phase Segregation in LaAlO₃/SrTiO₃
Heterointerfaces Evidenced by Medium-Energy Ion Spectroscopy. *Phys Rev Lett* **103**,
146101, (2009).
- 74 Song, Y., Noh, T. W., Lee, S. I. & Gaines, J. R. Experimental-Study of the 3-Dimensional
Ac Conductivity and Dielectric-Constant of a Conductor-Insulator Composite near the
Percolation-Threshold. *Phys Rev B* **33**, 904-908, (1986).
- 75 Wolf, S. A. *et al.* Spintronics: A spin-based electronics vision for the future. *Science* **294**,
1488-1495, (2001).
- 76 Awschalom, D. D. & Flatte, M. E. Challenges for semiconductor spintronics. *Nat Phys* **3**,
153-159, (2007).
- 77 Dietl, T. A ten-year perspective on dilute magnetic semiconductors and oxides. *Nat Mater*
9, 965-974, (2010).
- 78 Ohno, H. *et al.* (Ga,Mn)As: A new diluted magnetic semiconductor based on GaAs. *Appl
Phys Lett* **69**, 363-365, (1996).
- 79 He, X. *et al.* Robust isothermal electric control of exchange bias at room temperature. *Nat
Mater* **9**, 579-585, (2010).
- 80 Dagotto, E. & Tokura, Y. Strongly Correlated Electronic Materials: Present and Future.
Mrs Bull **33**, 1037-1045, (2008).
- 81 Fitzsimmons, M. R. *et al.* Upper Limit to Magnetism in LaAlO₃/SrTiO₃ Heterostructures.
Phys Rev Lett **107**, 217201, (2011).
- 82 Salman, Z. *et al.* Nature of Weak Magnetism in SrTiO₃/LaAlO₃ Multilayers. *Phys Rev Lett*
109, 257207, (2012).
- 83 Joshua, A., Pecker, S., Ruhman, J., Altman, E. & Ilani, S. A universal critical density
underlying the physics of electrons at the LaAlO₃/SrTiO₃ interface. *Nature
Communications* **3**, 1129, (2012).

- 84 Joshua, A., Ruhman, J., Pecker, S., Altman, E. & Ilani, S. Gate-tunable polarized phase of
two-dimensional electrons at the LaAlO₃/SrTiO₃ interface. *PNAS* **110**, 9633, (2013).
- 85 Xie, Y., Hikita, Y., Bell, C. & Hwang, H. Y. Control of electronic conduction at an oxide
heterointerface using surface polar adsorbates. *Nature Communications* **2**, 494, (2011).
- 86 Martin, Y. & Wickramasinghe, H. K. Magnetic Imaging by Force Microscopy with 1000-
a Resolution. *Appl Phys Lett* **50**, 1455-1457, (1987).
- 87 Kebe, T. & Carl, A. Calibration of magnetic force microscopy tips by using nanoscale
current-carrying parallel wires. *J Appl Phys* **95**, 775-792, (2004).
- 88 Liu, C. X. *et al.* Calibration of magnetic force microscopy using micron size straight
current wires. *J Appl Phys* **91**, 8849-8851, (2002).
- 89 Albrecht, T. R., Grutter, P., Horne, D. & Rugar, D. Frequency-Modulation Detection Using
High-Q Cantilevers for Enhanced Force Microscope Sensitivity. *J Appl Phys* **69**, 668-673,
(1991).
- 90 Chui, S. T. Spin reversal in ultra-thin magnetic films with fourfold anisotropy. *Appl Phys
Lett* **68**, 3641-3643, (1996).
- 91 Elfimov, I. S., Yunoki, S. & Sawatzky, G. A. Possible Path to a New Class of
Ferromagnetic and Half-Metallic Ferromagnetic Materials. *Phys Rev Lett* **89**, 216403,
(2002).
- 92 Fidkowski, L., Jiang, H.-C., Lutchyn, R. M. & Nayak, C. Magnetic and superconducting
ordering in one-dimensional nanostructures at the LaAlO₃/SrTiO₃ interface. *Phys Rev B*
87, 014436, (2013).
- 93 Banerjee, S., Erten, O. & Randeria, M. Ferromagnetic exchange, spin-orbit coupling and
spiral magnetism at the LaAlO₃/SrTiO₃ interface. *Nat Phys* **9**, 626-630, (2013).
- 94 Michaeli, K., Potter, A. C. & Lee, P. A. Superconducting and Ferromagnetic Phases in
SrTiO₃/LaAlO₃ Oxide Interface Structures: Possibility of Finite Momentum Pairing. *Phys
Rev Lett* **108**, 117003, (2012).
- 95 Dietl, T., Ohno, H., Matsukura, F., Cibert, J. & Ferrand, D. Zener model description of
ferromagnetism in zinc-blende magnetic semiconductors. *Science* **287**, 1019-1022, (2000).
- 96 Pentcheva, R. & Pickett, W. E. Charge localization or itineracy at LaAlO₃/SrTiO₃
interfaces: Hole polarons, oxygen vacancies, and mobile electrons. *Phys Rev B* **74**, 035112,
(2006).
- 97 Pavlenko, N., Kopp, T., Tsymbal, E. Y., Mannhart, J. & Sawatzky, G. A. Oxygen vacancies
at titanate interfaces: Two-dimensional magnetism and orbital reconstruction. *Phys Rev B*
86, 064431, (2012).
- 98 Lee, J. S. *et al.* Titanium *d_{xy}* ferromagnetism at the LaAlO₃/SrTiO₃ interface. *Nat Mater*
12, 703-706, (2013).
- 99 Lee, M., Williams, J. R., Zhang, S., Frisbie, C. D. & Goldhaber-Gordon, D. Electrolyte
Gate-Controlled Kondo Effect in SrTiO₃. *Phys Rev Lett* **107**, 256601, (2011).
- 100 Moetakef, P. *et al.* Carrier-Controlled Ferromagnetism in SrTiO₃. *Physical Review X* **2**,
021014, (2012).
- 101 Kalisky, B. *et al.* Scanning Probe Manipulation of Magnetism at the LaAlO₃/SrTiO₃
Heterointerface. *Nano Lett* **12**, 4055-4059, (2012).
- 102 Bi, F. *et al.* Room-temperature electronically-controlled ferromagnetism at the LaAlO₃/
SrTiO₃ interface. *Nature Communications* **5**, 5019, (2014).
- 103 Kalisky, B. *et al.* Critical thickness for ferromagnetism in LaAlO₃/SrTiO₃ heterostructures.
Nature Communications **3**, 922, (2012).